Kyoto University

Search for $\nu_\mu \rightarrow \nu_e$ oscillation in a long-baseline accelerator experiment

A dissertation submitted to
the graduate school of science
in candidacy for the degree of
doctor of philosophy

Department of Physics

By
Shimpei Yamamoto

Kyoto, Japan
June 2006

Abstract

We report a search for $\nu_\mu \rightarrow \nu_e$ oscillation with the KEK to Kamioka (K2K) long-baseline neutrino oscillation experiment.

The evidence for neutrino oscillations has been provided by a series of experiments. In our current knowledge of the three-flavor framework, the neutrino flavor mixing is described by two parameters of mass-squared difference ($\Delta m^2_{\rm solar}, \Delta m^2_{\rm atm}$), three mixing angles ($\theta_{12}$, θ_{23}, θ_{13}) and a CP phase (δ). As yet, there is no measurement of the mixing angle θ_{13} but just a limit of $< 12^\circ$.

In the K2K experiment, we search for $\nu_\mu \rightarrow \nu_e$ oscillation in an accelerator-produced muon neutrino beam which results from non-zero value of θ_{13}. The neutrino beam is produced by KEK's proton synchrotron and directed toward the Super-Kamiokande detector (SK) 250 km away. We analyzed the entire data sample of 9.2×10^{19} protons on target. In the search for ν_e appearance, the background events from a neutral pion are the most significant in SK. We developed a new reconstruction algorithm to reject a neutral pion more efficiently. With the new π^0 rejection cut, we have achieved the background suppression by 70% and improved the sensitivity to $\nu_\mu \rightarrow \nu_e$ oscillation.

We have searched for a signal of $\nu_\mu \rightarrow \nu_e$ oscillation among one hundred and twelve beam neutrino events observed in SK. We observe one single candidate event, which is consistent with the background expectation of 1.7 events. Since we find no evidence of $\nu_\mu \rightarrow \nu_e$ oscillation, we set the limit on the $\nu_\mu \rightarrow \nu_e$ oscillation parameters. In a two-flavor approximation, we set a constraint on $\nu_\mu \rightarrow \nu_e$ neutrino oscillation as $\sin^2 2\theta_{\mu e} < 0.13$ [90% confidence level (C.L.)] at the Δm^2 region of 2.8×10^{-3} eV^2. For the higher Δm^2 region, the more stringent limit of $\sin^2 2\theta_{\mu e} < 0.10$ is obtained. Further, we set the upper limit of $\sin^2 2\theta_{13} < 0.26$ (90% C.L.) on the assumption of the relation $\sin^2 2\theta_{13} \simeq 2 \sin^2 2\theta_{\mu e}$. Our result is consistent with the results from the reactor $\bar{\nu}_e$ experiments over a few km baseline that show the lack of observed disappearance of $\bar{\nu}_e$.

Acknowledgment

I am most grateful for the support and encouragement of many people. I realize that my research have relied on their joint efforts, therefore, this thesis is humbly dedicated to them.

First of all, I would like to express my great appreciation to Prof. Koichiro Nishikawa for the opportunity to do research with the K2K experiment. His encouragement was always a boost to my research and carried me through. I give my special thanks to Prof. Tsuyoshi Nakaya for his guidance on various occasions. His wise advices during my Ph.D. experience led me to a new perspective on physics. I also give my special thanks to Prof. Kenji Kaneyuki. He gave me advisory opinions on my study with the Super-K data. I am deeply thankful to Dr. Masashi Yokoyama for his unstinting support. He guided me in my research and kindly worked as a proofreader for my articles every time. I thank a special colleague, Dr. Masaya Hasegawa, for useful discussions, keen humor and friendship. I look forward hopefully to the day when we collaborate again.

The years spent at KEK have been an incredible part of my life. I received an excellent education as well as a great pleasure. I address my thanks to Dr. Hirokazu Maesaka for his considerable efforts to the construction and operation of the SciBar detector. I was pleased at having a wonderful time with him. I owe Dr. Makoto Yoshida a debt of gratitude for his strong support. He generously served as assistant to me any number of times. I would like to thank Prof. M. Tanaka for giving me hard but stimulating works on the development of electronics at the SciBar detector. I also thank Mr. T. Murakami; without his support, I would never have completed them. I would be grateful to Dr. A. K. Ichikawa for her considerable efforts to the construction of SciBar. I also learned the basic skills in experimental physics from her. I give thanks to Dr. K. Nitta for his support, encouragement and all the good times. I am most

thankful to Dr. Y. Takubo. I received a lot of surprises and pleasures when we closely cooperated. I am also thankful to Mr. T. Morita and Mr. T. Sasaki for their cooperation and friendships. I often had a pleasant dinner with Prof. Y. Hayato, Dr. M. Yoshida, Dr. H. Yokoyama and Mrs. M. Sekiguchi; I would like to thank them a lot. I again thank Prof. Y. Hayato for his support and passing the interesting information about my favorite pastimes on to me.

In addition, my research is supported by many colleagues in the K2K collaboration. I express my thanks to the directors of Prof. Y. Totsuka, Prof. K. Nakamura, Prof. Y. Suzuki, Prof. C. K. Jung and Prof. R. J. Wilkes, and the devoted members of Prof. T. Kobayashi, Prof. M. Sakuda, Dr. T. Iwashita Dr. T. Ishida, Dr. T. Ishii, Dr. J. H. Choi, Dr. Y. Ooyama, Dr. T. Nakadaira, Prof. Y. Itow, Prof. M. Shiozawa, Dr. M. Miura, Dr. Y. Obayashi, Dr. J. Kameda, Dr. S. Nakayama, Dr. S. Yamada, Dr. S. Mine, Dr. T. Hasegawa and Dr. T. Maruyama. I address special thanks to Prof. K. Sholberg, Prof. D. Kielczewska and Ms. J. Zalipska for their useful suggestions in the paper publication committee. I offer additional thanks to Mr. R. Terri for his help in proofreading the thesis.

I must extend thanks to all of the past and present staffs and colleagues in the high energy physics group at Kyoto University for memorable days and their kindnesses: Prof. K. Nishikawa, Prof. N. Sasao, Prof. T. Nakaya, Prof. H. Sakamoto, Dr. R. Kikuchi, Dr. T. Nomura, Dr. H. Nanjo, Dr. M. Yokoyama, Dr. H. Tanaka, Dr. H. Sato, Mr. M. Suehiro, Mr. T. Fujiwara, Dr. T. Inagaki, Dr. H. Sakai, Dr. Y. Ushiroda, Dr. S. Nishida, Dr. I. Kato, Dr. Y. Honda, Dr. H. Maesaka, Dr. K. Mizouchi, Ms. K. Uchida, Mr. M. Hasegawa, Mr. T. Sumida, Mr. S. Tsuji, Mr. K. Maeda, Mr. K. Hayashi, Mr. H. Morii, Mr. T. Morita, Mr. S. Ueda, Mr. T. Sasaki, Mr. K. Hiraide, Mr. J. Kubota, Ms. T. Taniguchi, Mr. T. Shirai, Ms. K. Takezawa, Mr. H. Yokoyama, Mr. K. Ezawa, Mr. Y. Kurimoto, Mr. Y. Kurosawa, Mr. Y. Nakajima, Mr. T. Nobuhara, Mr. K. Matsuoka, Mr. M. Taguchi, Mr. S. Gomi, Mr. H. Kawamuko, Mr. H. Kubo, Mr. K. Shiomi, Mr. T. Usuki and the secretary Ms. A. Nakao. Dr. I. Kato kindly initiated me into experimental physics with his encouragement. I spent a happy academic career with Mr. T. Sumida, and hope to work together before long.

I am afraid that I cannot include every single person who significantly contributed to my research life, but I wish to thank everyone equally.

Finally, I gratefully acknowledge a lot of support from my immediate family for years.

Contents

Chapter 1

Introduction

1.1 Physics of neutrinos

The Standard Model of particle physics has been extremely successful in describing the interactions and properties of fundamental particles. However, up to now, we recognized that some experimental results cannot be explained within the framework of the current theory. Neutrino oscillation is one such subject.

The Standard Model defines a neutrino to be a spin 1/2 fermion; it is colorless and caries zero electromagnetic charge and weak isospin of +1/2. Therefore, the neutrino can only interact via the weak current. It is a lepton, and exists in three flavors: ν_e, ν_μ and ν_τ. Up to now, various experiments have been performed to measure the masses of neutrinos directly [1, 2, 3, 4]. Currently, there is no evidence for a finite neutrino mass, but the smallness of their masses is indicated. However, there were disagreements between the measured neutrino fluxes and the theoretical predictions in the observations of neutrinos produced in the sun and the earth's atmosphere. One possible solution to these anomalies is drawn up with the phenomenon of flavor mixing in neutrinos, which is caused by finite neutrino masses. In 1967, Pontecorvo first considered the consequences of this phenomena which describes quark mixing. He advocated that neutrinos have a finite mass, where the weak and mass eigenstates are not identical and then formulated a mixing between neutrinos as well as quarks.

In this section, we introduce massive neutrinos as an extension to the Standard Model and explain neutrino oscillations.

1.1.1 Massive neutrinos

Massive neutrinos can be introduced with only a minor extension to the Standard Model. Neutrino masses can appear in two ways: as the Dirac mass term in the Lagrangian or introducing the Majorana mass term.

The Dirac term assumes that a particle and its antiparticle are different, which involves transitions between right- and left-handed states. That is, the right-handed neutrino ν_R is different from its charge conjugation ν_R^C which is the CPT partner of ν_L. The Dirac mass term (L_D) is formulated as

$$\begin{aligned} \mathrm{L}_D &= m_D \overline{\nu} \nu & (1.1) \\ &= m_D (\overline{\nu}_L \nu_R + \overline{\nu}_R \nu_L), & (1.2) \end{aligned}$$

where the Dirac field ν is defined as $\nu \equiv \nu_L + \nu_R$. Thus, Dirac neutrinos have four components, ν_L, ν_R^C, ν_R and ν_L^C, and conserve the lepton number.

Alternatively, a neutrino can be its own antiparticle as $(\nu_L)^C = \nu_R^C$ because neutrinos are neutral particles. Such a particle is called a "Majorana" particle. A Majorana neutrino causes a transition between a neutrino and an anti-neutrino, which violates lepton number conservation. The form of a Majorana mass term (L_M) is

$$\begin{aligned} \mathrm{L}_M &= m_M \overline{\chi} \chi & (1.3) \\ &= m_M (\overline{\nu}_L \nu_R^C + \overline{\nu}_R^C \nu_L) & (1.4) \end{aligned}$$

where χ is the self conjugate field $\chi = \nu_L + \nu_R^C$ satisfying $\chi = \chi^C$.

In order to incorporate the neutrino mass into the Standard Model, we introduce a $SU(2)$ singlet ν_R. Since the right-handed neutrino does not interact (sterile neutrino), it is possible to describe a scenario in which both Dirac and Majorana mass terms are present. Expressing ν_L and ν_R in terms of the self-conjugate fields χ and ω as $\chi = \nu_L + (\nu_L)^C$ and $\omega = \nu_R + (\nu_R)^C$, we can write the Lagrangian for neutrino masses as follows:

$$\mathrm{L} = \overline{n}_L \mathrm{M} n_L + h.c., \quad (1.5)$$

where

$$\begin{aligned} n_L &= \begin{pmatrix} \chi \\ \omega \end{pmatrix}, & (1.6) \\ \mathrm{M} &= \begin{pmatrix} m_L & m_D/2 \\ m_D/2 & m_R \end{pmatrix}, & (1.7) \end{aligned}$$

m_L and m_R are the Majorana masses associated with the left and right handed neutrinos, respectively, and *h.c.* means the Hermite conjugate of the first term. Diagonalizing M to $diag(m_1, m_2)$ yields:

$$m_{1,2} = \frac{1}{2}\left\{(m_R + m_L) \pm \sqrt{(m_R - m_L)^2 + m_D^2}\right\}, \tag{1.8}$$

$$\begin{pmatrix} \chi \\ \omega \end{pmatrix} = \begin{pmatrix} \cos\theta & \sin\theta \\ -\sin\theta & \cos\theta \end{pmatrix}\begin{pmatrix} \eta_1 \\ \eta_2 \end{pmatrix}, \tag{1.9}$$

where $\eta_{1,2}$ is the mass eigenstate and the mixing angle θ is given by $\tan 2\theta = \frac{m_D}{m_R - m_L}$.

Seesaw mechanism

Considering the case where $m_L = 0$ and $m_R \gg m_D$, we obtain mass eigenstates as

$$m_1 \sim \frac{m_D^2}{m_R}, \quad m_2 \sim m_R. \tag{1.10}$$

This indicates that a Dirac mass due to ν_L and a heavier mass due to ν_R can cause a very light mass state m_1 and a very heavy m_2. This special case is known as the seesaw mechanism [5,6], and it provides an explanation to the small neutrino masses.

1.1.2 Neutrino oscillations in a vacuum

Introducing massive neutrinos to the Standard Model, we can consider the mixing of flavors between them. Assuming that neutrinos have the Dirac mass with three mass eigenstates $\nu_i, i = 1, 2, 3$, each with a mass m_i, the neutrino flavor eigenstates can be written as linear combinations of them:

$$\nu_\alpha = \sum_{i=1,2,3} U_{\alpha i}\nu_i, \tag{1.11}$$

where α and i are the indexes of the flavor eigenstates (ν_e, ν_μ, ν_τ) and the mass eigenstates (ν_1, ν_2, ν_3), respectively. $U_{\alpha i}$ is an unitary matrix known as the Maki-Nakagawa-Sakata (MNS) matrix, which can be parametrized in the same way as

the Cabibbo-Kobayashi-Maskawa matrix for quark mixing:

$$
\begin{aligned}
U &= \begin{pmatrix} 1 & & \\ & c_{23} & s_{23} \\ & -s_{23} & c_{23} \end{pmatrix}\begin{pmatrix} c_{13} & & s_{13}e^{-i\delta} \\ & 1 & \\ -s_{13}e^{i\delta} & & c_{13} \end{pmatrix}\begin{pmatrix} c_{12} & s_{12} & \\ -s_{12} & c_{12} & \\ & & 1 \end{pmatrix} \\
&= \begin{pmatrix} c_{13}c_{12} & c_{13}s_{12} & s_{13}e^{-i\delta} \\ -c_{23}s_{12} - s_{13}s_{23}c_{12}e^{i\delta} & c_{23}c_{12} - s_{13}s_{23}s_{12}e^{i\delta} & c_{13}s_{23} \\ s_{23}s_{12} - s_{13}c_{23}c_{12}e^{i\delta} & -s_{23}c_{12} - s_{13}c_{23}s_{12}e^{i\delta} & c_{13}c_{23} \end{pmatrix},
\end{aligned} \tag{1.12}
$$

where $c_{ij} \equiv \cos\theta_{ij}$, $s_{ij} \equiv \sin\theta_{ij}$, θ_{ij} is the mixing angle for each flavor, and δ is a complex phase which causes the CP violation.

Now we consider the time evolution of a state that is in a flavor eigenstate ν_α at $t = 0$. The initial state is represented as

$$
|\nu_\alpha(t=0)\rangle = \sum_i U_{\alpha i}\,|\nu_i\rangle\,. \tag{1.13}
$$

The time evolution of the state depends on its energy eigenvalues, and is represented as

$$
|\nu_\alpha(t)\rangle = \sum_i U_{\alpha_i} e^{-iE_i t}\,|\nu_i\rangle\,, \tag{1.14}
$$

$$
E_i^2 = p^2 + m_i^2, \tag{1.15}
$$

where p and $m_{1,2,3}$ are the neutrino momentum and masses, respectively. Here, the probability that a neutrino in a flavor eigenstate ν_α at $t = 0$ is observed as ν_β at time t, $(P_{\alpha\to\beta})$, is formulated as

$$
\begin{aligned}
P_{\alpha\to\beta} &= \left|\left\langle \nu_\beta(t)|\nu_\alpha(0)\right\rangle\right|^2 \\
&= \sum_i \left|\left\langle \nu_\beta(0)|U_{\beta i}e^{-iE_i t}U^\dagger_{\alpha i}|\nu_\alpha(0)\right\rangle\right|^2 \\
&= \sum_i \left|U_{\alpha i}U_{\beta i}\right|^2 + \sum_{i\neq j} U_{\alpha i}U^*_{\beta i}U^*_{\alpha j}U_{\beta j}e^{-i(E_i-E_j)t}.
\end{aligned} \tag{1.16}
$$

As a consequence of flavor mixing for massive neutrinos, the flavor transition phenomenon, called "neutrino oscillations," could take place.

It is instructive to describe the probabilities in the framework of two-flavor mixing. Considering two flavors of ν_α and ν_β, the matrix U is given as follows:

$$
U = \begin{pmatrix} \cos\theta & \sin\theta \\ -\sin\theta & \cos\theta \end{pmatrix}. \tag{1.17}
$$

The probability for $\nu_\alpha \to \nu_\beta$ oscillation is given as

$$P(\nu_\alpha \to \nu_\beta) = \sin^2 2\theta \sin^2\left(\frac{(E_i - E_j)t}{2}\right). \tag{1.18}$$

Making an approximation of $E_i \sim p + m_i^2/2p$ and including the factors of $\hbar$ and c, the probability is formulated as

$$P(\nu_\alpha \to \nu_\beta) = \sin^2 2\theta \sin^2\left(\frac{1.27\Delta m^2[\mathrm{eV}^2]L[\mathrm{km}]}{E[\mathrm{GeV}]}\right), \tag{1.19}$$

where $\Delta m^2 \equiv m_j^2 - m_i^2$ is the mass-squared difference and L is the flight length of neutrino.

If the neutrino mass states mix together and their eigenvalues are different, that is $\theta \neq 0$ and $\Delta m^2 \neq 0$, neutrinos can change their flavor during travel. Thus, the observation of neutrino oscillation gives an evidence for the finite neutrino mass. The oscillation amplitude is characterized by the mixing angle θ and the mass-squared difference Δm^2, and expressed as a function of L/E. The oscillation effect is enhanced to the maximum when the following condition is satisfied:

$$\frac{L\ [\mathrm{km}]}{E\ [\mathrm{GeV}]} = \frac{\pi}{2.53 \cdot \Delta m^2\ [\mathrm{eV}^2]}. \tag{1.20}$$

1.2 Search for neutrino oscillation

Currently, there is no theoretical prediction on neutrino masses, and many experiments have been performed to probe the masses of neutrinos. Up to now, the evidence for neutrino oscillations has been discovered by various experiments. The neutrino oscillation experiments measure the sizes of the squared-mass differences and the mixing angles; these are called "oscillation parameters". Figure 1.2 shows the regions of neutrino oscillation parameter space allowed or excluded by various experiments. In this chapter, we introduce neutrino oscillation experiments and summarize our current knowledge of the oscillation phenomena.

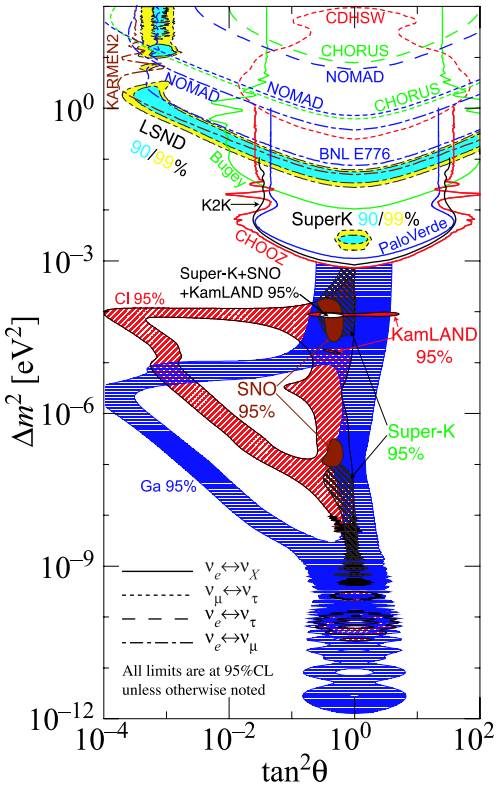

Figure 1.1: The regions of Δm^2 and mixing angle allowed or excluded by various experiments.

1.2.1 Mixing parameters measured by various neutrino oscillation experiments.

$\Delta m^2_{\text{solar}}$ region ($10^{-5} \sim 10^{-4}$ eV^2) :

The electron neutrinos created in the sun have been measured by several experiments: Homestake [7], Kamiokande [8], SAGE [9], GALLEX [10], GNO [11], SK [12] and SNO [13]. All of these experiments observed a deficit of solar neutrino fluxes compared with the prediction of the standard solar model. Because the energy of solar neutrinos is in the range from 0 to 15 MeV and the flight length is $\sim 10^{18}$ km, a small Δm^2 region (down to 10^{-11} eV^2) can be probed according to Equation 1.20.

Thanks especially to the flux measurements by SNO and SK, we understood that the solar neutrino oscillation is described by the LMA-MSW solution [14]. The solar neutrino results have been also confirmed with the spectral distortion and the flux reduction of reactor $\bar{\nu}_e$ measured by the KamLAND experiment [15]. Combining the KamLAND result with solar neutrino measurements, the param-

eters of neutrino oscillation $\nu_e \rightarrow \nu_x$ are constrained to be

$$7.4 \times 10^{-5} < \Delta m^2_{solar} < 8.6 \times 10^{-5} [\mathrm{eV}^2], \tag{1.21}$$

$$0.37 < \tan^2 \theta_{\mathrm{solar}} < 0.54, \tag{1.22}$$

at 95% confidence level (C.L.).

$\Delta m^2_{\mathrm{atm}}$ region ($\sim 10^{-3}$ eV^2) :

High energy primary cosmic-rays interacting with the atmosphere produce a cascade of secondary particles, mostly pions and kaons, whose decay chains result in a high flux of neutrinos called "atmospheric neutrinos". In the Δm^2 region of $10^{-3} \sim 10^{-2}$ eV^2, evidence for neutrino oscillations has been given in the atmospheric neutrino experiments [16, 17]. The energy spectrum of atmospheric neutrinos is in the range 0.1 − 100 GeV, and the flight length of neutrinos detected on the surface of the earth ranges from 10^1 km to 10^4 km. Due to these characteristics, we can probe neutrino oscillations with the sensitivity down to $\Delta m^2 \sim 10^{-5}$ eV^2. The SK collaboration found that the zenith angle distributions of muon neutrinos are asymmetric [16]. The SK collaboration also reported the observation of an oscillatory signature with L/E dependence [17]. It is well described by the hypothesis that ν_μ oscillates to ν_τ with a probability of nearly 100%. Long-baseline experiments with a muon neutrino beam, such as K2K [18] and MINOS [19], also confirmed the SK results by measuring the spectral distortion and the reduction of ν_μ flux during travel. In the two-flavor mixing framework, the neutrino oscillation parameters of $\nu_\mu \rightarrow \nu_\tau$ are constrained to be

$$1.9 \times 10^{-3} < \Delta m^2_{atm} < 3.1 \times 10^{-3} [\mathrm{eV}^2], \tag{1.23}$$

$$\sin^2 2\theta_{\mathrm{atm}} > 0.90, \tag{1.24}$$

at 90% C.L.

The results from atmospheric neutrino experiments imply the probability of $\nu_\mu \rightarrow \nu_e$ oscillation is small. The null results of disappearance of reactor $\bar{\nu}_e$ by CHOOZ [20] and Palo-Verde [21] also limit the probability of $\nu_\mu \rightarrow \nu_e$ oscillation, assuming CPT invariance $P(\bar{\nu}_e \rightarrow \bar{\nu}_\mu) = P(\nu_\mu \rightarrow \nu_e)$.

$\Delta m^2_{\mathrm{LSND}}$ region ($\sim 1\ \mathrm{eV}^2$) :

There is another report on neutrino oscillation from LSND. LSND is an accelerator experiment with $\bar{\nu}_\mu$ and observed an excess of $\bar{\nu}_\mu \to \bar{\nu}_e$ signal events. In the three-flavor framework, there are only three mass-squared differences and the sum of them is zero. Up to now, two of three are measured by solar neutrino, atmospheric neutrino and long-baseline experiments experiments as described above; these results indicate that the maximum one ($= \Delta m^2_{\mathrm{solar}} + \Delta m^2_{\mathrm{atm}}$) is near to $\Delta m^2_{\mathrm{atm}}$ considering $\Delta m^2_{\mathrm{atm}} \gg \Delta m^2_{\mathrm{solar}}$. The LSND result indicates that Δm^2 of $\sim 1\ \mathrm{eV}^2$ ($\neq \Delta m^2_{\mathrm{atm}}$), which is inconsistent with our expectation. This result requires the extension of the neutrino mixing framework with more than three neutrinos where a sterile neutrino is added to three active ones. However, the KARMEN experiments [22], which has a similar experimental sensitivity as LSND, showed null results on $\bar{\nu}_\mu \to \bar{\nu}_e$ oscillation. This issue is being addressed by the MiniBooNE experiment [23], whose purpose is to confirm or reject the LSND result.

1.2.2 Unsettled subjects on neutrino flavor mixing

If we assume the framework of three active neutrinos, solar neutrino oscillation occurs mainly with a small mass-squared difference:

$$\Delta m^2_{\mathrm{solar}} \equiv m_2^2 - m_1^2 = \Delta m^2_{21} (> 0). \tag{1.25}$$

Results from atmospheric neutrino experiments imply that there is a small component of ν_e in the ν_3 mass eigenstate, and the observed mass-squared difference is larger than that of solar neutrinos ($\Delta m^2_{atm} \gg \Delta m^2_{solar}$). Because the states of m_1 and m_2 are closely spaced, $\Delta m^2_{\mathrm{atm}}$ is represented as

$$\Delta m^2_{\mathrm{atm}} \equiv \left| m_3^2 - m_2^2 \right| = \left| \Delta m^2_{32} \right| \sim \left| \Delta m^2_{31} \right|. \tag{1.26}$$

The sign of Δm^2_{32} (or Δm^2_{31}) is still unknown, and there is two possibilities of mass hierarchy: $m_1 < m_2 < m_3$ (called normal hierarchy) or $m_3 < m_1 < m_2$. Figure 1.2 show the current understanding of the squared-mass spectrum in the framework of three active neutrinos and the normal mass hierarchy. We use the parameterized form of MNS matrix to identify the measured mixing angles as $\theta_{12} \cong \theta_{\mathrm{solar}}, \theta_{23} \cong \theta_{\mathrm{atm}}$.

Up to the present, the unsettled subjects on the neutrino flavor mixing are:

- Size of the mixing angle θ_{13},

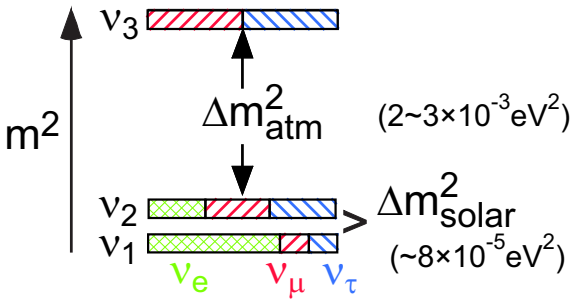

Figure 1.2: Squared-mass spectrum in three-neutrino framework. For each mass eigenstate, the fractions of neutrino flavors are shown. The fraction of ν_e is shown with cross-hatching, the ν_μ fraction with right-leaning hatching, and the ν_τ fraction with left-leaning hatching.

- Determination of the mass hierarchy,
- Size of CP phase δ.

A goal in neutrino physics is to measure the mixing angle θ_{13}; this mixing angle is yet to be measured. As mentioned before, the reactor neutrino experiments reported null results on $\bar{\nu}_e \to \bar{\nu}_x$ oscillation. The survival probability of $\bar{\nu}_e$ ($P_{\bar{\nu}_e \to \bar{\nu}_e}$) in the reactor experiments can be written

$$\begin{aligned} P_{\bar{\nu}_e \to \bar{\nu}_e} &\simeq 1 - \sin^2 2\theta_{13} \sin^2(\Delta m^2_{31} L/4E) \\ &\quad + \alpha^2 (\Delta m^2_{31} L/4E)^2 \cos^4 \theta_{13} \sin^2 2\theta_{12}, \end{aligned} \tag{1.27}$$

where $\alpha = \Delta m^2_{21}/\Delta m^2_{32}$. Thanks to the smallness of α, the third term is negligible and the probability is formed by two parameters, $\sin^2 2\theta_{13}$ and Δm^2_{31}. Currently, a limit of $\sin^2 2\theta_{13} < 0.13$ ($\theta_{13} <\sim 12°$) [20] at the $\Delta m^2_{\rm atm}$ region of 2.8×10^{-3} eV^2 is set on this mixing angle at 90% C.L. The search for neutrino oscillations with a baseline of several hundred km, such as K2K and MINOS, also have a potential to measure θ_{13}. The probability that ν_μ oscillates to ν_e ($P_{\nu_\mu \to \nu_e}$) can be given as

$$\begin{aligned} P_{\nu_\mu \to \nu_e} &= \sin^2 2\theta_{\mu e} \sin^2(\Delta m^2_{\mu e} L/4E) \\ &\simeq \sin^2 2\theta_{13} \sin^2 \theta_{23} \sin^2(\Delta m^2_{31} L/4E) \\ &\simeq \frac{1}{2} \sin^2 2\theta_{13} \sin^2(\Delta m^2_{31} L/4E). \end{aligned} \tag{1.28}$$

In the above expression, we suppose $\sin^2 2\theta_{23} \simeq \sin^2 2\theta_{atm} \sim 1.0$. Considering $\Delta m^2_{31} \sim \Delta m^2_{\rm atm}$, these accelerator experiments can probe the mixing angle θ_{13} in the mode $\nu_\mu \to \nu_e$.

1.3 Motivation for $\nu_\mu \rightarrow \nu_e$ search

The recent discovery of neutrino oscillations by several experiments are full of surprise and have provided a new window into physics beyond the Standard Model. In the three-flavor framework, neutrino mixing is described by two parameters of mass-squared difference (Δm^2_{solar}, Δm^2_{atm}), three mixing angles (θ_{12}, θ_{23}, θ_{13}) and a CP phase (δ). As yet, we know very little about the mixing angle θ_{13}, although the null results of disappearance of reactor $\bar{\nu}_e$ by CHOOZ and Palo Verde indicate that θ_{13} should be smaller than 12°.

Motivated by such situations, we have performed a search for θ_{13} in an experiment with a muon neutrino beam and a baseline of 250 km. We probe θ_{13} in the $\nu_\mu \rightarrow \nu_e$ appearance mode, which provides a complementary result to what the reactor neutrino measurements concluded. If θ_{13} has a non-zero value, we will investigate the CP violation in lepton sector by comparing $\nu_\mu \rightarrow \nu_e$ to its CP-mirror image $\bar{\nu}_\mu \rightarrow \bar{\nu}_e$ in the future. In the see-saw model, the neutrino mass eigenstates are identical to their anti-particles and $\nu_\mu \rightarrow \nu_e$ and $\bar{\nu}_\mu \rightarrow \bar{\nu}_e$ are different processes. Demonstrations of CP violation in the interactions of light neutrinos could enhance the feasibility of the production of the matter anti-matter asymmetry, known as leptogenesis.

In this thesis, we report the results of the search for $\nu_\mu \rightarrow \nu_e$ oscillation in the K2K experiment using the entire data sample. For the ν_e appearance signal search, the neutral pion production is the most significant background at the SK detector. We have studied this π^0 background and applied a new π^0 rejection algorithm. In this chapter, we summarized neutrino physics and the experimental searches for neutrino oscillations as the introduction. We will begin with an overview of the K2K experiment in Chapter 2. The following chapters (Chapter 3-9) give descriptions of the analysis: Monte Carlo (MC) simulations, predictions of the neutrino event rate and energy spectrum at SK, the signal selection, and the constraint on $\nu_\mu \rightarrow \nu_e$ oscillation parameters.

Chapter 2

The K2K experiment

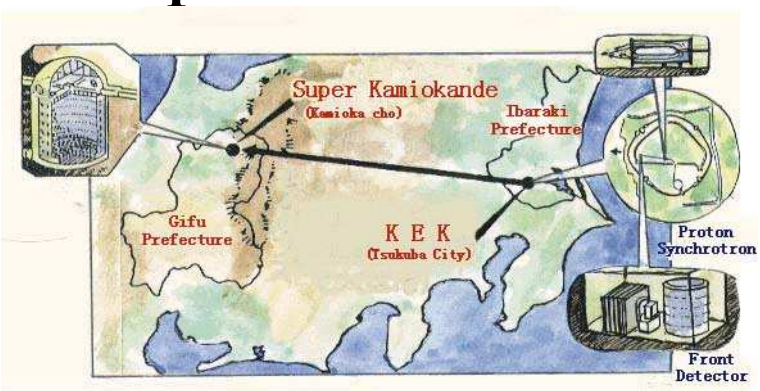

2.1 Experimental goal and design

The KEK to Kamioka long-baseline neutrino oscillation experiment (K2K) uses an accelerator-produced neutrino beam of nearly pure ν_μ. The neutrino beam is produced by a 12 GeV proton synchrotron accelerator in KEK [24] and directed toward the Super-Kamiokande detector 250 km away. In the proton collisions on an aluminum target, positive pions are produced and their decays consist of ν_μ's. With a mean neutrino energy of 1.3 GeV and a baseline of 250 km, the experiment has the maximum sensitivity to neutrino oscillations with

$$\Delta m^2 = \frac{\pi E[\mathrm{GeV}]}{2.53 \cdot L[\mathrm{km}]} \sim 6 \times 10^{-3} \mathrm{eV}^2. \tag{2.1}$$

The sensitivity of K2K covers the parameter region $\Delta m^2 = 2 \sim 3 \times 10^{-3}$ eV^2 indicated by the atmospheric neutrino anomaly.

The goals of the K2K experiment are:

— Confirmation of the muon neutrino deficit in atmospheric neutrinos ($\nu_\mu \rightarrow \nu_x$),

— Search for electron neutrino appearance ($\nu_\mu \rightarrow \nu_e$).

Neutrino oscillations cause the reduction of the total number of ν_μ events at SK. In addition, the wide-band ν_μ spectrum is distorted at SK due to the energy-dependent oscillation probability, as shown in Figure 2.1. To confirm the results of atmospheric neutrinos, we evaluate these characteristics by comparing the observation with the predictions without oscillation. Moreover, we probe the $\nu_\mu \rightarrow \nu_e$ oscillation in K2K. The sub-dominant contribution of $\nu_\mu \rightarrow \nu_e$ oscillation is not completely excluded yet, although the ν_μ oscillation is the dominant contribution. We look for the excess of ν_e events at SK and set a constraint on $\nu_\mu \rightarrow \nu_e$ oscillation parameters. Both measurements of $\nu_\mu \rightarrow \nu_\tau$ and $\nu_\mu \rightarrow \nu_e$ oscillation are the first experimental approach using an accelerator-produced ν_μ beam with a long baseline over a few hundred km.

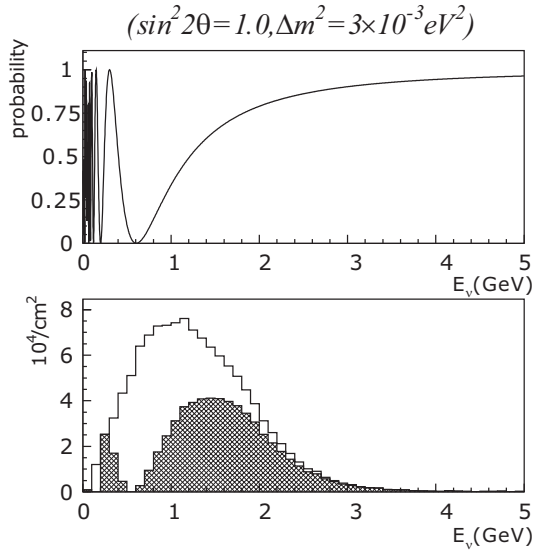

Figure 2.1: Oscillation probability (upper) and ν_μ energy spectrum (lower) at SK. In the lower figure, the solid histogram shows the energy spectrum without neutrino oscillation while the hatched one shows the energy spectrum on the assumption of oscillation parameters $\Delta m^2 = 3 \times 10^{-3}\mathrm{eV}^2$ and $\sin^2 2\theta = 1.0$.

In order to study neutrino oscillations, the K2K experiment has some key components in its design as described below.

Beam direction monitoring:

In K2K, the variation of the beam direction affects the neutrino flux and the energy spectrum at SK. In the Monte Carlo (MC) simulation, a change in the beam direction by 3 mrad reduces the neutrino flux by 1%. Thus, we require the beam to be controlled with an accuracy of 1 mrad as a guarantee of beam stability at SK. For this purpose, several beam monitors and near detectors are employed in KEK.

Measurements at the near detectors:

The absolute neutrino flux has a large uncertainty due to difficulties in the estimation of the primary proton beam intensity, the proton targeting efficiency, and hadron production cross-sections. There are also a large uncertainty in the neutrino-nucleus interactions in water. To avoid these uncertainties, we predict the neutrino event rate at SK by using the measured event rate and the energy spectrum at the near detectors.

Neutrino flux extrapolation from the near site to SK:

Due to the difference of beam acceptances between the near detectors and SK, the neutrino energy spectra at the near site and SK are different. In order to account for this difference, we evaluate the energy-dependent ratio of the ν_μ flux at SK to the near site (far/near flux ratio) with the *in situ* measurement of pion production in $p - Al$ collisions. Then, we derive the the expected neutrino event rate and energy spectrum at SK without oscillation from the near detector measurements transformed using the far/near ratio.

Timing synchronization between near site and SK:

With the K2K neutrino beam, we expect the event rate at SK to be 0.4 per day in the case of no oscillation. On the other hand, atmospheric neutrinos are detected with a rate of about 8 events per day; that could be a crucial background. Therefore, we adopt the time synchronization between the accelerator and SK by using the Global Positioning System (GPS).

2.2 Experimental components

A schematic view of the K2K experiment is shown in Figure 2.2. An overview of the experiment is as follows:

(i) Protons are accelerated by KEK's proton synchrotron and hit the aluminum target. In proton collisions, positive pions are produced and focused toward SK by the magnetic horns (Figure 2.2(a)).

(ii) The ν_μ beam is produced in positive pion decays, and its direction is monitored (Figure 2.2(b)).

(iii) The near detectors measure the neutrino interaction rate and the energy spectrum (Figure 2.2(c)).

(iv) After traveling 250 km, beam neutrinos are detected in SK (Figure 2.2(d)).

(v) The SK event times are synchronized with the accelerator (Figure 2.2(e)).

We will describe each experimental component in this section.

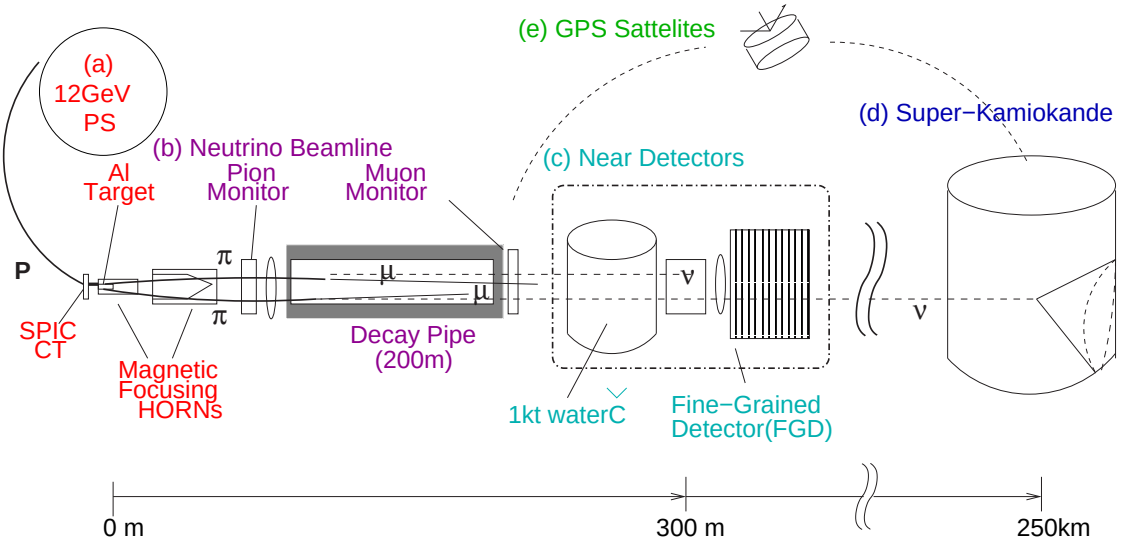

Figure 2.2: Schematic overview of the K2K experiment.

2.2.1 Primary proton beam

KEK 12 GeV proton synchrotron

The primary proton beam is provided by the 12 GeV proton synchrotron at KEK [25]. The accelerator is composed of a 750 keV Cockcroft-Walton pre-accelerator,

40 MeV drift-tube LINAC injector, 500 MeV booster synchrotron and the main ring of the synchrotron accelerating protons up to a kinetic energy of 12 GeV. In operation, approximately $6 \sim 7 \times 10^{12}$ protons are accelerated in every repetition cycle of 2.2 seconds. Accelerated protons are extracted in one turn; this is called "fast extraction". Then, protons are transported to the primary proton beam-line. The proton beam has the micro structure of nine bunches inside a spill, corresponding to the harmonic number of the main ring. The duration of the spill is 1.1 μsec.

Proton beam monitors

The extracted proton beam is transported in the primary beam-line, bent by 90 degrees toward SK (downward by 1.075 degrees), and hits the aluminum target. Figure 2.3 shows a schematic view of the beam-line.

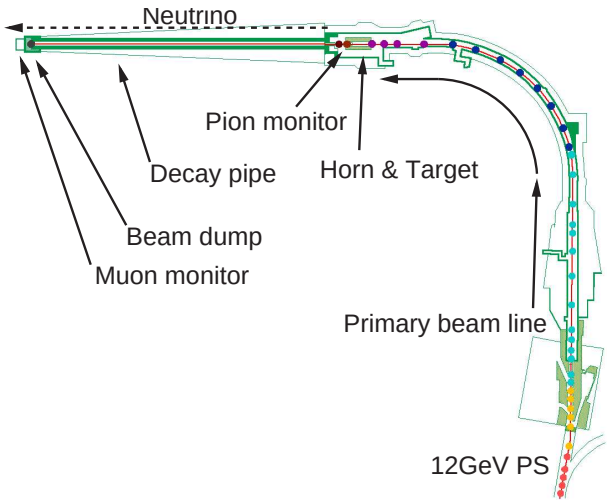

Figure 2.3: Schematic view of the beam-line. The points along the beam-line indicate the locations of the CTs and the SPICs.

In order to monitor the beam intensity and profile, current transformers (CTs) and segmented plate ionization chambers (SPICs) [26] are installed in multiple places along the beam-line. The CT is a beam intensity monitor consisting of a toroidal coil. The CT picks up the induced current from the beam spill by spill. The efficiency of the beam transportation is measured by the CTs and estimated to be approximately 85%. A CT placed just upstream of the target (called "TGT-CT") is used to estimated the number of delivered protons on the target (POT).

SPICs are used for the monitoring of the beam profile. The information measured by two SPICs (V39-SPIC and TGT-SPIC) located upstream of the target is used as the input into our simulation for the neutrino beam.

Hadron production target and magnetic horns

In proton collisions on the aluminum target, mainly pions are produced. To focus positive pions toward the direction of SK, two toroidal magnetic horns are employed [27]. A schematic view of the magnetic horns is shown in Figure 2.4. To enhance the focusing effect of positive pions, the aluminum target rod with dimensions of 3 cm in diameter and 66 cm in length is inserted into the first horn. This plays the role of inner conductor of the horn current. Supplying pulsed electric current of 250 kA to the horns, the maximum magnetic field of 3.3 T is achieved at the surface of the target rod. Thanks to the magnetic horns, the neutrino flux is 22 times higher than that without the horn current, as shown in Figure 2.5.

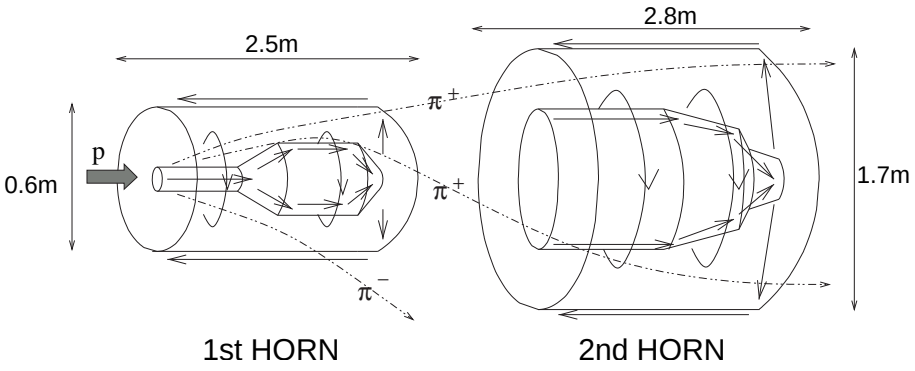

Figure 2.4: Schematic view of aluminum target and magnetic horns. The electrical current of 250 kA is supplied to the horns, making a toroidal magnetic field inside the horns. The aluminum target is inserted into the first horn.

2.2.2 Neutrino beam and monitors

Pion monitor

A gas Cherenkov imaging detector, called a pion monitor, is employed downstream the magnetic horn system to measure the secondary pions. The schematic

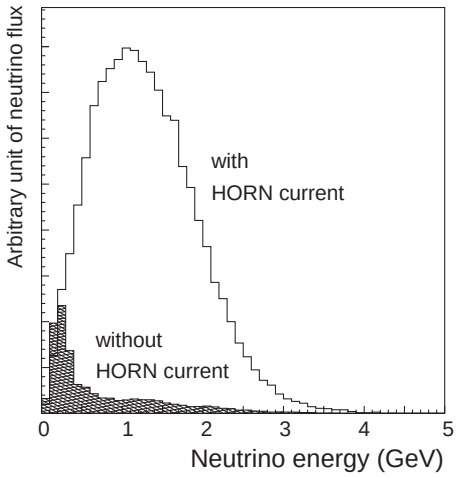

Figure 2.5: Neutrino flux at SK with and without horn current.

view of the pion monitor is shown in Figure 2.6.

The two-body decay kinematics of a pion is well-understood, and the neutrino energy spectrum at any location can be predicted from the measurements of pion momentum and direction. Thus, we can predict the neutrino spectra and the fluxes at the near and far sites; we derive the far/near flux ratio from these predictions. The results of this measurement validate the calculation of far/near flux ratio computed by the beam MC simulation (Section 5.3).

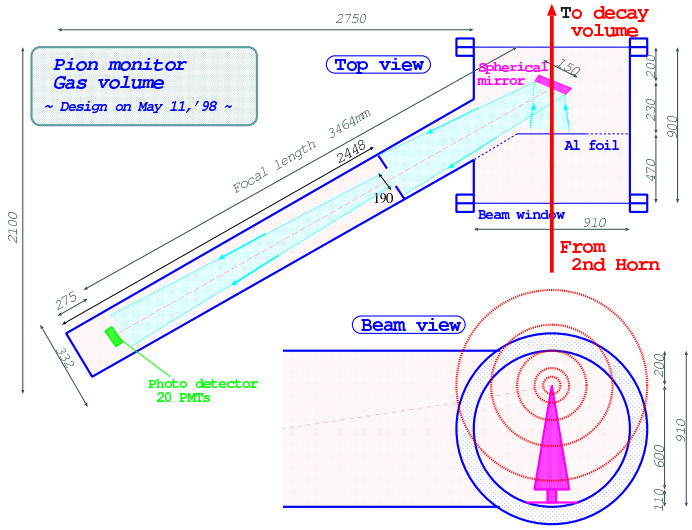

Figure 2.6: Schematic view of the pion monitor.

Decay volume

Positive pions focused by the magnetic horns enter a decay volume. The decay volume is a cylindrical pipe and its length is 200 m. Inside this volume, the positive pions decay to μ^+'s and ν_μ's, $\pi^+ \rightarrow \mu^+ + \nu_\mu$, with a fraction of almost 100%. To avoid the hadronic interactions of pions, the decay volume is filled with a helium gas of 1 atm.

At the end of the decay volume, there is a beam dump composed of 3.5m-thick iron and 2.0m-thick concrete. All the particles except for neutrinos and high-energy muons above 5.5 GeV/c are stopped there.

Muon monitor

There is a pit just downstream of the beam dump. The muon flux at the pit is estimated to be $\sim 10^4$ muons/cm^2. Since the parent particles of both muons and neutrinos are pions, we can measure the neutrino beam direction by measuring the direction of muons. The direction of muons is defined as the center of the spacial profile measured by two detectors called the "muon monitor [28]": one is a segmented ionization chamber (ICH) and the other is an array of silicon pad detectors (SPDs). Figure 2.7 shows the center of muon profile as a function of running time measured by the ICH. The beam direction has been controlled within 1 mrad as required.

2.2.3 Near detector complex

The near detector (ND) complex is located 300m downstream of the target. It is formed by two neutrino detector systems: a 1kt water Cherenkov detector and a fine-grain detector (FGD) system. Figure 2.8 shows a schematic overview of the ND complex. They are located in a cylindrical hole with dimensions of 24 m in diameter and 16 m in depth, set on the axis of the neutrino beam. Each detector has a different capability to measure the neutrino beam. Detailed descriptions of each detector are given below.

1kt water Cherenkov detector

A 1kt ring-imaging water Cherenkov detector (1KT), a miniature of the Super-Kamiokande detector, is installed as the most upstream detector at the near de-

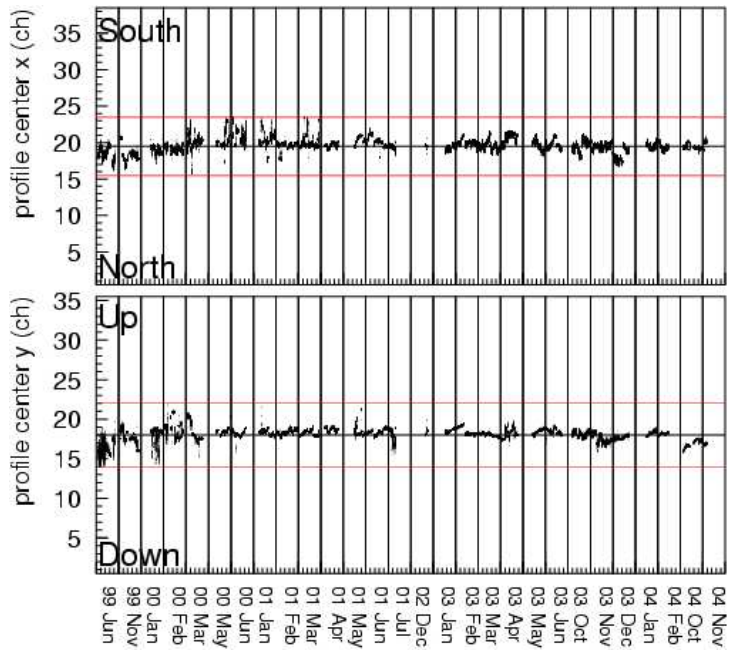

Figure 2.7: Stability of the center of muon profile measured by the ICH of the muon monitor. The upper figure shows the stability in the horizontal direction and the lower shows that in the vertical direction. The horizon black lines show the beam direction to SK measured by GPS, and red ones are off to the center by ±1 mrad.

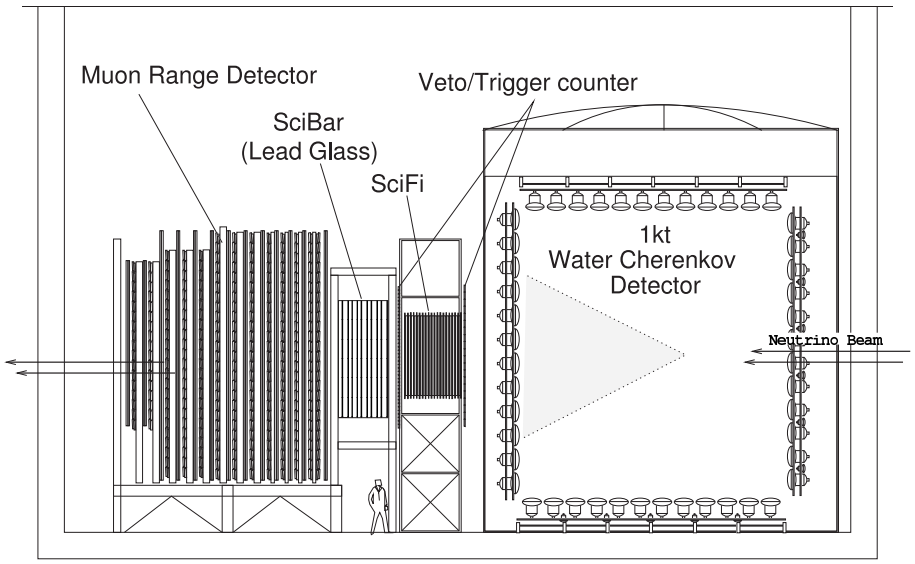

Figure 2.8: Schematic view of the near detector complex.

tector complex. Figure 2.9 shows a schematic view of the 1KT detector. The water tank is a cylinder with the dimensions of 10.8 m in diameter and 10.8 m in height, and filled with 1 kton of pure water. The inside of the tank is optically separated into two parts: the inner detector (ID) with a cylindrical volume of 8.6 m in diameter and 8.6 m in height, and the outer detector surrounding the ID. There are 680 20-inch photomultipliers (PMTs) facing inward, providing the photo-cathode coverage of 40%. The thickness of the OD part is 1 m for the barrel and 0.6 m for the bottom. There are 68 8-inch PMTs facing outward on the support frame: 42 PMTs are attached to the upstream 1/3 of the barrel and the rest are attached to the bottom. They work as the veto of incoming particles induced by neutrinos interacting outside. It also provides triggers to record cosmic-ray events for calibration.

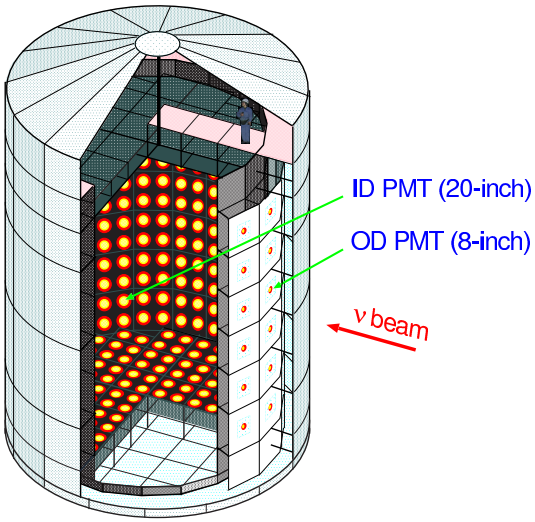

Figure 2.9: Schematic view of the 1kt detector.

The PMTs in the 1KT detect Cherenkov photons emitted from a charged particle traveling in the water. The refractive index of water is 1.33–1.36 depending on the wavelength. The momentum thresholds of Cherenkov radiation for an electron, a muon, a pion, and a proton are 0.58, 120, 159, and 1070 MeV/c, respectively. A particle with $\beta = 1$ emits approximately 340 photons per 1 cm in the wavelength 300–600 nm, where a 20 inch PMT is sensitive. The opening angle of Cherenkov radiation is 42 degrees.

In the 1KT detector, both charge and timing information of PMT signals is digitized by a front-end module, called an ATM [29]. One ATM processes 12

PMTs. The ATM generates an analog sum of PMT signals (PMTSUM) and a hit-sum signal whose pulse height is proportional to the number of hit PMTs (HITSUM). The analog sum of all PMTSUM signals from ID is recorded by 500 MHz flash-ADCs (FADCs) and a 100 MHz one. Since the ATM cannot separate multiple events within 1.2 μsec, we used the FADC data of the PMTSUM signal to select the single-interaction events. Then, we estimate the fraction of multi-interaction events by counting the number of peaks in the PMTSUM signal.

We use the 1KT data to measure the neutrino event rate at the near site, which is used to predict the event rate at SK. The neutrino energy spectrum is also measured combining with the data taken by the FGDs.

Fine-grain detectors

The FGD system consists of a scintillation fiber tracker (SciFi), a fully-active scintillator detector (SciBar), a lead glass calorimeter (LG) and a muon range detector(MRD). We measure the neutrino energy spectrum with the FGD system. For these studies, we analyze the data in which neutrinos interact with the SciFi and the SciBar. SciFi and SciBar are designed to have the tracking capability for all charged particles and particle identification. We use the MRD to measure the energy of a muon coming from SciFi and SciBar. With the LG detector, we measure the ν_e contamination in the beam.

The SciFi [30] consists of 20 scintillating fiber modules of 2.6×2.6m^2 in which 19 aluminum tanks filled with water are inserted between the modules as the target of neutrino interaction. Each module contains double layers of scintillating fiber sheets in both the horizontal and vertical directions. The scintillating fiber is 3.7 m long, 0.692 mm in diameter, and made of polystyrene. The water target tank is comprised of 15 rectangular pipes, each of which has dimensions of 16×6×240 cm^3 and a 1.8mm-thick aluminum wall. In total, the water target of SciFi is 6 tons.

The SciBar [31] was constructed as an upgrade of the near detector complex, replacing the LG in summer 2003. The main part of the SciBar detector consists of an array of plastic scintillator strips to realize a fully active detector with fine segmentation. Scintillators are coated with TiO_2 as the reflector, each of which have dimensions of $1.3 \times 2.5 \times 300$ cm^3. There are 14848 scintillator strips, and they are arranged into 64 layers. These features of the detector allows us to reconstruct all the charged particles produced in a neutrino interaction. With a tracking threshold of 8 cm, we can reconstruct protons (muons) with a momentum

greater than 450 MeV/c (100 MeV/c). The details of the SciBar detector are given in Appendix B. In the downstream part of SciBar, an electromagnetic calorimeter (EC) is installed. We analyze the EC data to study the electron neutrino fraction in the beam which contributes to the background of the $\nu_\mu \rightarrow \nu_e$ search. The measurement of the ν_e flux is described in Appendix B.

The MRD [32, 33] is located as the most downstream detector of the near detector complex. It consists of 12 iron absorbers sandwiched with 13 vertical and horizontal drift chamber layers. We employ the upper four iron plates of 10cm thickness to make the energy resolution of low energy muons better, while the other plates have a thickness of 20cm. The total thickness of iron is 2 m, corresponding to the range of 2.8 GeV/c muons.

2.2.4 Super-Kamiokande, the far detector

The Super-Kamiokande detector is a cylindrical 50 kton water Cherenkov detector located at Kamioka Observatory in Gifu Prefecture, 250 km from KEK. It is in the mine under Mt. Ikenoyama, where the mean rock overburden is 1000 m. This depth is equivalent to 2700 m of water, and the flux of cosmic rays is reduced by five orders of magnitudes compared to that on the surface of the earth.

The SK detector started taking data in April 1996, aiming for nucleon decay searches and studies of atmospheric and solar neutrinos. The running period of the first five years is referred to as SK-I. After being suspended for maintenance, an accident occurred in November 2001, which shattered 60% of the PMTs. The detector was rebuilt with a half of PMTs in December 2002 and the running period after the accident is called SK-II.

A schematic view of the detector is shown in Figure 2.10. The size of the water tank is 41.4 m in height and 39.3 m in diameter, which contains 50 ktons of pure water. The tank is optically separated into two concentric cylindrical regions by the support structure for the PMTs. The inner region, referred to as the inner detector (ID), contains 32 ktons of water and 11146 20-inch PMTs are attached inward on the support structure uniformly at intervals of 70 cm in the SK-I period. In SK-II, the number of PMTs was 5182. The photo-cathode coverage of the ID PMTs is 40% and 19% for SK-I and SK-II, respectively. A schematic view of a 20-inch PMT is shown in Figure 2.11. In SK-II, the PMT is covered by an acrylic cover around the photo-cathode and a fiber reinforced plastic (FRP) case for the rest. This is for prevention of damage through a chain reaction caused

by an implosion. The transparency of the acrylic cover in water is 98% for the wavelength longer than 400 nm and 95% for a 350 nm wavelength.

The outer region surrounding the ID is called the outer detector (OD). The thickness is 2.05 m on top and bottom and 2.2 m along the barrel. In this region, 1885 8-inch PMTs are mounted outward on the frame to veto incoming particles such as cosmic-ray muons. Furthermore, this 2 m thick water acts as a self-shielding against gamma-rays and neutrons entering from the rock. To enhance the light collection in OD, each PMT is equipped with a wavelength shifter plate.

The water in the tank is continuously circulated through the water purification system to keep the water properties stable. With this system, the attenuation length of the water has been kept at roughly 100 m. The system removes the radioactive materials, such as radon, from the water.

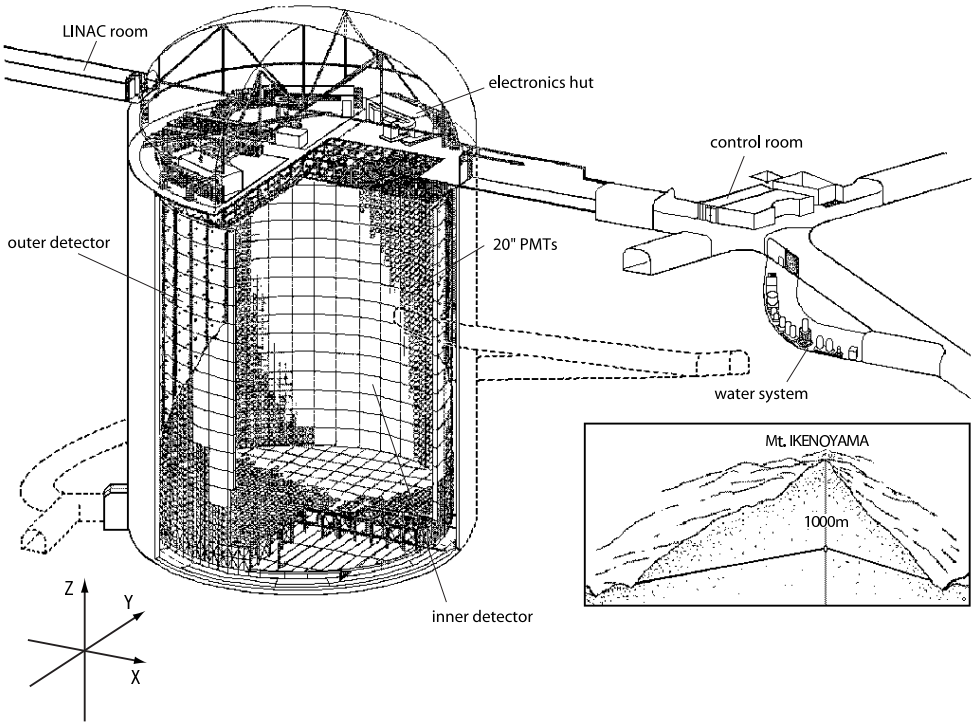

Figure 2.10: Schematic overview of the Super-Kamiokande detector

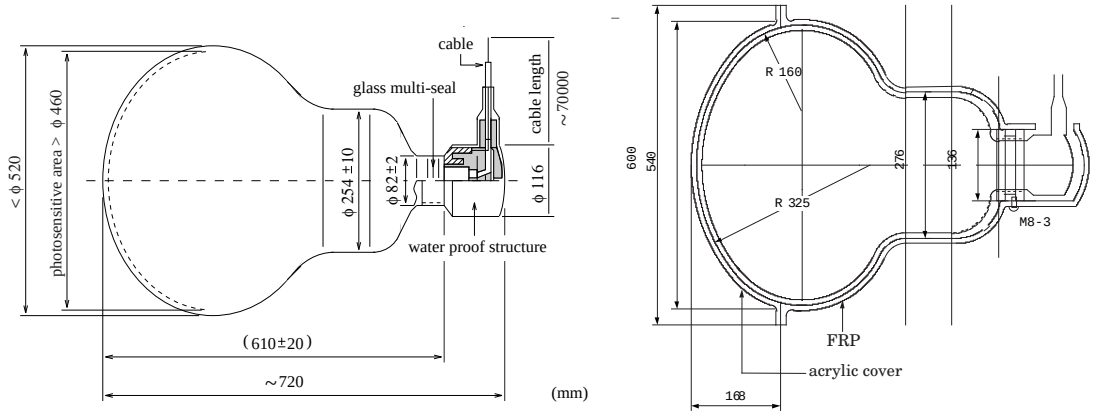

Figure 2.11: Schematic view of 20-inch PMT (left). The drawing of a PMT with an acrylic cover and a FRP case for SK-II is also shown (right).

2.2.5 Timing synchronization system

The timing synchronization between the accelerator and SK separates the beam neutrinos from atmospheric neutrino and cosmic-ray muon events in SK. For that purpose, the global positioning system (GPS) is employed. Figure 2.12 shows a schematic view of GPS system in the K2K experiment; it consists of GPS receivers, a VME receiver and a 50 MHz 32-bit local time clock (LTC). Receiving satellites' timing and position information, the GPS receiver provides the VME receiver and LTC with a time stamp every second. The VME receiver decodes the time stamp to universal time coordinate (UTC). The number of counts in the LTC is recorded simultaneously with receiving an event trigger signal. Identical sets of this system are located at KEK and at SK. For the stability monitoring of the system, two independent GPS receivers are employed at the near site.

2.3 Experimental phases and data sample

In the K2K experiment, there are two phases: K2K-I and K2K-II.

K2K-I corresponds to dates from June 1999 to July 2001 in which SK was instrumented with the full 11146 inner PMTs. K2K-I is further divided into two phases: K2K-Ia and K2K-Ib. For the K2K-Ia phase in June 1999, the horn current and the target diameter were different from the subsequent phases of experiment,

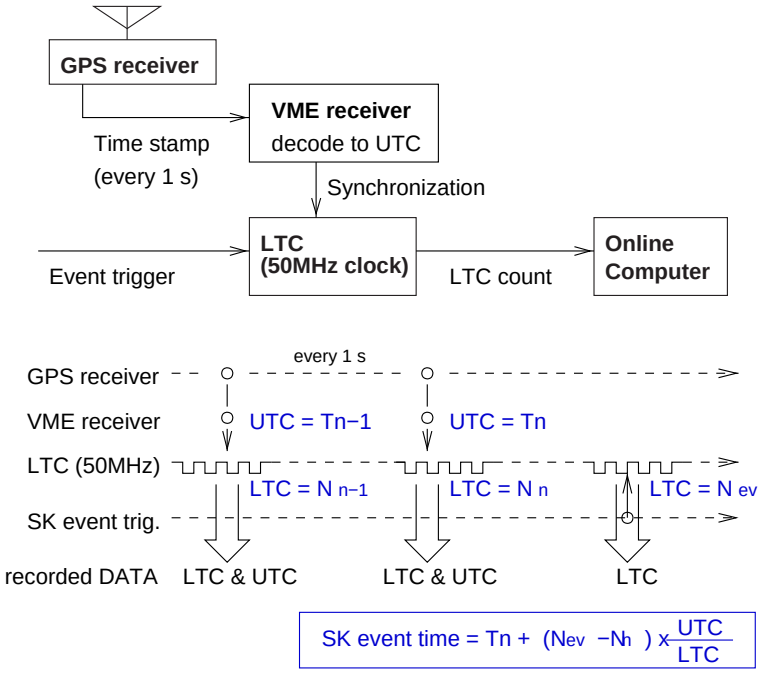

Figure 2.12: Schematic view and timing diagram of the GPS system. The time of an event in SK is estimated by linear interpolation with the UTC and LTC counts, as given in the formula.

which results in differences in the neutrino flux, far/near flux ratio, and systematic uncertainties.

K2K-II corresponds to dates with SK-II (January 2003 to November 2004). In the analysis of the FGDs for K2K-II, the phase is divided into two. The LG calorimeter was replaced by the SciBar detector, and correspondingly the period without the LG is called K2K-IIa (January 2003 to June 2003) and K2K-IIb (October 2003 to November 2004) with SciBar.

Figure 2.13 shows the number of delivered protons on the target. We achieved 10.5×10^{19} POT in total, of which 9.2×10^{19} with the good beam condition are used for analysis. The good beam condition is defined as follows:

- Data in normal experimental configurations except for the accelerator study, the beam tuning and the pion monitor measurement.
- All the beam-line components and the data acquisition are in good operation.
- A proton intensity is greater than 1.0×10^{12}protons/pulse, as a guarantee of the beam monitors' accuracy.
- Horn current is greater than 240 kA (190 kA) for K2K-Ib and K2K-II (K2K-Ia).
- Good GPS status both in KEK and SK.
- SK is in operation.

Experimental configurations of each phase are summarized in Table 2.1.

Table 2.1: Summary of the experimental configurations.

Phase	period	POT [10^{19}]	Target/horn	LG	SciBar	SK
K2K-I	**1999.6-2001.7**	**4.79**	—	set	—	SK-I
K2K-Ia	1999.6	0.31	ϕ20 cm/200 kA	↓	—	↓
K2K-Ib	1999.11-2001.7	4.48	ϕ30 cm/250 kA	↓	—	↓
K2K-II	**2003.1-2004.11**	**4.43**	↓	—	—	SK-II
K2K-IIa	2003.1-2003.6	2.26	↓	—	4 layers	↓
K2K-IIb	2003.10-2004.11	2.17	↓	—	64 layers	↓

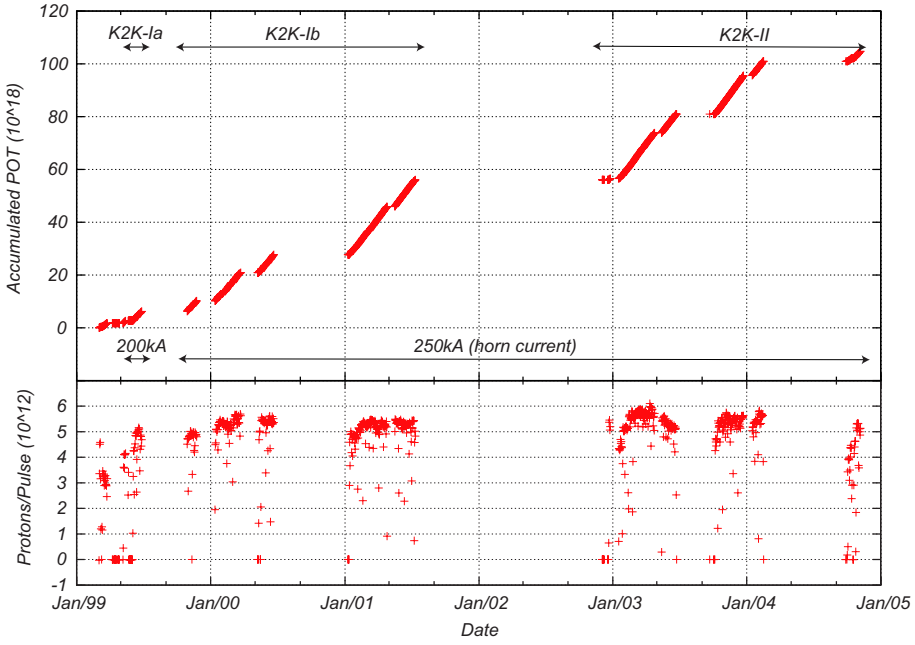

Figure 2.13: The integrated number of protons delivered to the target.

Chapter 3

Simulations

We use the Monte Carlo (MC) simulations to derive the expectations of neutrino events. Features of neutrino interactions, the methods of event reconstruction and the effects of systematic uncertainties are studied with the MC simulations.

The MC predictions of neutrino events are given by the following procedure:

(i) Neutrino flux calculation (beam MC),

(ii) Simulation of neutrino interactions with nuclei (NEUT),

(iii) Simulation of particle tracking in the detectors.

The detailed descriptions of each step are given in this chapter.

3.1 Neutrino flux calculation

The beam MC simulation reproduces the proton beam injection on the aluminum target, the secondary meson production and focusing by magnetic horns, and the tracking of secondary mesons until their decay to neutrinos.

3.1.1 Primary proton beam

To incorporate the beam properties into the beam MC simulation, we measure the profile of the primary proton beam with two SPICs located between the final focusing magnet and the target (V39-SPIC and TGT-SPIC). Based on this measurement, we estimate the beam profile and divergence at the target. The horizontal

beam spread of 1mm in standard deviation and the vertical spread of 6mm are estimated for the runs in June 1999 (K2K-Ia). In the period after November 1999 (K2K-Ib and K2K-II), the values of 3.4mm and 7.2mm are estimated for the horizontal and vertical spread, respectively. We use these values as the input to the beam MC simulation.

3.1.2 Pion production in the aluminum target

To predict the pion yield in $p - Al$ collisions, we adopt an empirical formula of Sanford-Wang which provides a quantitative description of the secondary particle production. This formula has eight parameters, and calculate the differential particle yield ($\frac{d^2n}{d\Omega dp}$) per interacting proton as

$$\frac{d^2n}{d\Omega dp} = C_1 p^{C_2} \left(1 - \frac{p}{p_B - 1}\right) \exp\left[-\frac{C_3 p^{C_4}}{p_B^{C_5}} - C_6\theta(p - C_7 p_B \cos^{C_8}\theta)\right], \qquad (3.1)$$

where θ is the angle of the secondary particle with respect to the beam axis in the laboratory frame, p and p_B are the momenta of the secondary particle and the primary proton, respectively, and $C_1, C_2, \cdots$, and C_8 are the parameters to be set. In this thesis, we adopt the pion production cross-section measured by the HARP experiment, described in Section 5.3. We fit the measured cross-section with the HARP measurement by the Sanford-Wang formula, and obtain the parameters of $C_{1,2,\cdots,8}$. For the flux predictions of the K2K-Ia period, we apply the compilation result given by Cho *et al.*(called Cho-CERN model [34, 35]). Adopting alternative models of GCALOR/FLUKA [36, 37, 38] and Sanford-Wang [39] or other available data [40, 41, 42, 43, 44, 34, 44], we estimate the systematic uncertainty.

For the kaon production, the Sanford-Wang formula with the parameter set described in Reference [39] is employed.

3.1.3 Particle tracking in the neutrino beam line

Survived primary protons and secondary particles are traced though the two magnetic horns down to the decay volume by using GEANT with the GCALOR hadron simulator. The effect of the magnetic field is also simulated.

The neutrino beam is made up via the decays of pions, kaons and muons. In the simulation, the following decay channels and their kinematics are simulated

for the ν_μ ($\bar{\nu}_\mu$) yield:

$$\begin{aligned}
\pi^{+(-)} &\rightarrow \mu^{+(-)} + \nu_\mu(\bar{\nu}_\mu) && [\pi^{+(-)}_{\mu 2}],\\
K^{+(-)} &\rightarrow \mu^{+(-)} + \nu_\mu(\bar{\nu}_\mu) && [K^{+(-)}_{\mu 2}],\\
K^{+(-)} &\rightarrow \pi^0 + \mu^{+(-)} + \nu_\mu(\bar{\nu}_\mu) && [K^{+(-)}_{\mu 3}],\\
K^0_L &\rightarrow \pi^{-(+)} + \mu^{+(-)} + \nu_\mu(\bar{\nu}_\mu) && [K^0_{\mu 3}],\\
\mu^{-(+)} &\rightarrow e^{-(+)} + \bar{\nu}_e(\nu_e) + \nu_\mu(\bar{\nu}_\mu) && [\mu^{-(+)}_{e3}].
\end{aligned}$$

For the ν_e ($\bar{\nu}_e$) flux, the following decays are simulated:

$$\begin{aligned}
\mu^{+(-)} &\rightarrow e^{+(-)} + \nu_e(\bar{\nu}_e) + \bar{\nu}_\mu(\nu_\mu) && [\mu^{+(-)}_{e3}],\\
K^{+(-)} &\rightarrow \pi^0 + e^{+(-)} + \nu_e(\bar{\nu}_e) && [K^{+(-)}_{e3}],\\
K^0_L &\rightarrow \pi^{-(+)} + e^{+(-)} + \nu_e(\bar{\nu}_e) && [K^0_{e3}].
\end{aligned}$$

3.1.4 Neutrino energy spectrum

Figure 3.1 shows the neutrino energy spectra at the near site and SK. Due to the difference of beam acceptance, the energy spectra are different between near and far sites. Figure 3.2 shows the energy spectrum for each neutrino type. The fraction of ν_μ, ν_e, $\bar{\nu}_\mu$, and $\bar{\nu}_e$ are 97.9%, 0.9%, 1.2%, and 0.02%, respectively, at SK, in the case of no oscillation. The composition of each decay process in ν_μ and ν_e is also shown in Figure 3.3. The main contributions to ν_μ is the decay of π^+ ($\pi^+_{\mu 2}$). For the ν_e flux, the main contribution comes from the muon decay μ^+_{e3} ($\sim$ 85%) and the rest comes from the kaon decays $K^{+,0}_{e3}$ ($\sim$ 15%).

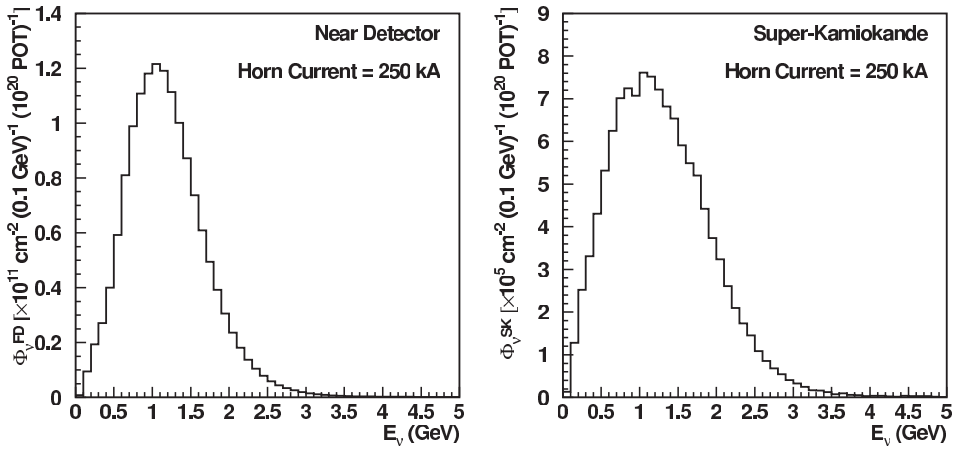

Figure 3.1: Neutrino energy spectra at the near site (left) and SK (right).

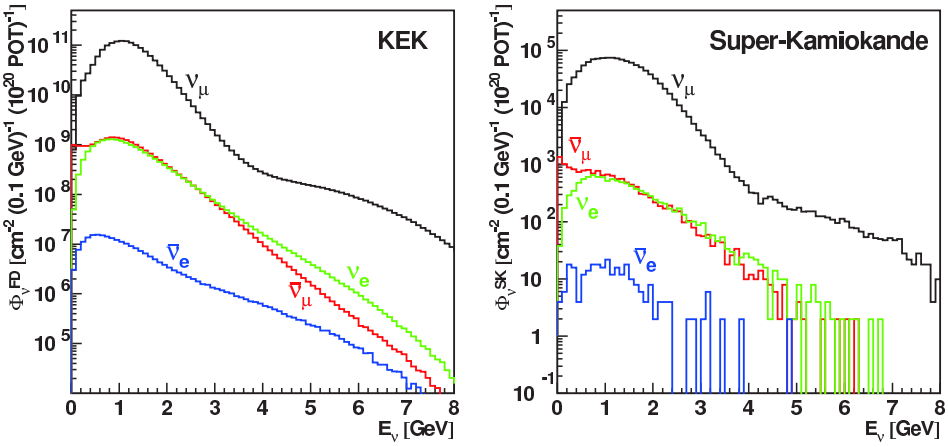

Figure 3.2: Neutrino energy spectra at the near site (left) and SK (right) for each neutrino type with 250 kA horn setting. Black, green, red, and blue lines show ν_μ, ν_e, $\bar{\nu}_\mu$, and $\bar{\nu}_e$, respectively.

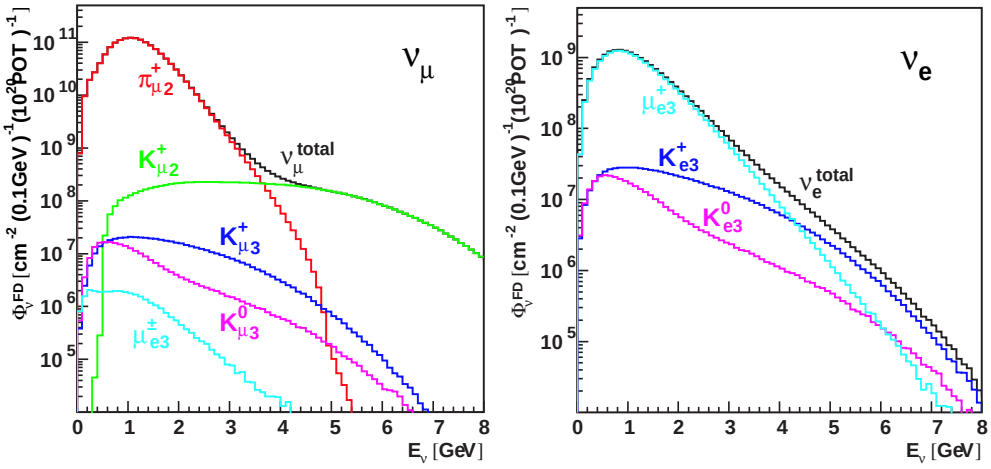

Figure 3.3: Composition of each decay process in ν_μ (left) and ν_e (right). The fluxes at the near site, according to the beam-MC simulation, are shown.

3.2 Neutrino interaction simulation

In the K2K experiment, neutrinos interact with nuclei and electrons in the water. The neutrino interactions are treated by the NEUT program library [45].

This library was originally developed for studies of atmospheric neutrinos in the Kamiokande experiment. In the code of the library, neutrino interactions with the target material are simulated. It provides the four-momentum of recoil or produced particles in the interaction.

In NEUT, the following charged current (CC) and neutral current (NC) interactions are taken into account:

- CC quasi-elastic scattering $\nu + N \rightarrow l^- + N'$ ($\sim 28\%$)
- NC elastic scattering $\nu + N \rightarrow \nu + N$ ($\sim 13\%$)
- CC resonance production $\nu + N \rightarrow l^- + N' +$ meson ($\sim 29\%$)
- NC resonance production $\nu + N \rightarrow \nu + N' +$ meson ($\sim 10\%$)
- CC multi-pion production $\nu + N \rightarrow l^- + N' +$ hadrons ($\sim 14\%$)
- NC multi-pion production $\nu + N \rightarrow \nu + N' +$ hadrons ($\sim 4\%$)
- NC coherent-pion production $\nu + {}^{16}\mathrm{O} \rightarrow \nu + {}^{16}\mathrm{O} + \pi^0$ ($\sim 1\%$)

where N and N' are nucleons and l^- is a charged lepton. The fraction of each mode, in the energy region of K2K neutrino beam, is also shown in parentheses. The details of neutrino interactions are given in Appendix A. The total cross-section of CC interactions consisting of quasi-elastic scattering (QE), single-meson productions and deep-inelastic scattering are shown in Figure 3.4. Figure 3.5 shows the cross-section of each interaction mode with water, calculated by NEUT.

3.2.1 Nuclear effects

Hadrons produced in a nucleus often interact with nuclear medium inside the nucleus, which results in the different final state or alters the kinematics of particles. These phenomena are called "nuclear effect". The nuclear effects of pions, nucleons, and Δ resonances are simulated in NEUT. The neutrino interaction position

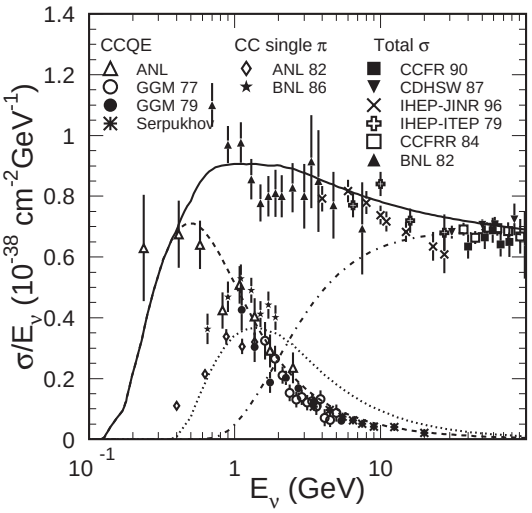

Figure 3.4: Total cross-section of CC interaction as a function of neutrino energy. Solid line shows the calculated total cross-section. The dashed, dotted and dash-dotted lines show the calculated cross-sections of QE, single-meson production and deep-elastic scattering, respectively. Data points are taken from various experiments.

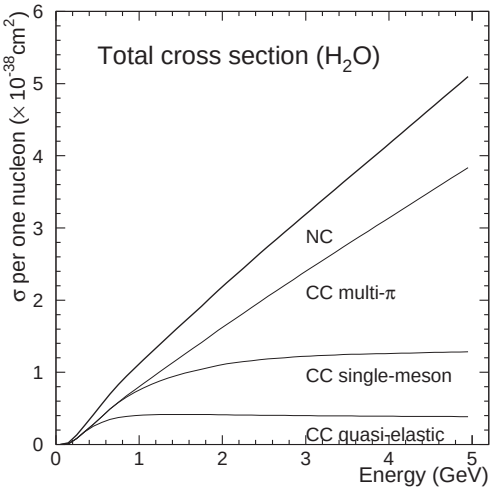

Figure 3.5: The cross-section of each neutrino interaction mode with water as a function of incident neutrino energy. The CC resonance production and CC coherent pion production modes are assorted in "CC single-meson".

in a nucleus is calculated using the Wood-Saxon type density distribution:

$$\rho(r) = \frac{Z}{A}\rho_0 \left\{1 + \exp\left(\frac{r-c}{a}\right)\right\}^{-1}, \tag{3.2}$$

where we choose $\rho = 0.48 m_\pi^3$, $a = 0.41$ fm, and $c = 2.69$ fm.

Pion

The nuclear effects for pions are classified into inelastic scattering, charge exchange and absorption. The cross-section is calculated by the model of L. L. Salcedo *et al.* [46]. The Fermi motion and the Pauli blocking effect of nucleons are taken into account in the similar way as CC-QE interaction. Figure 3.6 shows the calculated π^+-^{16}O interaction cross-section together with experimental data [47], which agree well with each other.

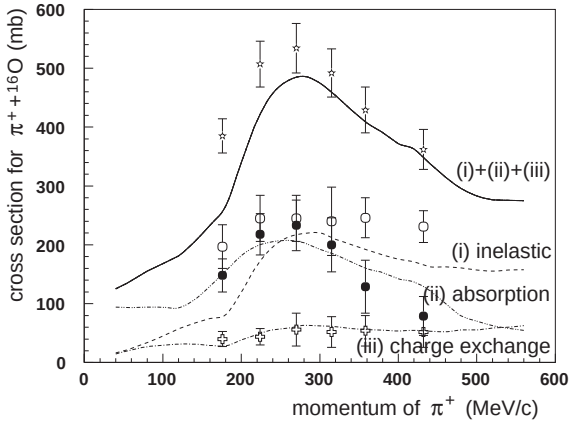

Figure 3.6: Cross-sections of π^+-^{16}O interactions. The lines show the results of our calculation of nuclear effect in NEUT based on [46], and the symbols show the experimental data [47]. Each interaction channel is illustrated in the figure.

Nucleon

The nucleon-nucleon elastic scattering cross-section implemented in NEUT is based on the measurement by H. W. Bertini [48], which is also used by GCALOR. We rescale the nuclear effect for nucleons by multiplying 0.9 to the measured cross-section by H. W. Bertini, which better reproduces the yield of scattered protons in $e - ^{12}$C interaction [49]. The pion production by nucleon is also taken into account, according to the isobar production model of S. J. Lindenbaum *et al.* [50].

Δ resonance

The absorption of a Δ resonance [51] is taken into account. Approximately 20% of the Δ resonances are lost by this effect.

3.3 Water Cherenkov Detector simulation

The particles generated in NEUT are traced by a detector simulation. The detector simulation is based on GEANT-3.2.1 package [52]. For the tracking of pions with momentum below 500 MeV, we refer the experimental data from $\pi - {}^{16}O$ scattering [53] and $\pi - p$ scattering [54].

In the water Cherenkov detector simulation, Cherenkov photons are generated according to the following equations of the half opening angle θ_C and the number of photons (N):

$$\cos\theta_C = \frac{1}{n\beta} \tag{3.3}$$

$$\frac{d^2N}{dxd\lambda} = \frac{2\pi\alpha}{\lambda^2}\left(1 - \frac{1}{n^2\beta^2}\right), \tag{3.4}$$

where n, β, x, λ and α are the refractive index of water, velocity ($= v/c$), the path length of a charged particle, the wavelength and the fine structure constant, respectively. For the propagation of Cherenkov photons, Rayleigh scattering, Mie scattering and absorption are taken into account. Attenuation coefficients used in the simulation are shown in Figure 3.7, which are tuned to reproduce the *in situ* measurement by a laser system and using cosmic-ray muons [55]. The quantum efficiency of PMT is implemented based on the measurement of single photoelectron distribution. Properties of the electronics system, timing width of ADC gate and signal threshold, are also simulated.

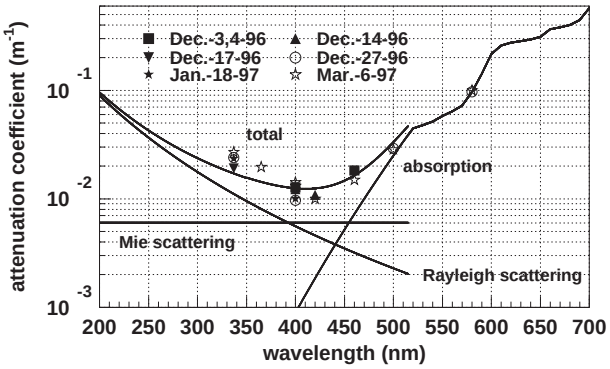

Figure 3.7: Attenuation coefficients as a function of wavelength in water. The data points are obtained from the light scattering measurement. The solid line shows a model in the simulation. The lines indicate the contribution of each process.

Chapter 4

Outline of analysis

We describe the signature of $\nu_\mu \rightarrow \nu_e$ oscillation signal events and background events in this chapter. We also describe the outline of the analysis procedure to extract the mixing parameter of $\nu_\mu \rightarrow \nu_e$ oscillation.

4.1 Signature of $\nu_\mu \rightarrow \nu_e$ oscillation

Our search for $\nu_\mu \rightarrow \nu_e$ oscillation is based on detection of charged current interaction of ν_e in an oxygen nucleus. Supposing that $\Delta m^2_{\mu e}$ is nearly $\Delta m^2_{\rm atm}$, the ν_μ oscillation probability is maximum with the neutrino energy of 0.6 GeV in K2K. In this energy region, quasi-elastic scattering $\nu_e + n \rightarrow e + p$ is the dominant process of interaction, in which the momentum of recoil proton is typically below the Cherenkov threshold in water. Therefore, only an electron is visible in SK. Electron events can be separated from muon events by the Cherenkov ring pattern. After the Cherenkov ring reconstruction, we select the single-ring events as a ν_e signal candidate because the separation between an electron and a muon becomes worse for multi-ring events mainly due to the overlapping of Cherenkov photons from multiple particles.

4.2 Background

After the neutrino event selection, the background originates from the beam neutrino interactions. Background of atmospheric neutrinos is negligible due to the good timing synchronization between the near and far sites by GPS. The

dominant source of background comes from the π^0 production in neutrino-^{16}O interactions. When one gamma-ray from π^0 decay is not reconstructed, the event is classified as a single-electron event, which is a signature of $\nu_\mu \rightarrow \nu_e$ oscillation. The typical event displays of ν_e CC-QE interaction and π^0 production background are shown in Figure 4.1. Supposing that θ_{13} is near the current limit of ~ 0.1 at $\Delta m^2 = 2.8 \times 10^{-3}$ eV^2, we obtain an oscillation probability for $\nu_\mu \rightarrow \nu_e$ in K2K of $\sim 10^{-2}$, which gives the expectation of a few ν_e signal events in our entire data sample. Thus, the understanding of π^0 background and the reduction are quite critical. For this purpose, we have developed a new reconstruction algorithm of π^0.We apply the π^0 rejection cut to the K2K data sample using the π^0 reconstruction algorithm.

The remaining background events originate from the contamination of ν_e in the beam (beam ν_e). This is not intrinsically reducible. The beam-ν_e contamination in the beam at SK is estimated to be 1.2%.

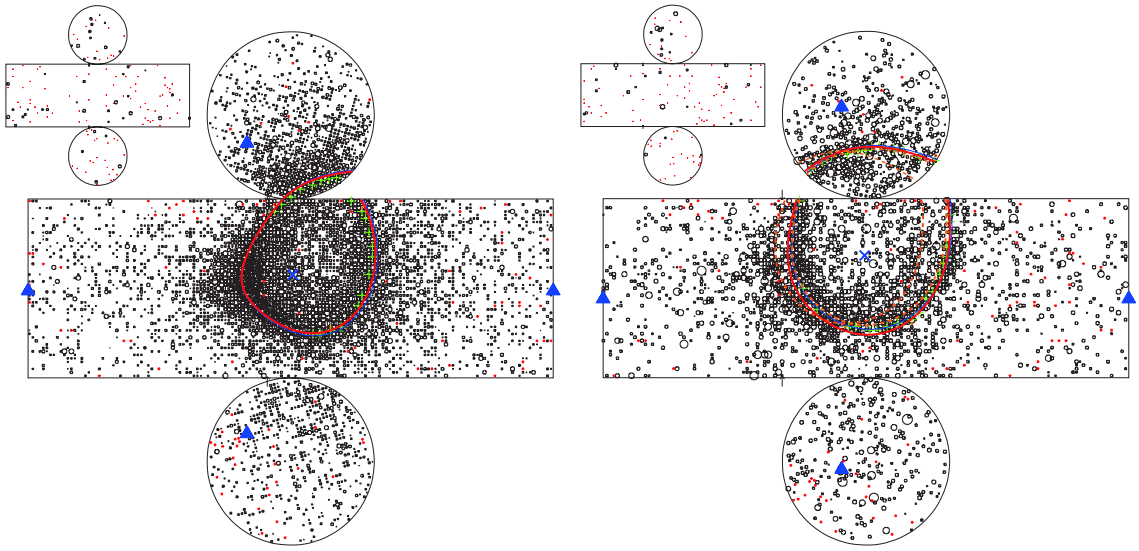

Figure 4.1: Typical event displays of ν_e CC-QE interaction (left) and π^0 production background (right). The solid lines show the reconstructed Cherenkov rings. In the right figure, the two dashed lines show the expected ring projections according to the vertices and directions of gamma-rays from a π^0 decay.

4.3 Search for $\nu_\mu \rightarrow \nu_e$ oscillation

To search for $\nu_\mu \rightarrow \nu_e$ oscillation, we look for the excess of ν_e appearance signal by comparing the observed number of signal candidate events with the expected number of background events. Since the absolute neutrino neutrino flux and its cross-section have large uncertainties, we derive the expected number of signal (background) events at SK from the total number of neutrino interactions (N_{SK}) and the MC event rate predictions as:

$$N_{SK} \times \frac{\text{MC event rate of } \nu_e \text{ signal (background)}}{\text{MC total event rate without oscillation}}. \tag{4.1}$$

First, we estimate the total number of neutrino events in SK in the case of no oscillation (Chapter 5). To calculate N_{SK}, we perform the following measurements:

- Neutrino interaction rate at the 1KT detector,
- Neutrino energy spectrum at the near site,
- Pion production cross-section in the $p - Al$ collisions.

The *in situ* measurement of charged pions in $p - Al$ collisions is performed in the HARP experiment. Using the HARP results as the input to the MC simulation, we calculate the far/near flux ratio. We then extrapolate the measured neutrino interaction rate and energy spectrum at the near site to SK by multiplying the far/near flux ratio.

Next, applying the event selection (Chapter 6, 7), we compare the observed number of signal candidate events with the background expectation.

Finally, we give a constraint on the oscillation parameters of $\sin^2 2\theta_{\mu e}$ and Δm^2 from the obtained $\nu_\mu \rightarrow \nu_e$ oscillation probability with a statistical approach (Chapter 8, 9).

Chapter 5

Expected number of beam neutrino events at SK

We predict the number of neutrino events at SK when there is no oscillation. For the prediction, we use the neutrino interaction rate measured by 1KT. We also measure the neutrino energy at the near site and extrapolate it to SK with the far/near flux ratio.

In this chapter, we follow four steps as

(i) Measurement of neutrino event rate at 1KT,

(ii) Measurement of neutrino energy spectrum at near detectors,

(iii) Near-to-far spectrum extrapolation,

(iv) Prediction of the number of neutrino events at SK.

5.1 Neutrino interaction rate at the 1KT detector

In order to predict the number of neutrino events at SK, we measure the neutrino interaction rate at the 1KT detector. The 1KT detector uses the same detector technology as SK, and the event reconstruction algorithm of 1KT is also similar to that of SK. Therefore, when we compare the observed number of events in SK with the expected one from 1KT, most of the systematic uncertainties, such as neutrino interaction cross-sections and the detection efficiencies, cancel out.

In the 1KT detector, multi neutrino interactions occur in a spill due to the intense neutrino beam; the fraction of multi-interaction events in the total spills

is approximately 10%. Because we cannot reconstruct multi-interaction events properly, we estimate the neutrino interaction rate from the number of single-interaction events inside the fiducial volume by correcting the fraction of multi-interaction event. For this purpose, we count the number of peaks in the sum of the pulse height information of all PMTs recorded by FADC. We then evaluate the correction factor of $N_{int}^{total}/N_{peak}^{single}$, where N_{int}^{total} and N_{int}^{single} are the total number of FADC peaks of events and the number of single FADC peak events, respectively. The number of neutrino events in 1KT (N_{int}^{1KT}) is expressed as

$$N_{1KT}^{int} = N_{1KT}^{select} \cdot \frac{N_{peak}^{total}}{N_{peak}^{single}} \cdot \frac{1}{\epsilon_{1KT}} \tag{5.1}$$

where N_{1KT}^{select} and ϵ_{1KT} are the number of single-interaction events and the event selection efficiency, respectively. Descriptions of the event selection criteria and the corrections are given in the following sections.

5.1.1 Event selection in the 1KT detector

The single-interaction neutrino events in 1KT are selected with the following requirements:

(i) There is no event 1.2 μsec before the beam timing,

(ii) The total number of photoelectrons is greater than 200 (equivalent to approximately 20 MeV),

(iii) Good beam condition (described in Section 2.3) is satisfied,

(iv) FADC pulse height is greater than 1000 photoelectrons (equivalent to approximately 100 MeV),

(v) Only one FADC peak in a spill is observed,

(vi) The vertex is reconstructed in the fiducial volume.

Because the 1KT detector cannot record events properly when two events occur within a short time interval, we apply the criterion (i). The criterion (ii) rejects low-energy events which could not be reconstructed, and (iv) is applied to reject events of decay-electrons from stopped muons in the detector. Because the reconstruction

algorithm cannot find the vertices of each event properly for the multi-interaction event, we select the single-interaction event with the criterion (v). After the event reconstruction, we select the events whose vertices are inside the fiducial volume. Figure 5.1 shows the fiducial volume of the 1KT detector; it is defined as a cylindrical volume along the beam direction with a radius of 2 m and a height of 2 m, and located 1 m upstream from the center of the tank. The fiducial mass corresponds to 25 tons. Detailed descriptions of the event selection are given in Reference [56].

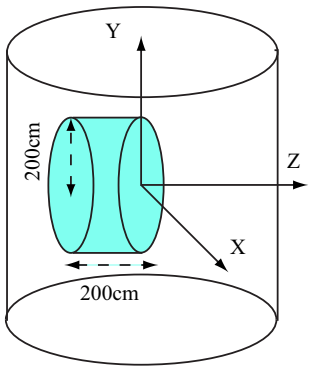

Figure 5.1: Fiducial volume of the 1KT detector.

Figure 5.2 shows the event selection efficiency as a function of neutrino energy, estimated by the MC simulation. The averaged efficiency is estimated to be 75%.

5.1.2 Corrections on N_{1KT}^{select}

- **Correction of background contamination:**
  There are background events from cosmic-ray muons and beam-induced particles which are generated by neutrino interactions in the surrounding materials. The fraction of background events due to the cosmic-ray muons is estimated to be 1.0% with the data taken by the random trigger. The beam induced background event has a PMT hit cluster in the OD region originated from the incoming particle. We have performed a visual scan for the OD-PMT hits to estimate the fraction of beam-induced background. It is estimated to be 0.5 %. The total background contamination is estimated to be 1.5% by including small contributions from another background sources [56]. The background events are subtracted from the number of selected events.

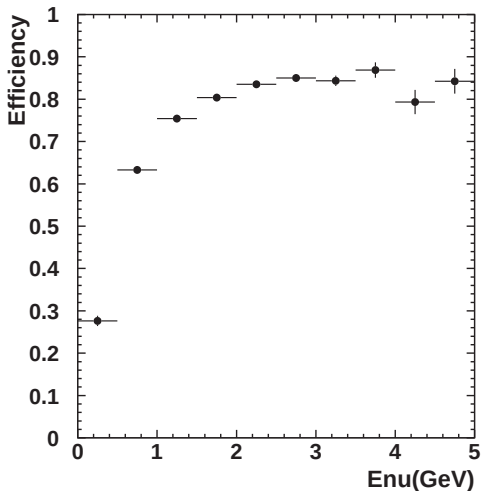

Figure 5.2: Event selection efficiency of 1KT as a function of neutrino energy.

- **Correction for multi-interaction events:**
  If neutrino interactions occur within one bunch, we cannot identify multi-interaction events by the FADC peak counting. To estimate the mis-identification probability of multi-interaction events as single-interaction events, we employ the MC simulation which reproduces the FADC pulse-height distribution of multi-interaction events. Comparing the number of FADC peaks with the MC events, we estimate the correction factor for multi-interaction events happened in one bunch to be 1.008.

5.1.3 Event rate summary

We obtain the neutrino interaction rate at 1KT with the procedure described above. The numbers of neutrino interactions for each experimental period are summarized in Table 5.1. The neutrino interaction rate as a function of running time in the 1KT detector is shown in Figure 5.3. The event rate is stable within the fluctuation of 6%.

5.1.4 Systematic uncertainty

The systematic uncertainty of the 1KT event rate is estimated to be 4.1%. The dominant source comes from the uncertainty in the fiducial volume. To evaluate

Table 5.1: Summary of event rate measurements in the 1KT detector.

Period	$POT_{1KT}(10^{18})$	N^{select}_{1KT}	N^{total}_{peak}	N^{single}_{peak}	N^{int}_{1KT}
K2K-Ia	2.6	4282	109119	89782	7206
K2K-Ib	38.2	75973	1854781	1475799	130856
K2K-II	33.9	83529	2012446	1588669	140268

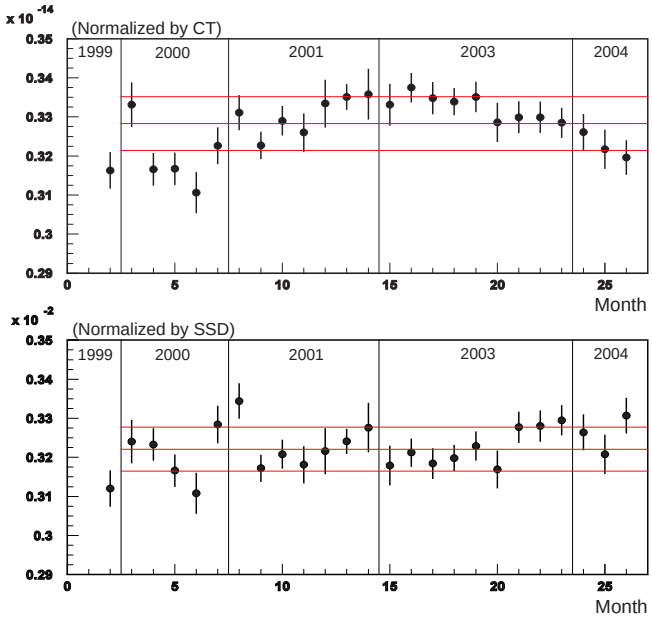

Figure 5.3: The event rate per month in the 1KT detector. The event rate is normalized by POT measured by TGT-CT (upper) and SPD (lower). The middle line shows the average and the interval between the lines shows the RMS of the event rate, which is 2.0% (1.6%) for the upper (lower) figure. The full spread is approximately 6%.

Source	Error (%)
Fiducial volume	± 3.0
Energy scale	± 0.3
FADC stability	± 0.8
FADC cut position	± 1.5
FADC error	± 1.0
Event rate	± 1.6
Background	± 0.5
Multi-interaction	± 0.7
Total	± 4.1

Table 5.2: Sources of systematic error on N^{int}_{1KT}.

this uncertainty, we have studied the performance of the vertex reconstruction using cosmic-ray muons [57]. We found a bias on the reconstructed vertices less than 4 cm, and estimate the uncertainty of the fiducial volume to be 3%. Other sources of systematic uncertainty are the energy scale, the FADC gain stability and the threshold, corrections on N^{1KT}_{select}, the event rate stability and the beam profile. All the uncertainties are summarized in Table 5.2. Details of all the sources are described in Reference [56].

5.2 ν_μ energy spectrum measurement at the near site

For the measurement of the neutrino energy spectrum before neutrinos oscillate, we use the CC interaction events in 1KT, SciFi and SciBar. The neutrino energy is reconstructed from the muon momentum (p_μ) and angle with respect to the beam direction (θ_μ) by assuming QE interaction as

$$E_\nu = \frac{m_p^2 - (m_n - V)^2 - m_\mu^2 + 2(m_n - V)E_\mu}{2(m_n - V - E_\mu + p_\mu \cos\theta_\mu)}, \tag{5.2}$$

where m_p, m_n, m_μ, E_μ and V are the proton mass, the neutron mass, the muon mass, the muon energy and the nuclear potential energy (27 MeV for ^{16}O), respectively. The two-dimensional distributions of p_μ versus θ_μ are used to measure the neutrino energy spectrum.

χ^2 fitting

The observed p_μ-θ_μ distributions are compared with the MC expectations by a χ^2 fitting method, treating the neutrino energy spectrum in the MC simulation as fitting parameters. Here we give an example of the procedure in the 1KT detector. The $p_\mu - \theta_\mu$ distribution with the MC expectation is shown in Figure 5.4. The neutrino energy in GeV is divided into eight bins: 0.0-0.5, 0.5-0.75, 0.75-1.0, 1.0-1.5, 1.5-2.0, 2.0-2.5, 2.5-3.0 and above 3.0. For the MC expectation, the $p_\mu - \theta_\mu$ distribution is prepared for each E_ν bin and separately for QE interactions and other than QE (non-QE); 8×2 distributions are prepared in total for each event sample. The free parameters in the fit are the weighting factors of neutrino energy spectrum to the MC events for eight energy bins ($f_1^\phi, ..., f_8^\phi$) and a parameter R_{nQE} which represents the relative weighting of CC non-QE events to CC-QE events. The χ^2 functions are separately defined for each detector and then summed to build a combined χ^2 function as

$$\chi^2 = \chi^2_{\mathrm{1KT}} + \chi^2_{\mathrm{SF}} + \chi^2_{\mathrm{SB}}, \tag{5.3}$$

where χ^2_{1KT}, χ^2_{SF} and χ^2_{SB} are χ^2 for 1KT, SciFi and SciBar, respectively. A set of the fitting parameters is found by minimizing the χ^2 function. Details of the event selection and the fitting procedure in each detector are given in References [56,58, 59,60,61]. Here only the results of measurement are given.

5.2.1 Measured neutrino energy spectrum at near site

The best-fit values of parameters given by the combined data sample are shown in Table 5.3. We have checked the results of the measurements with individual detector data: all the fitting parameters are in good agreement within their errors each other. The measured energy spectrum with the combined data shows a good agreement with that with each detector sample. We also confirmed that the MC simulation with the fitted parameters well reproduces all the distributions for each detector, such as p_μ, θ_μ and momentum transfer squared q^2 ($\equiv 2E_\nu(E_\mu - p_\mu \cos\theta_\mu)$, assuming QE interaction). For the resultant R_{nQE}, we evaluate the uncertainty of R_{nQE} to be 20% by comparing the combined result with the results of each detector.

The measured neutrino spectrum is shown in Figure 5.5. The error matrix representing correlations between the spectrum parameters f_i^Φ and R_{nQE} is also shown in Table 5.4. The neutrino energy spectrum is used as the input to predict

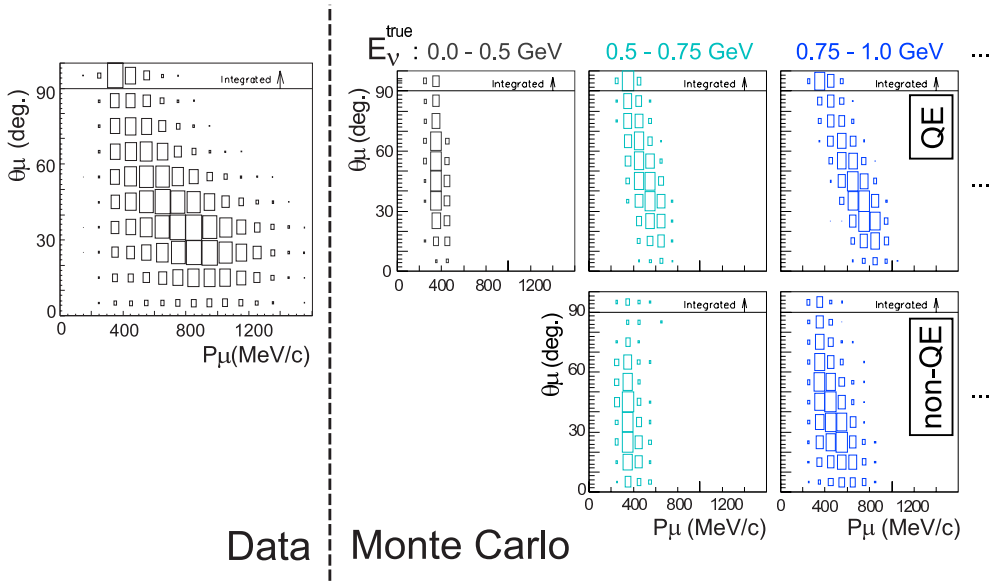

Figure 5.4: $p_\mu - \theta_\mu$ distributions.

the neutrino spectrum at SK, and the errors and correlations are used in $\nu_\mu \to \nu_e$ oscillation analysis, which is described in Chapter 8 and 9.

Table 5.3: Results of the spectrum measurement. The best fit value of each parameter is listed for the fits with all the detectors data. The reduced χ^2 ($\chi^2_{\rm total}$/DOF) is also shown. (The parameters $f_1^\Phi, \cdot, f_8^\Phi$ and $R_{\rm nQE}$ are the weighting factors to the MC events.)

parameter	
f_1^Φ (0.00-0.50)	1.657 ± 0.437
f_2^Φ (0.50-0.75)	1.107 ± 0.075
f_3^Φ (0.75-1.00)	1.154 ± 0.061
f_4^Φ (1.00-1.50)	≡ 1
f_5^Φ (1.50-2.00)	0.911 ± 0.044
f_6^Φ (2.00-2.50)	1.069 ± 0.059
f_7^Φ (2.50-3.00)	1.152 ± 0.142
f_8^Φ (3.00-)	1.260 ± 0.184
$R_{\rm nQE}$	0.964 ± 0.20
$\chi^2_{\rm total}$/DOF	1.17(=687.2 / 585)

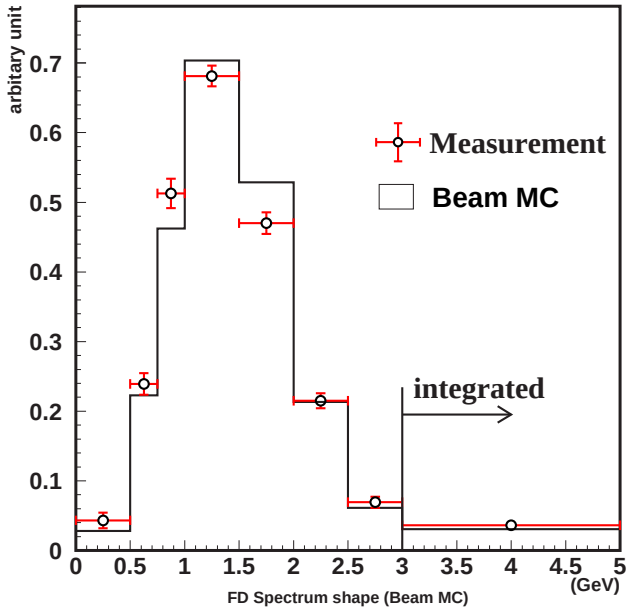

Figure 5.5: The neutrino energy spectrum measured at near detectors (open circles). The expectation with the beam MC simulation is also shown (histogram).

Table 5.4: The error matrix for $f_{i\Phi}$ and R_{nQE}. The square root of error matrix is shown here in the unit of %.

	f_1^Φ	f_2^Φ	f_3^Φ	f_4^Φ	f_5^Φ	f_6^Φ	f_7^Φ	f_8^Φ	R_{nQE}
f_1^Φ	43.86	-3.16	7.28	-	-2.21	-0.76	-3.48	0.81	-8.62
f_2^Φ	-3.16	7.51	1.97	-	1.90	0.62	1.29	2.43	-5.68
f_3^Φ	7.28	1.97	6.00	-	3.38	1.63	3.44	1.71	-2.99
f_4^Φ (fixed)	-	-	-	-	-	-	-	-	-
f_5^Φ	-2.21	1.90	3.38	-	4.04	-1.86	4.53	2.20	1.65
f_6^Φ	-0.76	0.62	1.63	-	-1.86	5.28	-5.85	5.11	0.94
f_7^Φ	-3.48	1.29	3.44	-	4.53	-5.85	13.67	-10.14	4.09
f_8^Φ	0.81	2.43	1.71	-	2.20	5.11	-10.14	18.35	-11.77
R_{nQE}	-8.62	-5.68	-2.99	-	1.65	0.94	4.09	-11.77	20.30

5.3 Near-to-far spectrum extrapolation

Due to the finite size of the π decay volume and the detectors, the neutrino flux is not simply proportional to L^{-2}, where L is the distance from the target (Appendix C). Therefore, we need to evaluate the energy-dependent flux ratio between SK and the near site, $R_{F/N} \equiv \Phi^{\nu_\mu}_{SK}/\Phi^{\nu_\mu}_{ND}$, to extrapolate the near detector measurement to SK, where Φ_{SK} and Φ_{ND} are the neutrino fluxes at SK and the near site, respectively. In the current analysis, we adopt a measurement of pion production cross-section in $p - Al$ collisions by the HARP experiment for the flux prediction.

5.3.1 The HARP experiment

For the neutrino flux prediction in the previously published results [62, 63, 18], we adopted the beam MC simulation based on the Cho-CERN pion production model. It was validated by the *in situ* measurement of pions by the pion monitor [28]. However, in the uncertainty of ν_μ energy spectrum at SK, a dominant contribution has originated from the uncertainty of $R_{F/N}$ which comes from the uncertainty of pion production in primary $p - Al$ collisions.

For the precise measurement of pion production and the far/near flux ratio, the HARP experiment was conducted at CERN. HARP comprises the same proton beam momentum (12.9 GeV/c) as K2K and an aluminum target. The HARP detector consists of forward and large-angle detection systems, as shown in Figure 5.6. In the large angle region, a time projection chamber (TPC) is located in a solenoid magnet. The forward spectrometer is built around a dipole magnet with magnetic field of 0.66 T with large planar drift chambers (NDCs), a time-of-flight wall (TOFW), a threshold Cherenkov detector (CHE) and an electromagnetic calorimeter (ECAL). The aluminum target is located inside TPC. A detailed description of the HARP experiment is given in References [64, 65]. The forward spectrometer covers the angular range of produced pions from 30 mrad to 210 mrad and the momentum range from 0.75 GeV/c to 6.5 GeV/c, which agree with the dominant phase space of the pion production contributing to the K2K neutrino beam. Therefore, in HARP, we measure the cross-section of pion production relevant to the K2K far/near flux ratio.

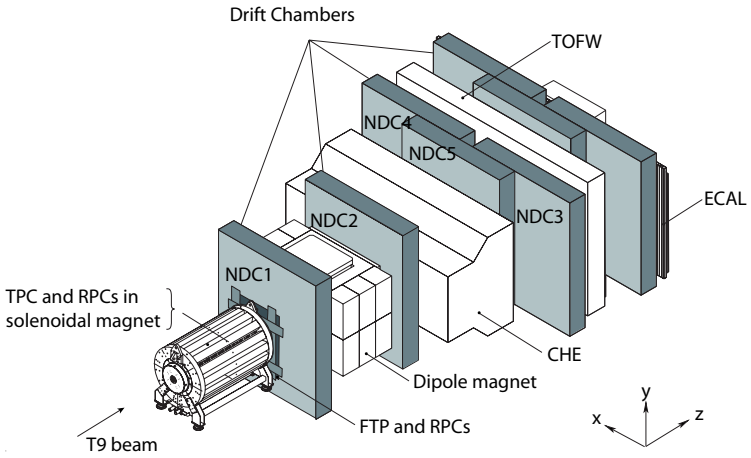

Figure 5.6: Schematic view of the HARP detector.

5.3.2 Neutrino flux prediction

The pion production cross-section is formalized by the Sanford-Wang formula as expressed in Equation 3.1. The Sanford-Wang parameters for the *Al* target are measured by fitting the HARP data with the formula. The best-fit parameters and the differential cross-sections of pions are shown in Table 5.5 and Figure 5.7. The details of the HARP analysis are described in Reference [66].

Table 5.5: Parameters of the Sanford-Wang differential cross-section formula obtained by fitting the HARP data.

C_1	C_2	C_3	$C_4 = C_5$	C_6	C_7	C_8
4.4×10^2	$8.5 \times 10^{-}1$	5.1	1.78	4.43	1.35×10^{-1}	3.57×10^1

The production cross-section of pions measured by the HARP experiment is used to predict the neutrino fluxes in the beam MC simulation. Figure 5.8 and 5.9 show the ν_μ flux predictions at the near site and SK, and the ratio of them, respectively. The predictions based on the Cho-CERN pion production model are also shown for comparison. The new predictions are in a good agreement with the previous ones.

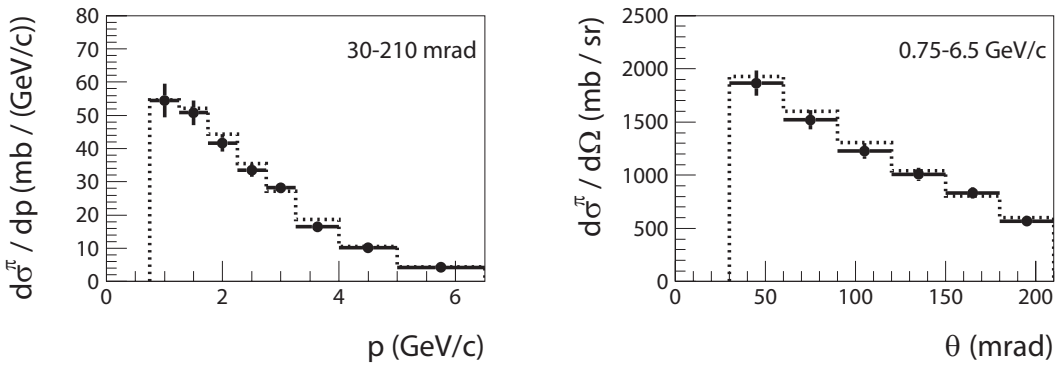

Figure 5.7: The differential cross-section of pions as a function of the pion momentum integrated over the pion angular range of 30 mrad $< \theta <$ 210 mrad, and as a function of θ in the pion momentum range of 0.75 GeV/c $< p <$ 6.5 GeV/c. The points show the HARP measurements. Also shown with the dotted lines are the Sanford-Wang formula with the HARP best-fit parameters.

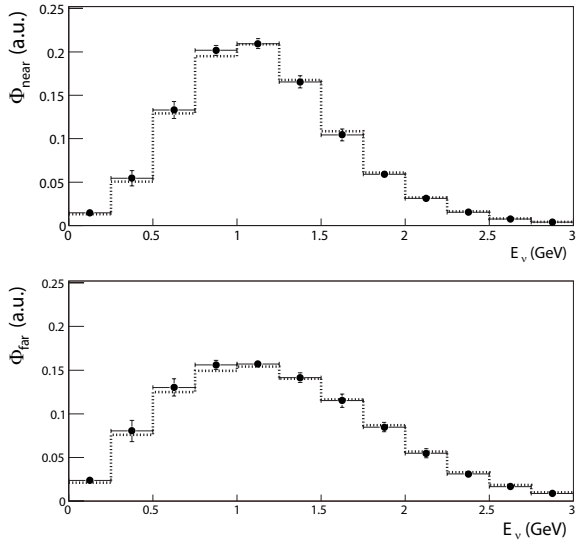

Figure 5.8: ν_μ fluxes at the near site (top) and SK (bottom) as a function of neutrino energy predicted by the beam MC simulation with the HARP measurement (circles with error bars) and the Cho-CERN model (dotted histograms). The histograms are normalized to be unit in the integration.

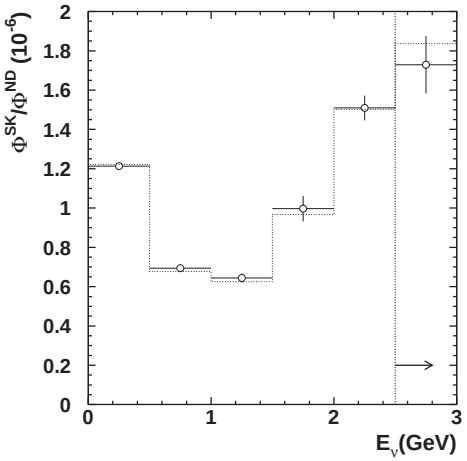

Figure 5.9: Ratio of ν_μ flux at SK to the near site predicted by the beam MC simulation. The HARP prediction and the prediction based on the Cho-CERN hadronic model are shown by the open circles with error bars and the dotted histogram, respectively. The arrow shows that the contents in last bin are integrated over all neutrino energies above 2.5 GeV.

5.3.3 Systematic uncertainty

The systematic uncertainties in the ν_μ flux prediction for each neutrino energy bin are estimated here, with the error matrix ($M_{F/N}$) including the correlation among different energy bins.

We consider the uncertainties associated with the following objects:

- primary beam optics,
- primary hadronic interactions of protons,
- secondary hadronic interactions,
- horn magnetic fields.

For the beam optics parameters, we take into account the uncertainties in the impact point at the target, the injection angle, the profile width and the angular divergence. They are evaluated from the beam profile measurement by the ionization chambers of V39-SPIC and TGT-SPIC (Section 2.2.1).

Second, we consider the effect of the uncertainties in our understanding of primary hadronic interactions. In the $p - Al$ hadronic interaction length, we assume

an uncertainty of 30% in the simulation. The uncertainty in the multiplicity and kinematics of pion production is estimated by using the uncertainties and correlations in the Sanford-Wang parameters given by the HARP result [66]. For the production cross-section of charged and neutral kaons, we quote an uncertainty of 50%.

Third, the effect of interactions of the secondary particles (*e.g.*, inelastic scattering, absorption and charge exchange of pions) is estimated by adopting an alternative model. We evaluate the difference of fluxes between the GCALOR/FLUKA model and GHEISHA model [67], and also compare them with the available experimental data.

Finally, we consider the uncertainties due to the magnetic field in the horn system, field strength and field homogeneity in azimuth. The uncertainty of the field strength and the azimuthal field perturbation is evaluated based on the measurement of the magnetic field using inductive coils as in Reference [68]. We estimate the uncertainties of 10% and 15% for the field strength and perturbation, respectively.

Varying the parameters and cross-sections by their estimated errors in the beam MC simulation, the uncertainty of the far/near flux ratio is estimated. The estimated systematic uncertainties of $R_{F/N}$ is summarized in Table 5.6. We also obtain the 6×6 error matrix $M_{F/N}$ as follows:

$$sign(M_{F/N}) \cdot \left|M_{F/N}\right|^{1/2} = \tag{5.4}$$

	0.0 – 0.5	0.5 – 1.0	1.0 – 1.5	1.5 – 2.0	2.0 – 2.5	> 2.5
0.0 – 0.5	1.4	0.2	−0.6	−1.9	−1.7	1.6
0.5 – 1.0	0.2	2.7	3.0	3.7	2.6	−3.7
1.0 – 1.5	0.6	3.0	3.6	4.6	3.2	4.5
1.5 – 2.0	−1.9	3.7	4.6	6.5	4.7	−6.2
2.0 – 2.5	−1.7	2.6	3.2	4.7	4.2	−5.2
> 2.5	1.6	−3.7	−4.5	−6.2	−5.2	8.5

The binning of neutrino energy is same as in Figure 5.9 and the values are in the unit of %.

5.3.4 Estimated neutrino energy spectrum at SK

Multiplying the measured energy spectrum at near detectors by the far/near flux ratio, we obtain the expected ν_μ energy spectrum at SK in the case of no oscillation;

Table 5.6: Summary of the systematic error sources in the far/near flux ratio prediction. The errors are in %.

Category	Error source	$\Delta R_{F/N}$
Beam optics	Centering	0.03
	Aiming	0.03
	Spread, divergence	0.75
	Sub-total	**0.76**
Primary hadronic interaction	interaction rate	0.63
	Kinematics of π production	1.43
	Multiplicity of kaons	0.23
	Sub-total	**1.58**
Secondary hadron interaction		0.71
Horn magnetic field	Strength	0.52
	Azimuthal field perturbation	0.34
	Sub-total	**0.62**
	Total	**1.99**

it is shown in Figure 5.10. The expected energy spectrum of ν_e oscillated from ν_μ with the oscillation parameters $\sin^2 2\theta_{\mu e} = 1.0$ and $\Delta m^2 = 2.8 \times 10^{-3}$ eV^2 is also shown.

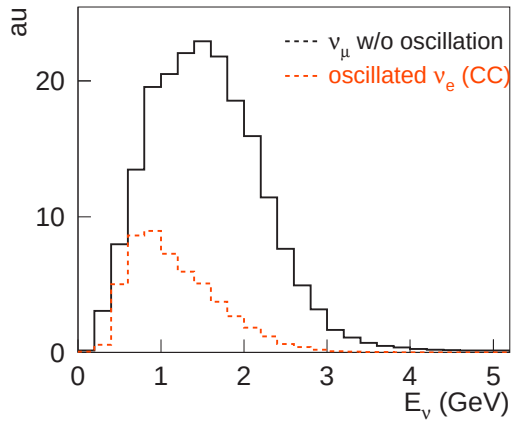

Figure 5.10: Expected neutrino energy spectrum at SK. The histogram shows the ν_μ energy spectrum without oscillation and the dashed one shows the ν_e energy spectrum via CC interaction assuming $\sin^2 2\theta_{\mu e} = 1.0$ and $\Delta m^2 = 2.8 \times 10^{-3}$ eV^2.

5.4 Prediction of the number of neutrino events at SK

We estimate the number of neutrino interactions in SK, which is used for normalization.

The expected number of neutrino events at SK (N_{SK}) without oscillation is derived from the 1KT event rate extrapolated by using the far/near flux ratio, live time and fiducial mass of SK and 1KT. The formulation is expressed as

$$N_{SK} = N_{1KT}^{int} \cdot R^{int} \cdot \frac{M_{SK}}{M_{1KT}} \cdot \frac{POT_{SK}}{POT_{1KT}} \cdot C_{\nu_e} \cdot \epsilon_{SK}^{FCFV}, \tag{5.5}$$

$$R^{int} = \frac{\int dE_\nu \Phi_{SK}(E_\nu) \cdot \sigma(E_\nu)}{\int dE_\nu \Phi_{1KT}(E_\nu) \cdot \sigma(E_\nu)}, \tag{5.6}$$

where

N^{int}_{1KT} : The number of neutrino interactions in 1KT (Equation 5.1),
Φ_{SK} : The neutrino flux at SK,
Φ_{1KT} : The neutrino flux at 1KT,
M_{SK} : The fiducial mass of SK (22.5 ktons, described in Section 6.1),
M_{1KT} : The fiducial mass of 1KT (25 tons),
POT_{SK} : The number of protons on target which corresponds to the analyzed data in SK,
POT_{1KT} : The number of protons on target which corresponds to the analyzed data in 1KT,
ϵ^{FCFV}_{SK} : The detection efficiency of beam neutrinos in SK,
C_{ν_e} : The correction factor for the difference of ν_e contamination in the beam at near detectors and SK.

The correction factor $C_{\nu e}$ is estimated to be 0.996 with the beam MC simulation. The measured neutrino energy spectrum at near detectors and the far/near flux ratio are incorporated into R_{int}. In $\nu_\mu \rightarrow \nu_e$ search, we use the SK events where the vertex is inside the fiducial volume and all the particles from the interaction are fully contained in the inner detector. The selection criteria and detection efficiency ϵ^{FCFV}_{SK} are described later (Section 6.1). In total, we estimate the total number of neutrino events at SK without oscillation to be $158.4^{+9.4}_{-8.7}$ for the entire period of K2K. For each experimental phase, we estimate the number of neutrino events to be 81.1 and 77.4 for K2K-I and K2K-II, respectively.

Chapter 6

Selection of beam neutrinos in SK

In this Chapter, we describe the selection criteria of beam neutrinos in SK. Then we describe the selection criteria for ν_e signal candidates.

6.1 Selection of beam neutrino events in SK

In this section, we describe the selection criteria for the events originated from the K2K beam neutrinos.

6.1.1 Selection of neutrino events in SK

In SK, the beam neutrino events are stored in a large amount of recorded data. The expected event rate of beam neutrinos is less than one event per day, while approximately 10^6 other triggered events are recorded per day. Most of the recorded events are originated from the background events listed below:

- cosmic-ray muons coming from outside of the detector,
- decay-electrons emitted from stopping muons in the inner detector,
- low energy gamma-rays ($\lesssim 11$ MeV) from radio activity (radon) in the water or surrounding rock,
- flashing light by a discharge of electricity at PMT dynodes,
- solar neutrinos,

- atmospheric neutrinos.

The background events except for atmospheric neutrinos are rejected by the data reduction described below. This is the pre-selection of neutrino events to reduce the amount of data to be processed, and the sophisticated selection cuts are applied after the event reconstruction (Section 6.1.2). Considering the difference of ID PMT density between SK-I and SK-II, some of the selection criteria are defined separately for K2K-I and K2K-II.

High energy trigger event

In SK, beam neutrino events are selected with the high energy trigger. The trigger threshold is set to be 31 (16) hit PMTs within 200 nsec time window, which corresponds to 50–100 (20–50) photoelectrons for SK-I (SK-II).

Decay-electron cut

When a cosmic-ray muon stops inside the tank, the subsequent decay-electron could be misidentified as a neutrino event. To reject the decay-electron background, we require more than 30 μsec between the event and the preceding one.

Total photoelectron cut

To reject low energy background events such as gamma-rays from radon or surrounding rock, we require that the events should have more than 200 (94) photoelectrons in 300 nsec time window for SK-I (SK-II). This threshold corresponds to about 20 MeV/c for electrons and about 190 MeV/c for muons.

Flashing PMT cut

There are sometimes PMTs that flash due to the discharge at dynodes (flashing PMT events). Since the flashing PMT event is often recognized as a neutrino event, we require the following criteria to remove it.

1. **Maximum photo-electron cut** :
   Since the signal from a flashing PMT is localized, we reject the event with $PE_{max}/PE_{300} > 0.2$ (0.4) for SK-I (SK-II), where PE_{max} is the maximum number of photo-electrons among the PMTs and PE_{300} is the number of total photo-electrons in 300 nsec time window.

2. Timing distribution cut :
Most of the flashing PMT events make relatively broad hit-timing distributions. We search for the minimum number of hits within 100 nsec (N_{min}) by sliding time window in the time range 300–800 nsec after the trigger timing. We reject the events with $N_{min} \geq 15$ (20) for SK-I (SK-II). If the number of ID hits is less than 800, we tighten the cut to reject the events with $N_{min} \geq 10$.

3. Goodness of fit :
If the number of ID hits is less than 500 (250) for SK-I (SK-II), we use the goodness of the vertex fitter to reject the flashing-PMT events. The goodness of fit becomes worse for flashing PMT events because the vertex of Cherenkov ring is not reconstructed properly. We select the events with the goodness of fit more than or equal to 0.4.

6.1.2 Reconstruction of neutrino event

Then, we reconstruct neutrino events and apply more strict selection criteria.

The reconstruction algorithm was originally developed for study of atmospheric neutrinos. Each reconstruction step is summarized below. More details are described in Reference [69].

Vertex finding

The vertex position of an event is reconstructed using the timing information of the PMTs. The vertex finding algorithm calculate the residual time defined as $t_0 - t_{TOF}$, where t_0 and t_{TOF} are the hit time of a PMT and the time of flight of Cherenkov light from a given vertex to the PMT, respectively. Scanning vertex points, the algorithm finds the point where the residual times of all the PMTs are in the best agreement. In this step, we also reconstruct the momentum vector and the Cherenkov opening angle of the most energetic ring in the event.

Ring counting

After the vertex reconstruction, the number of rings and their directions are reconstructed. A description of the ring counting algorithm is given in Section 6.2.

Particle identification

The reconstructed rings are classified into two particle types of muon-like [minimum-ionization particle type (MIP-type)] and electron-like (shower-type), by using the ring pattern and the Cherenkov opening angle. A description of particle identification is given in Section 6.2.2.

Precise vertex finding

With the particle identification information, another vertex finding algorithm (MS-fit) is applied for single-ring events to improve the precision of the vertex position. The momentum is also estimated from the total number of photoelectrons within a 70° half-angle cone relative to the particle direction.

6.1.3 Selection of fully-contained events in the fiducial volume of SK

As the second step of the data reduction, we select the events where the vertex is inside 22.5 kt fiducial volume of SK and all the particles are fully contained in the inner detector; these are called Fully-Contained Fiducial-Volume (FCFV) events. For the FCFV events, we properly reconstruct the Cherenkov ring and measure the energy of the particles. The selection criteria are similar to those for atmospheric neutrinos as in Reference [16].

Outer detector cut

We select fully-contained (FC) events using outer detector (OD) information. We require that the FC events should have the maximum number of hits in the OD cluster less than 10. In addition, we also reject the event with the number of OD hits greater than 50 within 800 nsec time window. The remaining cosmic-ray events are also rejected with this cut.

Visible energy cut

Since the energy threshold is not well-defined in the total photoelectron cut, we use the visible energy (E_{vis}). The visible energy is estimated from the sum of all

ring energies in the inner detector, assuming all rings are originated by electrons. We remove the events with E_{vis} lower than 30 MeV.

Visual scan

The remaining events are visually scanned to confirm that the events are really neutrino events. A few flashing-PMT events surviving with the above cuts are removed by this visual scan.

Fiducial volume cut

We require that the reconstructed vertex is within the fiducial volume defined as $D_{\mathrm{wall}} \geq 2.0$ m, where D_{wall} is the distance from the vertex to the nearest surface of ID. This volume corresponds to the water mass of 22.5 kton. Figure 6.1 shows the reconstructed vertex distribution after the beam timing cut described in Section 6.1.4. We find that the reconstructed vertices are distributed uniformly as a characteristics of neutrino events. The boundary of the fiducial volume is shown in the figure.

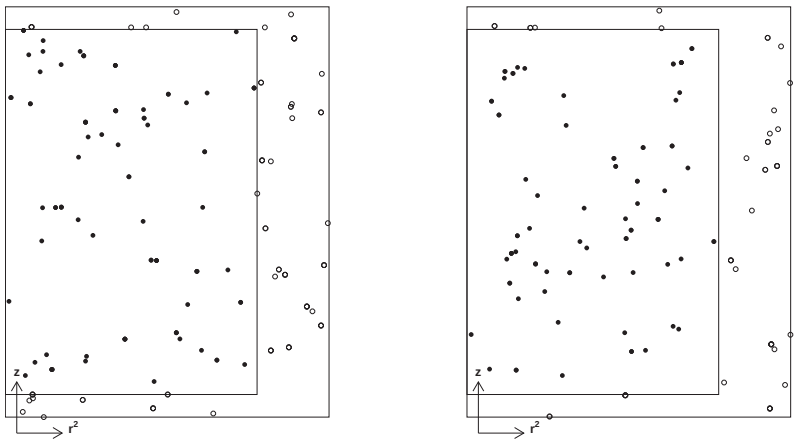

Figure 6.1: Vertex distribution of beam neutrino events in $r^2 - z$ space for K2K-I (left) and K2K-II (right), where r and z are the cylindrical coordinates whose origin is defined as the center on the bottom of the inner detector. The vertices of events inside and outside the fiducial volume are shown by filled and open circles, respectively. The fiducial volume is shown by the inner lines.

6.1.4 Beam neutrino selection with GPS information

Finally, to select beam neutrino events and reject atmospheric neutrinos, we apply a cut based on timing synchronization between the KEK accelerator and SK using the GPS information. We also require the data accumulated under the good beam spill conditions.

Using the UTC stamps of the starting time of the beam spills (T_{KEK}) and the event time in SK (T_{SK}), we define the time difference between the observed event and the expected arrival time of the K2K neutrino beam (ΔT) as

$$\Delta T \equiv T_{\mathrm{SK}} - T_{\mathrm{KEK}} - TOF, \tag{6.1}$$

where TOF is the time-of-flight of neutrinos traveling from KEK to SK, which is approximately 833 μsec with the assumption that the velocity of neutrino is same as the light velocity. For the beam originated events, we expect they distribute within the time range $0 \lesssim \Delta T \lesssim 1.1$ μsec, corresponding to the beam spill width. Considering the uncertainty of the UTC time stamp of < 0.2 μsec, we impose the timing cut as

$$-0.2\ \mu\mathrm{sec} < \Delta T < 1.3\ \mu\mathrm{sec}.$$

Figure 6.2 shows the ΔT distributions for each reduction step within the time windows of $|\Delta T| < 500$ μsec and $|\Delta T| < 5$ μsec. The selected events are clustered within the time window of the beam spill, and they show the bunch structure of beam spill as shown in Figure 6.3. These indicate that we have properly selected the beam neutrino events. Three events outside of the time window are consistent with atmospheric neutrino events; we expect 2.3 background events originated from atmospheric neutrinos in $|\Delta T| < 500$ μsec window.

6.1.5 Observed FCFV events

After the reduction described above, we obtain fifty five and fifty seven FCFV events for K2K-I and K2K-II, respectively. The data reduction of the FCFV selection is summarized in Table 6.1. The selection efficiency for FCFV events in SK is estimated to be 0.772 and 0.779 for K2K-I and K2K-II, respectively, according to the MC simulation. As described in Equation 5.5, we expect the number of FCFV events without oscillation to be 81.1 and 77.4 for K2K-I and K2K-II, respectively.

The relation between the observed number of events and the accumulated number of POT is shown in Figure 6.4. The observed number is proportional to

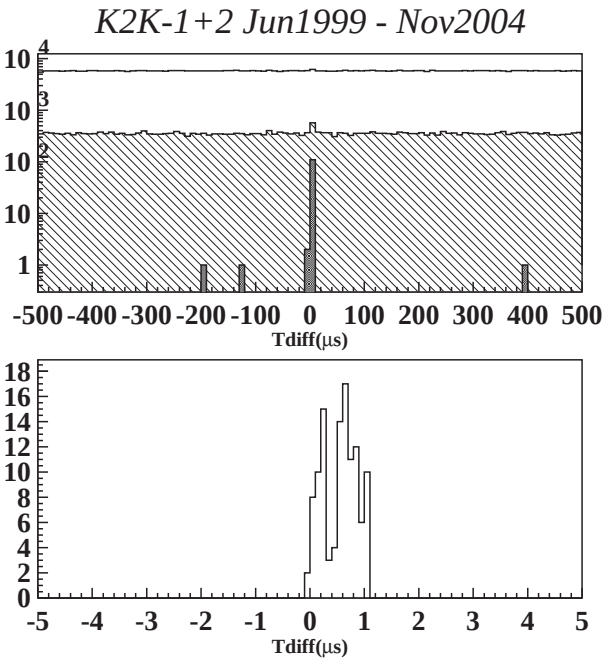

Figure 6.2: ΔT distribution for each reduction step. Open, hatched and shaded histograms in the upper figure are after the decay electron cut, the visible energy cut and the fiducial volume cut, respectively. The lower is the ΔT distribution after the timing cut. Data of K2K-I and K2K-II are combined.

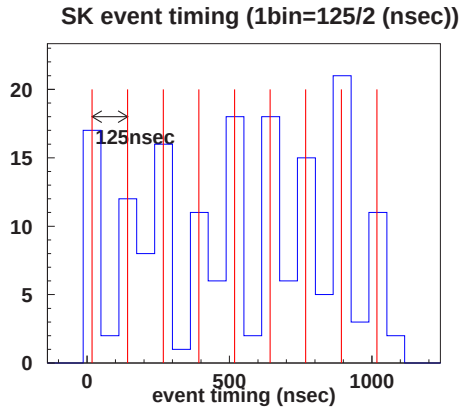

Figure 6.3: ΔT distribution in a narrow time window.

Table 6.1: Reduction of fully contained events in the fiducial volume.

	K2K-I	K2K-II
Total number of spill	9177578	8214003
$\|\Delta T\| < 500\mu$s	107892	470469
High energy trigger	36560	29878
Total p.e. cut	18902	16623
$E_{vis} > 30$eV	103	88
Scanning	95	87
Fiducial volume cut	56	59
$-0.3\mu\text{s} < \Delta T < 1.2\mu\text{s}$	55	57

the accumulated POT as we expect. The KS-test probability assuming the linear correlation is 79%.

6.2 Selection of electron signal candidates in the fully-contained events

We have one hundred and twelve fully-contained events in the 22.5kt fiducial volume of SK. We select the the ν_e appearance signal candidate events from the FCFV events with the following requirements:

(i) single-ring event,

(ii) shower-type ring,

(iii) visible energy above 100 MeV (rejection of low energy pions),

(iv) no decay electron follows the event (rejection of muons),

(v) non-π^0 like event.

The selection criteria of each step are described in the following sections. The selection (i)-(iv) use the standard reconstruction algorithm of atmospheric neutrinos. For the final selection (v), we developed a new reconstruction algorithm, described in Chapter 7. The data reduction is also summarized after applying this π^0 rejection cut.

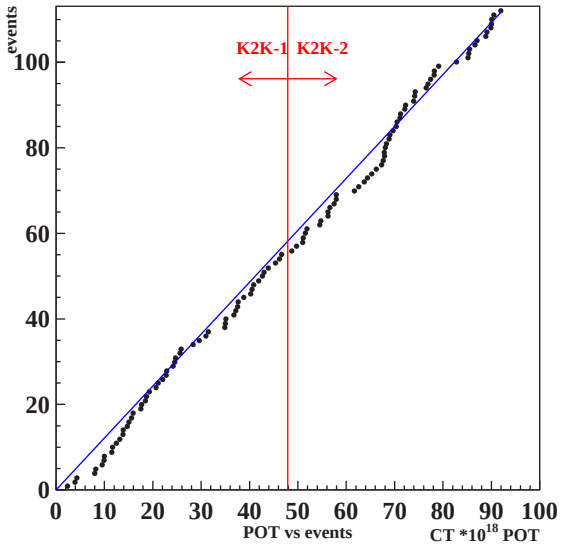

Figure 6.4: Neutrino event rate at SK as a function of POT.

6.2.1 Single-ring event selection

We count the number of Cherenkov rings of the FCFV events, and select single-ring events to enhance the fraction of ν_e CC-QE events. Single-ring events are separated from multi-ring events based on an estimator using the charge pattern distribution on the PMTs. A second ring is searched for by scanning possible ring directions, and the assumption of two rings is compared with that of one ring. To obtain the number of rings which is most consistent with the data, the ring counting algorithm works iteratively and tries to find another ring. The estimator is constructed to take a positive value when the second ring is detected: negative values indicate a single-ring event. We require the candidate events to have negative values of the estimator. Distributions of the ring counting estimator for K2K-I and K2K-II data, together with those of the MC simulation for the ν_e signal events and ν_μ background events are shown in Figure 6.5. Unless we explicitly state otherwise, the histograms of the MC events are normalized by the number of expected ν_μ events (81.1 for K2K-I and 77.4 for K2K-II) at SK without oscillation in this chapter.

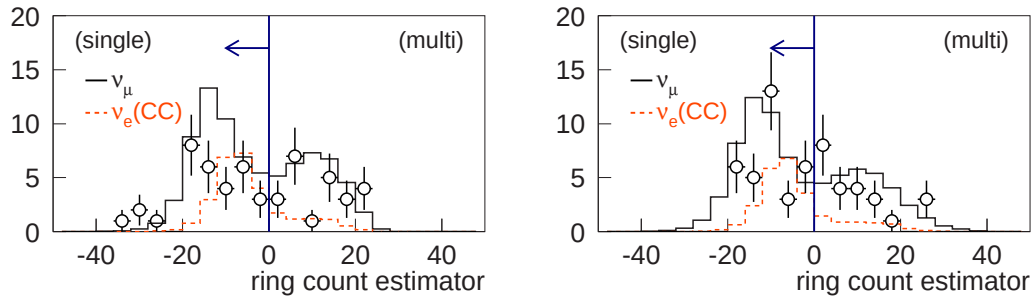

Figure 6.5: Distributions of the ring counting estimator for K2K-I (left) and K2K-II (right). The open circles show the data. The solid histogram and the dashed one show the ν_μ background MC events and the ν_e signal MC events on the assumption of $\sin^2 2\theta_{\mu e}$ =1.0 and $\Delta m^2 = 2.8 \times 10^{-3}$, respectively. Negative values indicate the single-ring events.

6.2.2 Shower-type ring selection

Next, we identify the particle type of a Cherenkov ring.

An electron or a gamma-ray make a ring with a diffused hit pattern due to the electromagnetic shower and the multiple scattering. On the other hand, a muon or a charged pion make a ring with the sharp edge and they can be distinguished from an electron or a gamma-ray. In addition, for a given momentum, the difference in mass makes Cherenkov opening angle different for an electron and a muon. Thus, we construct the estimators based on the ring pattern and the opening angle.

To identify the particle type, the observed charge pattern is compared with the expectation of an electron or that of a muon based on the MC simulation. The probability function of the charge for each PMT is assumed to be the Gaussian distribution (or Poisson distribution for small photoelectrons) using the number of observed photoelectrons and the expected one assuming an electron or a muon [69]. The ring pattern likelihood for the electron (muon) ring ($\mathcal{L}$) is constructed with the product of the probabilities for the PMTs inside the 70° half-angle cone relative to the particle direction. Then, the probability from the ring pattern for electrons (muons) is given as

$$Prob_{\text{pattern}}\left(e(\mu)\right) = \exp\left[-\frac{\{\chi^2\left(e(\mu)\right) - min(\chi^2(e), \chi^2(\mu))\}}{2\sigma^2_{\chi^2}}\right], \tag{6.2}$$

where $\chi^2(e(\mu))$ is translated from the ring pattern likelihood as $\chi^2(e(\mu)) = -2\log\mathcal{L}$. The resolution of the χ^2 distribution, σ_{χ^2}, is approximated by $\sigma_{\chi^2} = \sqrt{N}$, where N is the number of PMTs used in the calculation.

For the Cherenkov opening angle, the probability is similarly given as

$$Prob_{\text{angle}}\left(e(\mu)\right) = \exp\left[-\frac{\left\{\theta^{obs} - \theta^{exp}\left(e(\mu)\right)\right\}^2}{2\left(\delta\theta\right)^2}\right], \tag{6.3}$$

Where θ^{obs} ,$\delta\theta$ and $\theta^{exp}(e(\mu))$ are the reconstructed opening angle, the uncertainty of the reconstruction and the expected opening angle with the reconstructed momentum assuming an electron (a muon), respectively.

With these variables, two PID parameters of ring pattern (P_{pattern}) and opening angle (P_{angle}) are defined as:

$$P_{\text{pattern(angle)}} = \sqrt{-logP_{\text{pattern(angle)}}(\mu)} - \sqrt{-logP_{\text{pattern(angle)}}(e)}. \tag{6.4}$$

The distribution of single ring events in $P_{\text{pattern}} - P_{\text{angle}}$ space is shown in Figure 6.6. We select the events where both PID parameters are negative as the shower-type events.

6.2.3 Visible energy cut

Some of ν_μ-originated background events are caused by low-energy charged pions or muons. When a charged pion interacts in the water and it makes the Cherenkov ring edge scattered, the event can be classified as single-ring shower-type by the reconstruction algorithm. In addition, for a muon with the momentum below Cherenkov threshold, only an electron event from its decay is observed with the energy of a few tens of MeV. These events have E_{vis} below $\sim$ 100 MeV. Thus, we reject the events to have the visible energy below 100 MeV as the background. The distributions of the visible energy are shown in Figure 6.7.

6.2.4 No decay electron

After the selection cuts described above, a small fraction of muon or mis-identified charged pion events still remains. To reject these events, we require that the signal candidate events are not followed by an event of muon-decays within a

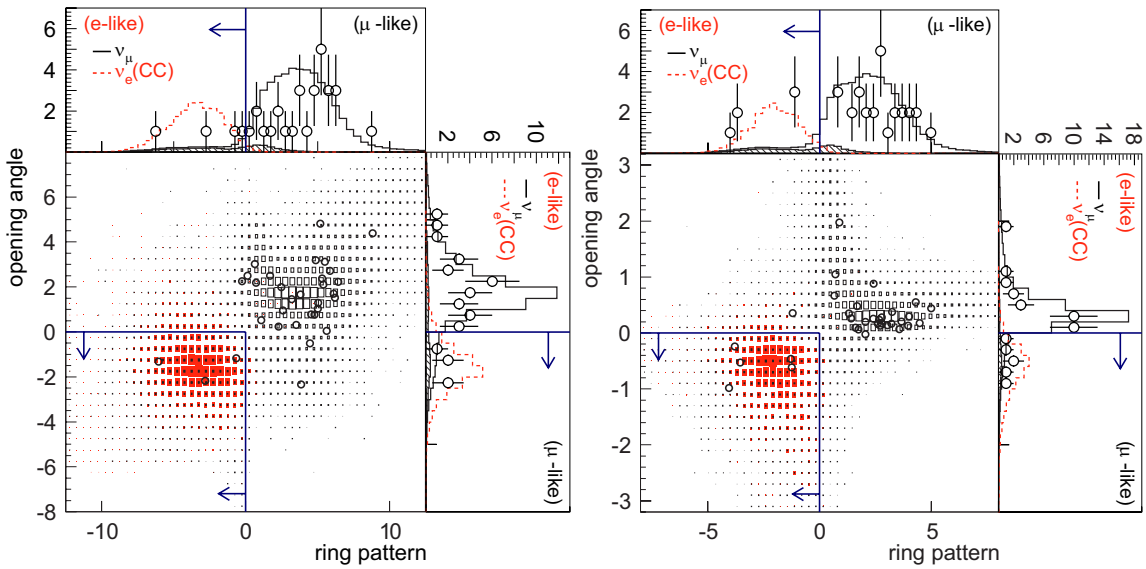

(a) K2K-I

(b) K2K-II

Figure 6.6: Distribution of single-ring events in the ring pattern and opening angle parameter space for K2K-I and K2K-II. The open circles show the data. The open boxes and the solid ones show the ν_μ background MC events and the ν_e signal MC events on the assumption of $\sin^2 2\theta_{\mu e}$ =1.0 and $\Delta m^2 = 2.8 \times 10^{-3}$, respectively. The selection boundary for shower-type events are shown with lines. The events with negative values of each PID parameters are classified as the shower like event. The projections of each PID parameter are also shown, and the hatched region in them represents the composition of ν_μ-NC interaction.

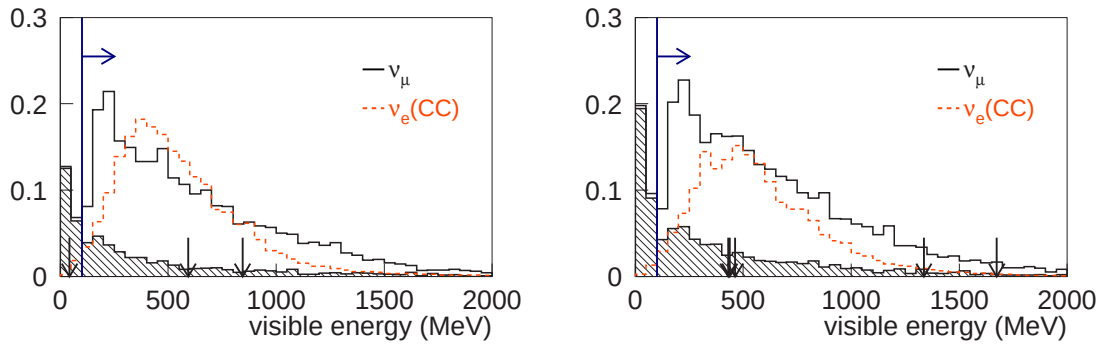

(a) K2K-I

(b) K2K-II

Figure 6.7: Visible energy distribution of single-ring shower-type events. The remaining events in the data are shown by arrows. The distribution of ν_μ background MC events are shown by a solid histogram. The contribution of low-energy charged pion and muon in the ν_μ-originated background is shown by the hatched region. The ν_e signal MC events, on the assumption of $\sin^2 2\theta_{\mu e}$ =0.1 and $\Delta m^2 = 2.8 \times 10^{-3}$, is also shown by a dashed histogram. The selection boundary is drawn with a line.

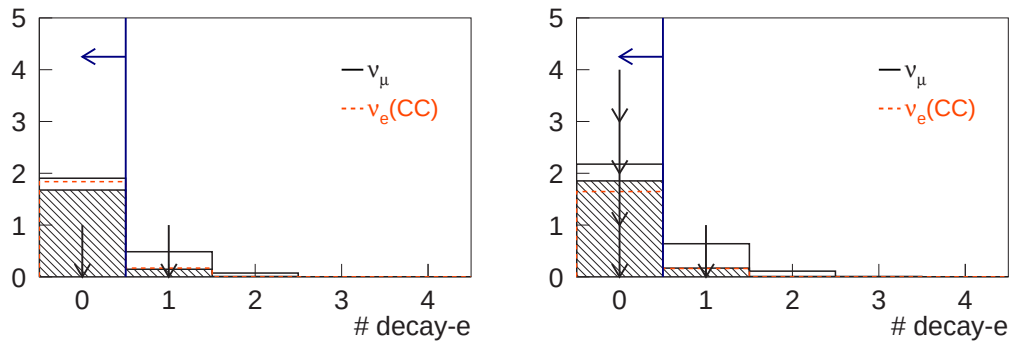

(a) K2K-I (b) K2K-II

Figure 6.8: Distribution of the number of decay electrons for single-ring shower-type events. The remaining events in the data are shown by arrows. The distribution of ν_μ background MC events and the ν_μ-NC composition are shown by a solid and hatched histograms, respectively. The dashed histogram shows the ν_e signal MC on the assumption of $\sin^2 2\theta_{\mu e}$ =0.1 and $\Delta m^2 = 2.8 \times 10^{-3}$.

30 μsec time window. Distributions of the number of decay-electrons are shown in Figure 6.8. The criteria of decay electron tagging is described in Appendix D.

With all the standard selection cuts described above, we obtain one signal candidate for K2K-I and four for K2K-II. On the other hand, we expect that the number of ν_μ-originated background events to be 4.1 for the entire data sample. As shown in Figure 6.8, the ν_μ-originated background is dominated by the NC interaction events in which most of them make up π^0's, according to the MC simulation.

6.3 Summary

In this chapter, we described the selection criteria for the beam neutrinos and the event reconstruction. We obtained one hundred and twelve fully-contained events in the 22.5 kt fiducial volume of SK.

For the FCFV events, we applied the standard selection cuts to select the signal-ring shower-type events. We obtained one candidate event in K2K-I and four in

K2K-II. However, we expect that the π^0 background events are yet to be rejected according to the MC simulation. For the final π^0 rejection cut, we give detailed descriptions in the next chapter. We also give the resultant number of surviving events after the π^0 rejection.

Chapter 7

Rejection of neutral pion background

In the search for a signal of $\nu_\mu \rightarrow \nu_e$ oscillation, a dominant source of background events is originated from π^0 production in neutrino-^{16}O interactions. In this chapter, we introduce a new reconstruction algorithm called "π^0 fitter" to improve the π^0 rejection. At first, we present the characteristics of π^0 background events. We then describe the π^0 reconstruction algorithm. Second, we check the performance of the π^0 fitter by using atmospheric neutrinos. In the end, we apply the π^0 fitter to the surviving events for the final selection of signal candidate events in K2K.

7.1 Characteristics of π^0 background event

A dominant source of background comes from the events with a single π^0 decaying into two gamma-rays, where one gamma-ray is missed by the standard reconstruction algorithm described in Section 6.2. The π^0 events are classified as single-ring shower-type, the same signature of ν_e-CC interaction. The π^0 background mainly originates from NC interaction where a single π^0 and no other mesons are produced in the final state from the nucleus. We label this π^0 background as "NC1π^0 ". In the K2K beam energy, a single π^0 is produced via Δ resonance of NC interaction as

$$\begin{aligned} \nu + N &\rightarrow \nu + \Delta \\ &\hookrightarrow N' + \pi^0, \end{aligned}$$

where N and N' are nucleons. In addition, π^0's could be produced by final state interactions of nucleons or mesons inside of nucleus. We estimate that 70% of

background in the single-ring shower-type sample originate from NC1π^0 process after the standard selection described in Section 6.2. From now on, unless we explicitly state otherwise, we define that the higher-energy gamma-ray is the "first" gamma-ray and the lower-energy one is the "second" in π^0 decay.

A gamma-ray from π^0 decay could be missed with the following reasons.

- The energies of two gamma-rays are highly asymmetric and the energy of second gamma-ray ($E_{\gamma 2}$) is too small to be reconstructed as a ring (Figure 7.1a).

- The two rings of gamma-rays are overlapped and reconstructed as one ring when the opening angle between two gamma-rays ($\theta_{\gamma\gamma}$) is small (Figure 7.1b).

The $E_{\gamma 2}$-$\theta_{\gamma\gamma}$ and π^0 momentum distributions of NC1π^0 background events in the single-ring shower-type sample are shown in Figure 7.2. Since the events cluster in the $E_{\gamma 2}$ region below $\sim$ 50 MeV, we find the second gamma-ray with lower energy is not properly reconstructed as a ring, as shown in Figure 7.1(a). We also find the events cluster in the region $\theta_{\gamma\gamma} < 20°$. To count the Cherenkov rings, we search ring edges in the observed charge pattern. Therefore, due to the finite image resolution, we cannot count over two rings for π^0 events with $\theta_{\gamma\gamma} <\sim 20°$ as shown in Figure 7.1(b).

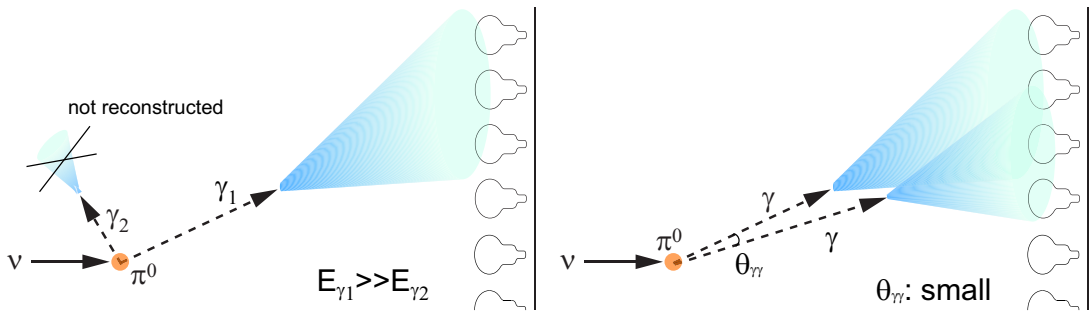

(a) Highly asymmetric energy decay (b) Small opening angle

Figure 7.1: Illustrations of π^0 production background.

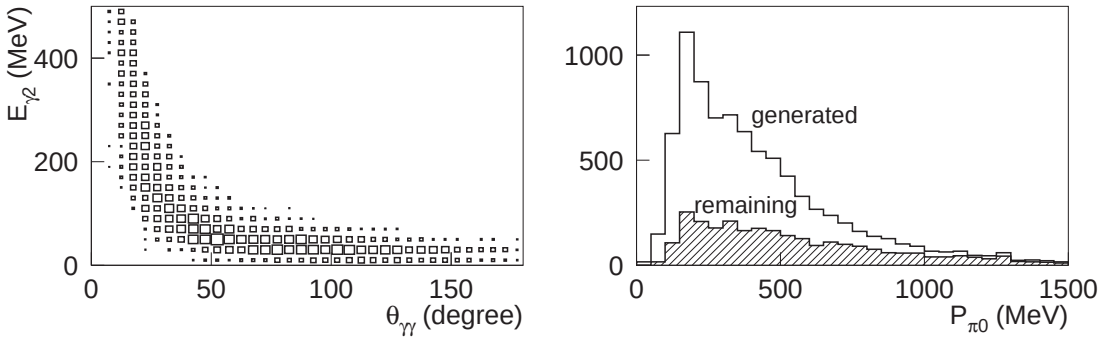

Figure 7.2: $E_{\gamma 2} - \theta_{\gamma\gamma}$ (left) and π^0 momentum (right) distributions of NC1π^0 background events in the single-ring shower-type sample. In the right figure, the histogram shows the all events produced via NC1π^0 interaction, and the hatched shows those classified as single-ring shower-type.

7.2 Reconstruction algorithm of the π^0 fitter

We describe the new algorithm of the π^0 fitter developed to improve the π^0 reconstruction.

For the reconstruction of second gamma-ray, the fitter works on the assumption that two Cherenkov rings of gamma-ray must exist. The π^0 fitter reconstructs two gamma-rays by comparing the observed charge distribution on the PMTs with the expected charge distributions of two gamma-rays.

In the fitter, two gamma-rays are supposed to be emitted at one point. Then the following variables given by the standard reconstruction algorithm are used as input:

- vertex,
- direction of the shower-type ring,
- visible energy ($E_{\rm vis}$).

The vertex is assumed to be the point where two gamma-rays were emitted, and the direction of the first gamma-ray is set to be that of the single ring found by the standard reconstruction. Varying the direction of the second gamma-ray and the fractions of energy shared among two gamma-rays, we obtain a combination

of two gamma-rays which matches with the observed charge distribution. The estimation of charge distribution and the fitting method are described next.

7.2.1 Expected charge distribution

The expected charge distribution is calculated for the given vertex, momenta and directions of two gamma-rays. On the assumption that the Cherenkov photon flux is axially symmetric around the direction of gamma-ray, the Cherenkov photon fluxes are estimated as a function of the angle θ with respect to the gamma-ray direction. The shape of electromagnetic shower and its length depend on the initial gamma-ray momentum (p_γ). Further, the Cherenkov photon flux depends on the distance of the PMT from the vertex (r). Thus, the direct light distributions are estimated as a function of θ, p_γ and r in the MC simulation.

In this way, the expected photoelectrons for the i-th PMT from a gamma-ray (q_i^{exp}) is given as

$$q_i^{exp} = \alpha \cdot Q^{exp}(\theta_i, p_\gamma, r_i) \cdot \left(1 - \frac{r_i}{\sqrt{r_i^2 + R_{PMT}^2}}\right) \cdot \exp\left(\frac{-r_i}{L}\right) \cdot f^{acc} + q_i^{scatt} \qquad (7.1)$$

where

α	:	the normalization factor,
Q_i^{exp}	:	the expected photon flux from a gamma-ray, which is estimated as a function of θ_i, p_γ and r_i,
R_{PMT}	:	the PMT radius of 25 cm,
L	:	the attenuation length of water,
r_i	:	the distance from the vertex to the i-th PMT,
f^{acc}	:	the correction of PMT acceptance as a function of incident light angle to the PMT.
q_i^{scatt}	:	the expected scattered light flux on i-th PMT.

The factors of $\left(1 - r_i/\sqrt{r_i^2 + R_{PMT}^2}\right)$ and $\exp(-r_i/L)$ represent the corrections of solid angle and light attenuation, respectively. The effect of the light scattering is also taken into account based on the measurement using a laser as in Reference [55]. Finally, the expected charges are summed for two gamma-rays to obtain an expected charge distribution.

7.2.2 Finding the best-fit ring configuration

To determine the best-fit configuration of two gamma-rays, a χ^2 fit is applied to the charge distribution with the fitting parameters of gamma-ray momentum vectors $p_{\gamma 1}$ and $p_{\gamma 2}$. Supposing that the charge pattern is distributed according to Poisson statistics, the χ^2 for a PMT (χ^2_i) is given by

$$\chi^2_i(p_{\gamma 1}, p_{\gamma 2}) = 2(q_i^{exp}(p_{\gamma 1}, p_{\gamma 2}) - q_i^{obs}) + 2q_i^{obs} \ln \frac{q_i^{obs}}{q_i^{exp}(p_{\gamma 1}, p_{\gamma 2})}, \tag{7.2}$$

where q_i^{exp} is the expected charge on the i-th PMT for the given gamma-rays, and q_i^{obs} is the observed one. The fitting is performed by minimizing the overall χ^2, the sum of χ^2_i among all PMTs, using the simplex method [70,71]. In the procedure, we do not require any kinematical constraint of π^0 decay.

The π^0 events where two rings are almost overlapped have a narrow χ^2 distribution in the direction of the first ring. To improve the fitting performance for such events, a second fit is performed with the finer stepping to look for the second gamma-ray near the first gamma-ray ring. The procedure of the second fit is identical to the initial one except that the initial parameters of second gamma-ray are set to be near the first gamma-ray ring. We choose the fitting result with a smaller χ^2 between two fits.

Figure 7.3 shows the energy resolution of gamma-ray as a function of the gamma-ray energy, estimated from the MC π^0 events. The resolution of the first gamma-ray energy ($E_{\gamma 1}$[GeV]) is estimated to be $\sim$ 20%, while the resolution for the second is estimated to be $3.1/\sqrt{E_{\gamma 2}} + 19.4(\%)$ for K2K-I and $3.5/\sqrt{E_{\gamma 2}} + 18.8(\%)$ for K2K-II. The angular resolution of the gamma-ray direction and the opening angles between two gamma-rays are shown in Figure 7.4. The resolutions are around 8° for the gamma-ray direction and $\sim$ 6.5° for the opening angle. Figure 7.5 shows the distribution of the invariant mass (M_{inv}) reconstructed from two gamma-rays found by the π^0 fitter. The M_{inv} is defined as

$$M_{inv} = \sqrt{2E_{\gamma 1}E_{\gamma 2}(1 - \cos\theta_{\gamma\gamma})}. \tag{7.3}$$

The resolution of π^0 invariant for K2K-I and K2K-II is 22.4 MeV/c^2 and 23.1 MeV/c^2, respectively.

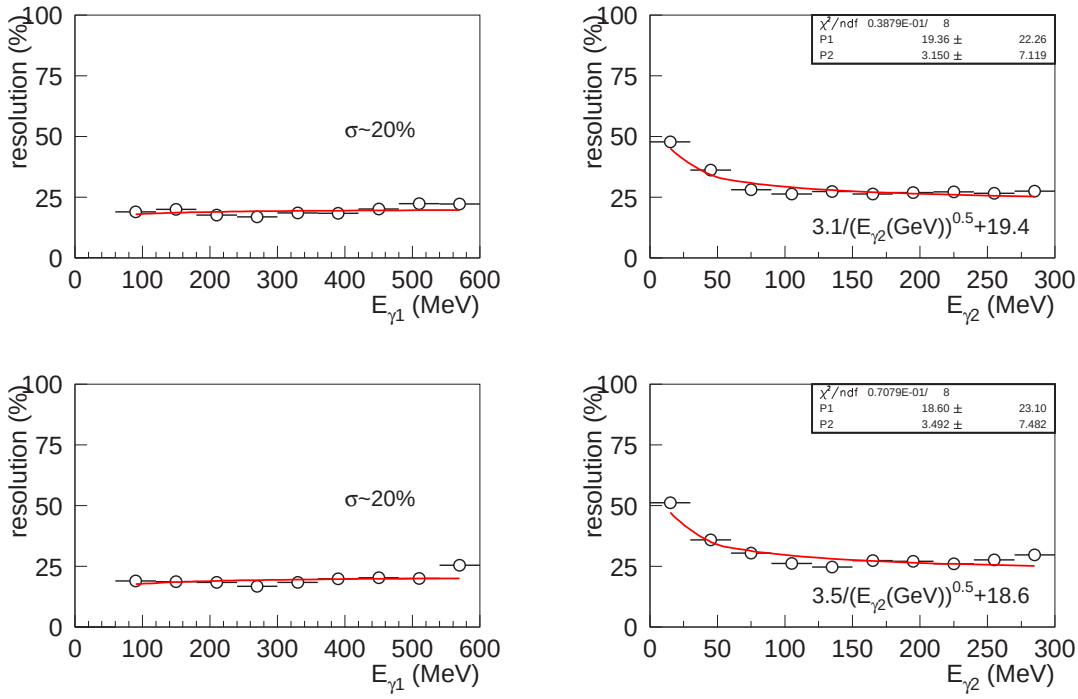

Figure 7.3: Energy resolution of gamma-rays for NC1π^0 events for K2K-I (upper) and K2K-II (lower).

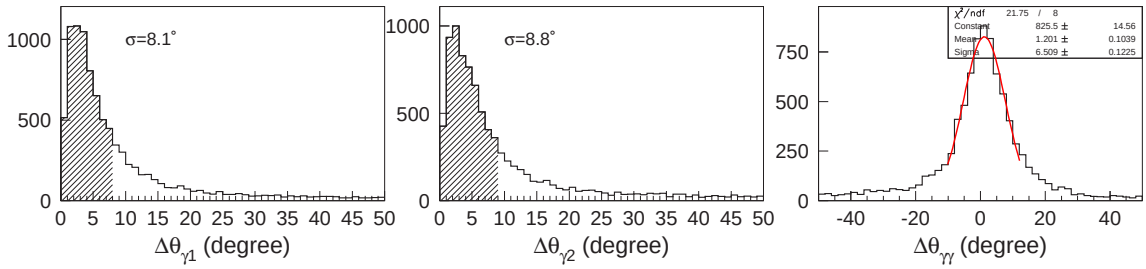

(a) K2K-I

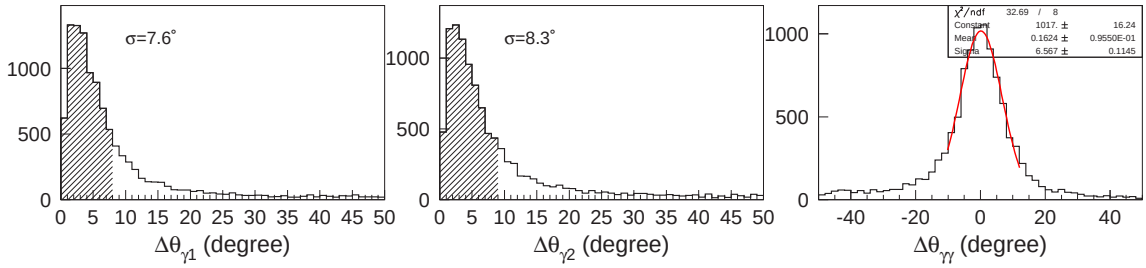

(b) K2K-II

Figure 7.4: Angular resolution of gamma-rays for NC1π^0 events. The angular resolution of gamma-rays is defined as the width in which 68% of the events are included.

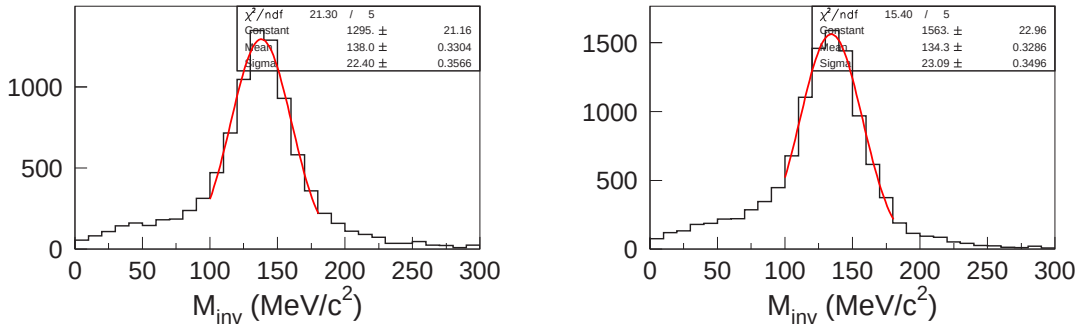

Figure 7.5: Reconstructed π^0 invariant mass distribution of NC1π^0 events for K2K-I (left) and K2K-II (right).

7.3 Performances of π^0 reconstruction

In order to check the performance of the π^0 fitter, we use MC NC1π^0 events in SK with the K2K neutrino energy spectrum. We apply the π^0 fitter for the NC1π^0 events. When the multiple rings are found in the standard reconstruction algorithm, the ring with highest energy is used as the input to the π^0 fitter.

At first, with the standard reconstruction algorithm, we select the single π^0 events with the following selection criteria:

(i) two-ring events,

(ii) both rings are shower-type,

(iii) no decay electron follows,

(iv) 85 MeV/c^2 < M_{inv} < 185 MeV/c^2.

Criterion (iii) is used to reject invisible muons and charged pions whose momentum is below the Cherenkov threshold. The detection efficiency of NC1π^0 event is estimated to be 46% (44%) for K2K-I (K2K-II), for the standard algorithm.

Second, we select the π^0 events by the π^0 fitter to compare the performance with the standard reconstruction algorithm. In this event selection, we only require one ring with shower-type. So we remove the criteria (i) and (ii), and replace them with

(i') single or multi-ring events with one shower-type.

Then, we apply the π^0 fitter to find the two gamma-ray rings. In the calculation of invariant mass in criterion (iv), we use the momenta and the opening angle between two gamma-rays reconstructed by the π^0 fitter. Applying the criteria (i'), (iii) and (iv) with the π^0 fitter, we improve the π^0 detection efficiency of NC1π^0 event to 76% (78%) for K2K-I (K2K-II). The detection efficiencies as a function of π^0 momentum and in $E_{\gamma 2}$-$\theta_{\gamma\gamma}$ space with the MC-true information are shown in Figure 7.6 and 7.7, respectively. With the π^0 fitter, we recover the π^0 events especially with high momentum in which the opening angle of two gamma-rays is small or the energy of the second gamma-ray is low.

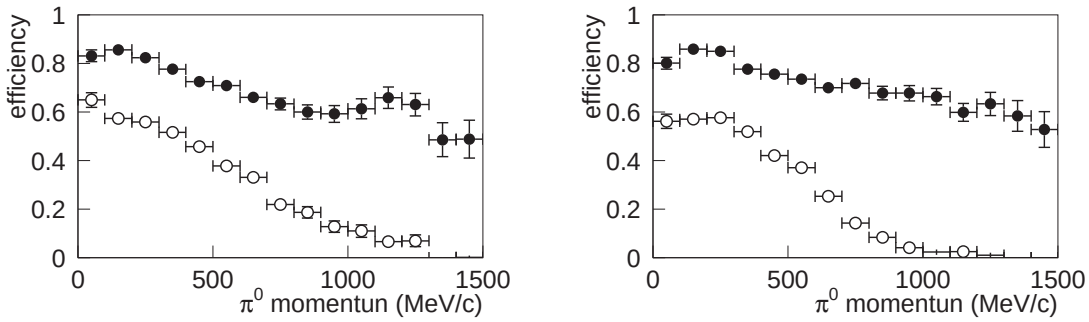

Figure 7.6: π^0 detection efficiency as a function of momentum for K2K-I (left) and K2K-II (right). The open circles show the efficiency with the standard reconstruction by criteria (i)-(iv) and the solid circles show that with the π^0 fitter by criteria (i')+(iii)+(iv).

7.4 e/π^0 separation

In this section, we study the performance of the separation between electrons and π^0's.

For the separation between the electron events and the π^0 events, we use the invariant mass of two gamma-rays reconstructed by the π^0 fitter. We note that the π^0 fitter may find the second gamma-ray ring even for single-electron events. The invariant mass distributions of ν_μ-originated background and ν_e signal events for single-ring shower-type events are shown in Figure 7.8. The π^0 background events have a value of M_{inv} close to the π^0 mass, while a ν_e signal event has M_{inv} smaller than the π^0 mass. This is explained as follows.

For ν_e signal events, there is no real second ring and the fitter could reconstruct the second fake ring with hits around the first energetic ring. Because the electromagnetic shower and light scattering defuse the edge of the first ring and make scattered hits around it, the fitter recognizes these hits as a ring of gamma-ray. Therefore, the angle between the second fake ring and the first ring is expected to be close ($\sim 20^\circ$). Further, the visible energy is equivalent to the shower-type ring energy (E_e) for the single-ring shower-type events and the second gamma-ray energy tends to be small after sharing E_e with the two-ring configuration. Figure 7.9 shows distributions of the reconstructed opening angle and the energy fraction of the first gamma-ray ($E_{\gamma 1}/(E_{\gamma 1}+E_{\gamma 2})$). Considering that E_e is shared with two rings

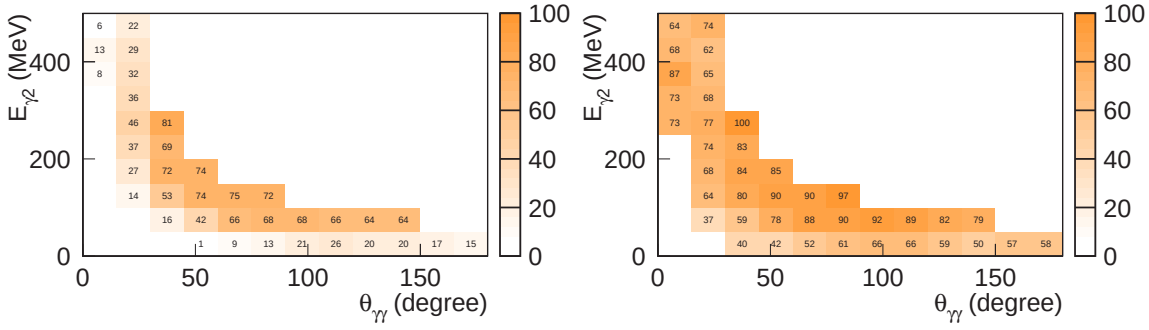

(a) K2K-I

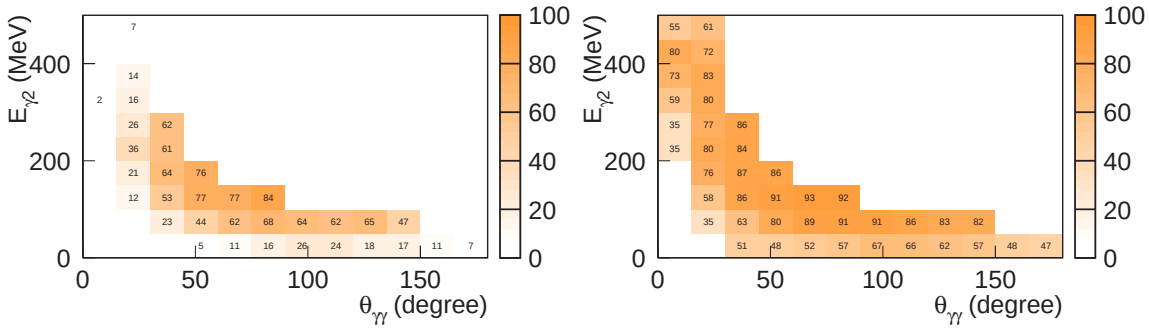

(b) K2K-II

Figure 7.7: π^0 reconstruction efficiency in $E_{\gamma 2}$-$\theta_{\gamma\gamma}$ space. The left figures show the efficiency with the standard reconstruction and the right ones show that with the π^0 reconstruction.

and the reconstructed opening angle and the energy fraction are assumed to be constant ($\sim 20^\circ$ and ~ 0.9), we expect a linear dependence of M_{inv} on the electron energy as $M_{inv} = \sqrt{2(0.9E_e)(0.1E_e))(1-\cos 20^\circ)} \propto E_e$, as shown in Figure 7.10.

As a result, for the ν_e signal event in the energy region of K2K neutrino beam, M_{inv} is reconstructed to be smaller than the nominal π^0 mass. Then, by selecting the low M_{inv} events, we can separate the electron events from the π^0 events.

We also find that the peak position of M_{inv} for the π^0 background events is slightly shifted lower from the nominal π^0 mass as shown in Figure 7.8. We reconstruct M_{inv} less than the π^0 mass when $E_{\rm vis}$ (or E_e) is smaller than the true π^0 energy (E^0_π). Because the standard reconstruction algorithm defines the observed charge within a 70° half opening angle of Cherenkov ring toward the particle direction as E_e, the energy of the second gamma-ray is not included in E_e for the events where the opening angle of two gamma-rays is large. Figure 7.11 shows the difference between E_e and E_{π^0} for the π^0 background events with $\theta_{\gamma\gamma} < 40^\circ$ and $\theta_{\gamma\gamma} > 70^\circ$. Although E_e is equivalent to E_{π^0} for the events with $\theta_{\gamma\gamma} < 40^\circ$, E_e is slightly lower than E_{π^0} for the events with a large $\theta_{\gamma\gamma}$. Consequently, we observe M_{inv} lower than the π^0 mass when E_e is smaller than E_{π^0} and it is shared with two gamma-rays in the π^0 fitter.

7.5 Validation of π^0 fitter with atmospheric neutrinos

We apply the π^0 fitter for the real data of atmospheric neutrinos to validate the performance.

Using the standard reconstruction algorithm, we select the events with two shower-type rings (two-ring shower-type events) by requiring the criteria (i)-(iv) given in Section 7.3. Figure 7.12 shows the invariant mass distribution of two-ring shower-type events for atmospheric neutrinos. The MC histograms are normalized by the live time of 1492 days for SK-I and 627 days for SK-II. We then apply the π^0 fitter to these samples. The comparison of reconstructed gamma-ray energies and opening angle between the standard reconstruction and the π^0 fitter is shown in Figure 7.13. We find a good agreement between the standard reconstruction algorithm and the π^0 fitter for the two-ring π^0 events, and also find a good agreement between data and the MC events.

We also perform a check for e/π^0 separation by using the single-ring events of atmospheric neutrinos. (These atmospheric neutrino events have the same

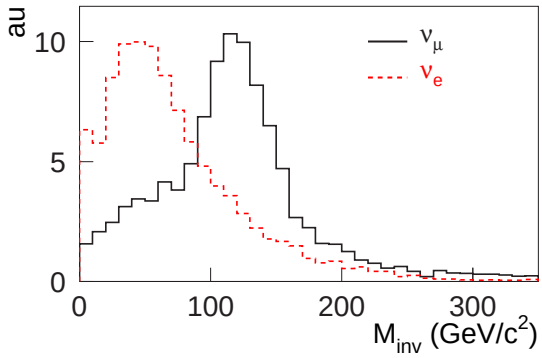

Figure 7.8: Invariant mass distribution of $\pi^0 \to \gamma\gamma$ for single-ring shower-type events. The solid line shows the ν_μ background MC events, and the dashed line shows the ν_e signal MC events assuming $\Delta m^2 = 2.8 \times 10^{-3}$ eV^2.

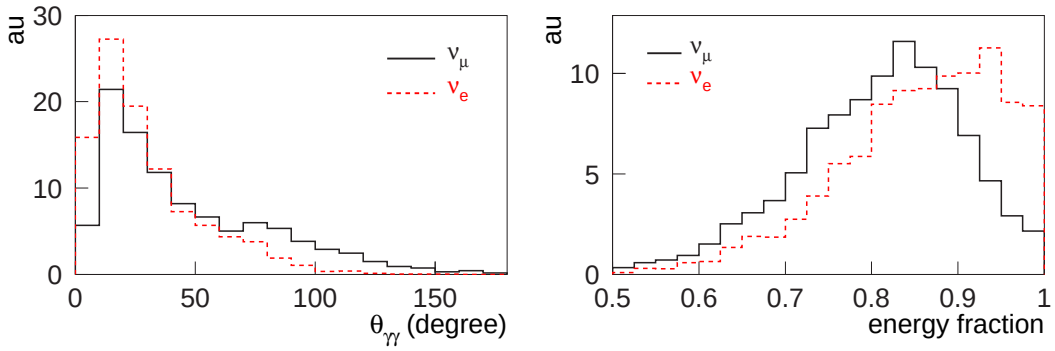

Figure 7.9: Opening angle (left) and energy fraction (right) distributions given by the π^0 fitter for single-ring shower-type events. The solid line shows the ν_μ background MC events, and the dashed line shows the ν_e signal MC events assuming $\Delta m^2 = 2.8 \times 10^{-3}$ eV^2.

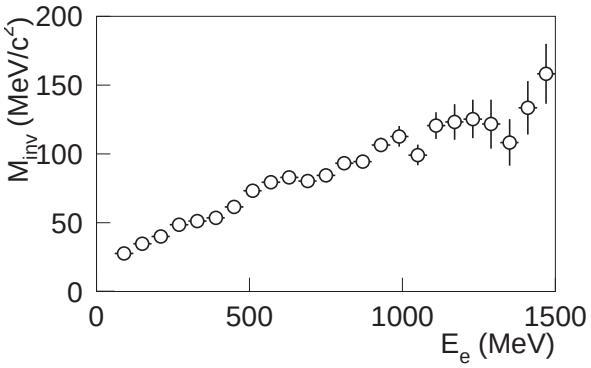

Figure 7.10: Profile histogram of M_{inv}-E_e for ν_e signal events under the assumption of $\Delta m^2 = 2.8 \times 10^{-3}$ eV^2.

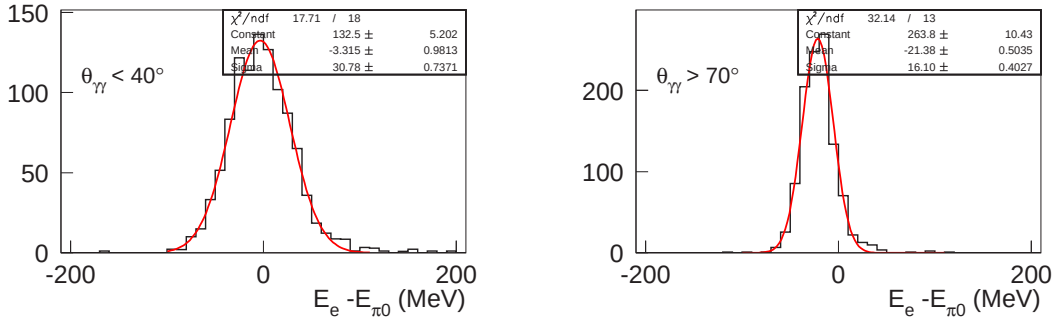

Figure 7.11: The difference between the shower-type ring energy and the π^0 energy for the π^0 background events with $\theta_{\gamma\gamma} < 40°$ (left) and $\theta_{\gamma\gamma} > 70°$ (right).

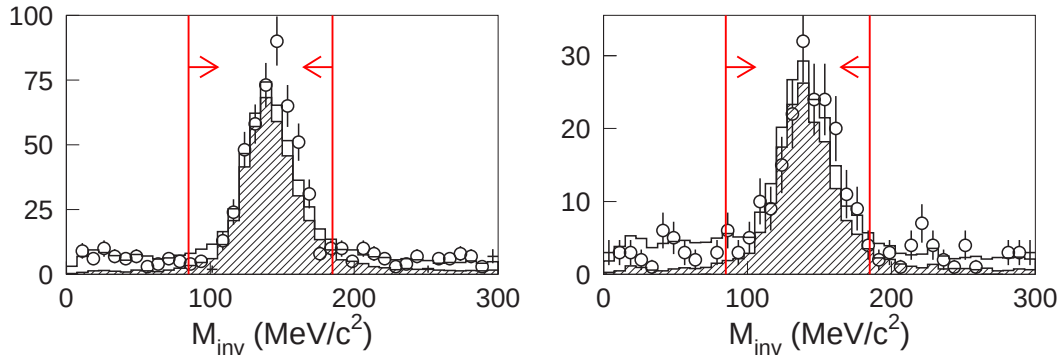

Figure 7.12: The invariant mass distributions for the atmospheric neutrino events with two shower-type rings for SK-I (left) and SK-II (right). The open circles and histogram show the data and the MC events, respectively. The hatched histogram shows the contribution from NC interactions. The selection boundary is shown by lines. The MC histograms are normalized by the live time of the detector.

topology as ν_e signal or ν_μ-originated background in K2K.) In this sample, more than 90% of events are originated from ν_e ($\bar{\nu}_e$) interaction, and the remaining fraction comes from ν_μ ($\bar{\nu}_\mu$). The π^0's are produced via NC interaction of ν_e ($\bar{\nu}_e$) and ν_μ ($\bar{\nu}_\mu$), and have a $\sim$ 6% fraction of the events. Figure 7.14 shows the distribution of atmospheric neutrinos in M_{inv}-E_e space. The MC event distributions for CC and NC interactions are separately shown in the top and middle plots, respectively. We can see the π^0 events clustered around the π^0 invariant mass for NC interaction. In the distribution of the data, we can recognize the events around the π^0 mass expected by the NC interaction of the MC simulation. Figure 7.15 shows the invariant mass distribution of single-ring shower-type events with the shower-type ring energy below 250 MeV. The invariant mass distribution of electrons and π^0's shows reasonable agreement between the data and the MC simulation. In addition, the invariant mass peak of π^0 is obtained by fitting with a combination of the Gaussian function for the π^0 events and the exponential function for the electron events (Figure 7.16). The fitted peaks of data and the MC events for SK-I (SK-II) are 122(118) MeV/c^2 and 116(117) MeV/c^2, respectively. The data are consistent with the MC simulation considering the energy scale uncertainty of 2% [60] and the statistical uncertainty of data; the estimated statistical errors are $\pm$2MeV/c^2 and $\pm$3 MeV/c^2 for SK-I and SK-II, respectively.

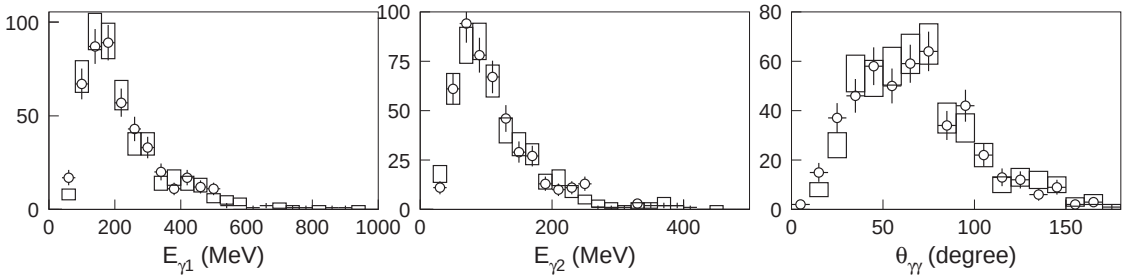

(a) SK-I

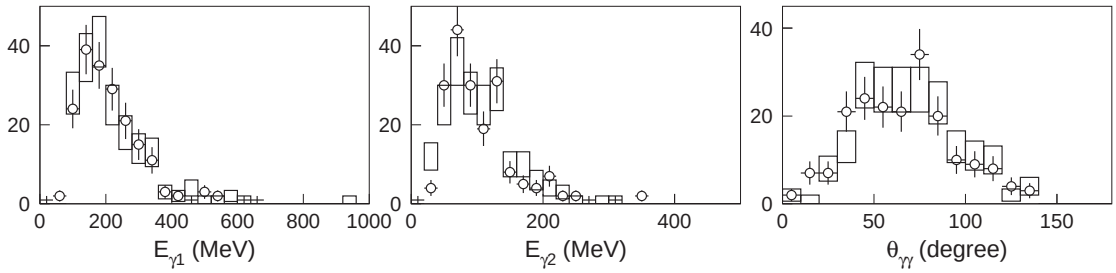

(b) SK=II

Figure 7.13: Comparison of reconstructed gamma-ray energies and opening angle between the standard reconstruction and the π^0 fitter for SK-I (upper) and SK-II (lower). The open boxes show the distributions for the standard reconstruction, and the open circles show that for the π^0 fitter.

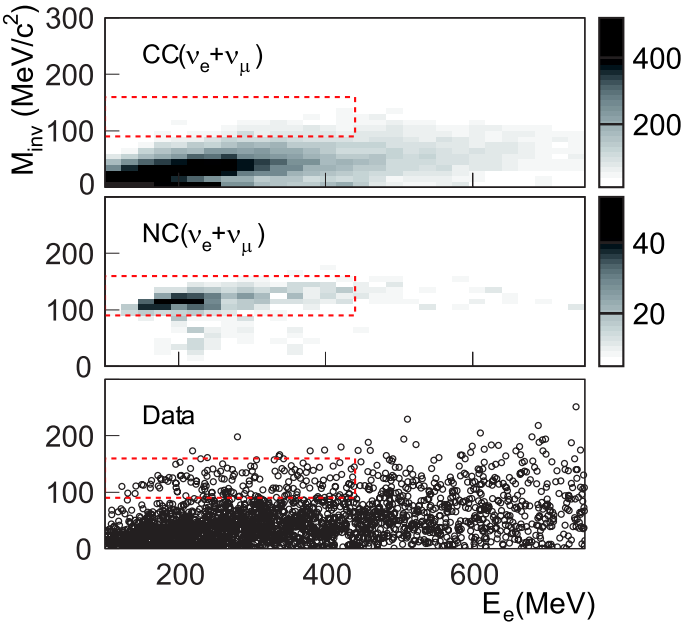

Figure 7.14: Event distribution of atmospheric neutrinos in M_{inv}-E_e space. The upper and middle figures shows the CC and NC interaction in the MC simulation, respectively. The lower shows the data. The boxes indicate the region where the π^0 events lie, expected by the MC simulation.

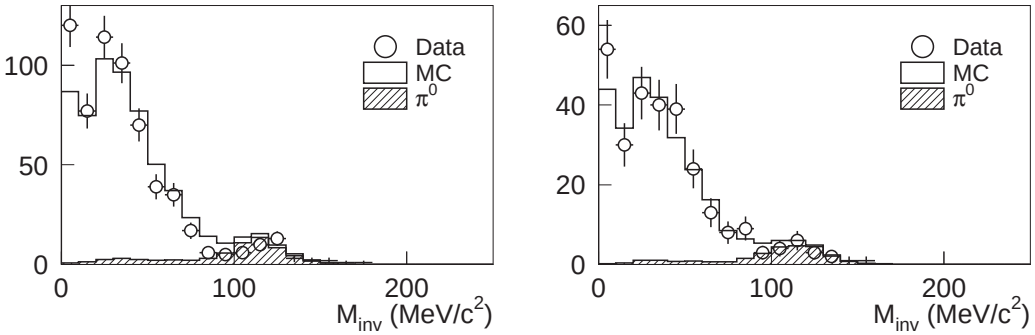

Figure 7.15: Invariant mass distribution of single-ring shower-type events for atmospheric neutrinos in SK-I (left) and SK-II (right). The open circles and histogram show the data and the MC events, respectively. The contribution of π^0 events is shown by the hatched region.

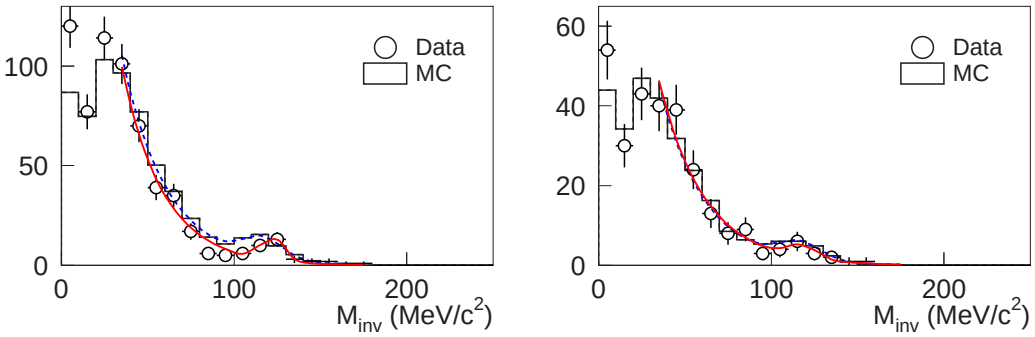

Figure 7.16: Invariant mass distribution of single-ring shower-type events of atmospheric neutrinos for SK-I (left) and SK-II (right). The distributions are fitted by a combination of the Gaussian function with the exponential function. The results are shown by the solid (dashed) lines for the data (the MC events).

We perform another check for e/π^0 separation using the events with two rings where one is MIP-type and the other is shower-type (two-ring $\mu - e$ sample). This kind of event topology is mainly attributed to the π^0 production via CC interaction ($\nu_\mu + N \rightarrow \mu + \pi^0 + N'$) where a muon and only one gamma-ray are reconstructed. After masking the hits associated with the MIP-type ring, we obtain the sample similar to the π^0 background events. We applied the π^0 fitter to this sample, and reconstructed the invariant mass as shown in Figure 7.17. We find the π^0 events in this two-ring $\mu - e$ sample by the π^0 fitter. The M_{inv} peaks of the data and the MC simulation for SK-I (SK-II) are $120 \pm 7 (117 \pm 8)$ MeV/c^2 and $117 \pm 2 (116 \pm 2)$ MeV/c^2, respectively. The data and the MC events show a good agreement, and values of the M_{inv} peaks are also consistent between the data and the MC events.

We checked the validity of the π^0 fitter and confirmed the performance with the real data as we expected in the MC simulation.

7.6 π^0 rejection for the K2K data sample

In this section, we apply the π^0 fitter in the selection criteria of ν_e signal candidate events.

Using the invariant mass M_{inv} of two gamma-rays given by the π^0 fitter and the

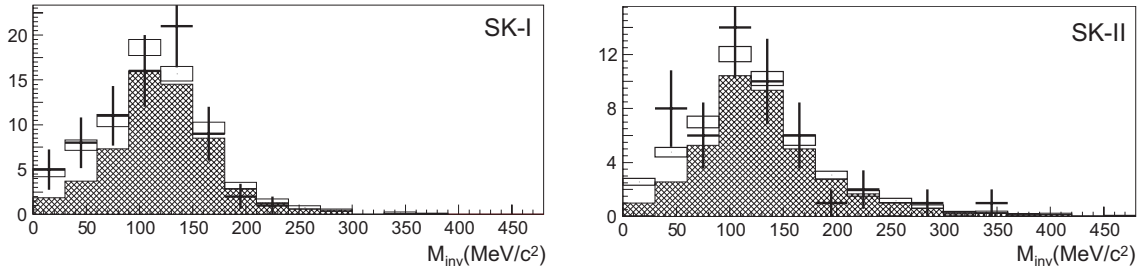

Figure 7.17: Reconstructed π^0 invariant mass distributions of two-ring μ-e sample for atmospheric neutrinos. The points with error bars and boxes show data and the MC events, respectively. The hatched histogram shows the fraction of π^0 production in the MC simulation. The left and right figure show SK-I and SK-II, respectively. The fitted peaks of data and the MC events are $120\pm7(117\pm8)$ MeV/c^2 and $117 \pm 2(116 \pm 2)$ MeV/c^2, respectively.

shower-type ring energy E_e as estimators, we separate the ν_e signal events from the π^0 background events. The resultant M_{inv}-E_e plot is shown in Figure 7.18. The selection boundary is set to be 100 MeV/c^2. Here, we consider that the resolution of invariant mass is poor for π^0 events with low momentum, while the ν_e signal events with a small E_e tend to have a small value of M_{inv}, as shown in Figure 7.10. Thus, in the region of $E_e < 400$ MeV, we apply a tighter M_{inv} cut to the event. The resultant selection cut is set to be

$$\begin{cases} M_{inv} < \dfrac{3E_e}{20} + 40 \text{ MeV} & \text{for } E_e < 400 \text{ MeV}, \\ M_{inv} < 100 \text{ MeV} & \text{for } E_e \geq 400 \text{ MeV}. \end{cases} \tag{7.4}$$

The signal region is optimized to maximize the sensitivity for the $\nu_\mu \rightarrow \nu_e$ signal with $\sin^2 2\theta_{\mu e} = 0.05$ and $\Delta m^2 = 2.8 \times 10^{-3}$ eV^2, based on the MC study.

After the π^0 rejection, we find one surviving event in K2K-II.

7.7 Summary of data reduction

The reduction of the data, the background and signal expectations according to the MC simulation are summarized in Table 7.1 and 7.2. The MC events are normalized by the expected number of FCFV events without oscillation, as described in Section 5.4. In the table, we consider the small fraction of the ν_e

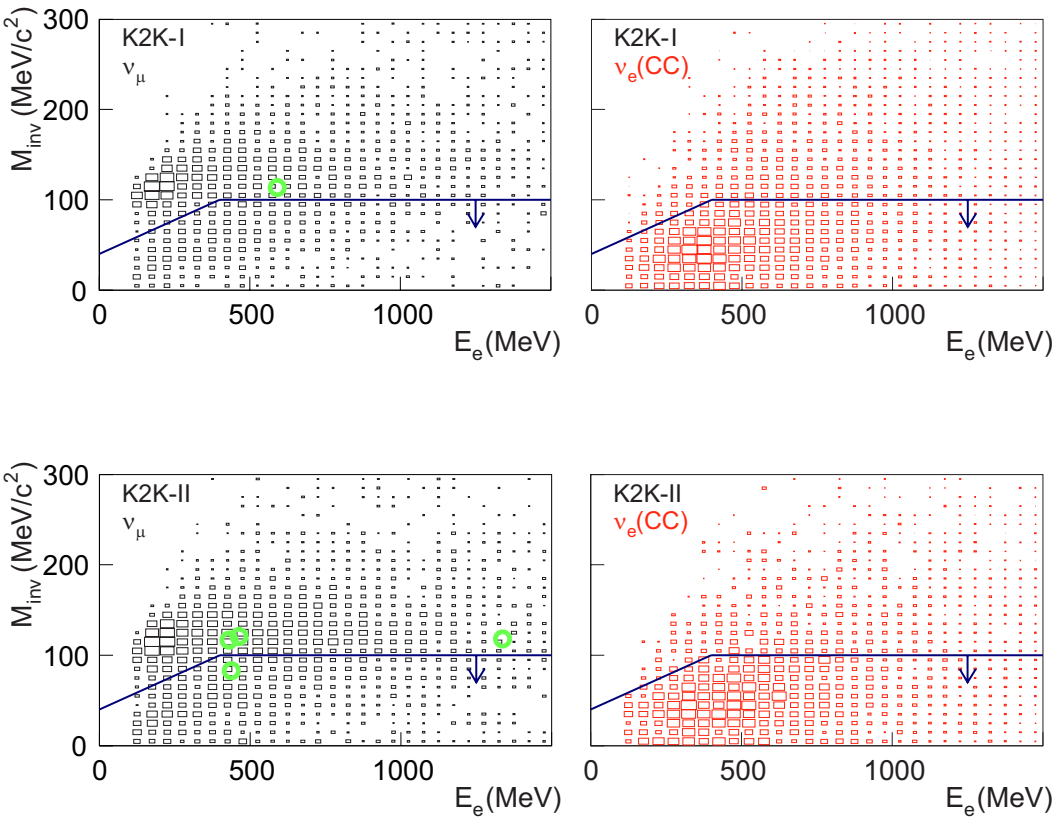

Figure 7.18: Distribution of candidate events in the M_{inv}-E_e space for K2K-I (upper) and K2K-II (lower). The left figures show the ν_μ background MC events, and the right ones show the ν_e signal MC events on the assumption of $\Delta m^2 = 2.8 \times 10^{-3}$. Surviving events before the π^0 rejection in data are shown by open circles. The selection boundary is also shown by a line with a bent.

contamination in the beam as shown in Figure 3.2. This beam-ν_e flux has been checked by the ν_e flux measurements of the near detectors (Appendix B).

The efficiency of ν_μ rejection and ν_e selection as a function of neutrino energy with all the selection cuts are shown in Figure 7.19. The overall efficiency for the selection of ν_e via CC interactions for K2K-I and K2K-II is 47% and 51%, respectively. This selection efficiency of K2K-II is a little larger than K2K-I, however, the ν_μ background expectation is also larger for K2K-II. That is due to the poor ring counting performance of SK-II for the second ring: SK-II has the lower PMT density than SK-I and the finding efficiency of second ring is slightly worse due to the lower image resolution. The overall ν_μ rejection factors are estimated to be 0.55% and 0.74% for K2K-I and K2K-II, respectively. In Figure 7.19, the tight rejection of ν_μ in the lowest energy bin is due to the visible energy cut. The lower ν_e selection efficiency above 1 GeV is due to the π^0 rejection cut: the events with a high energy electron have a large value of M_{inv}, and are rejected as π^0-like.

We have searched for a signal of $\nu_\mu \rightarrow \nu_e$ oscillation among one hundred and twelve beam neutrino events in SK. After all the selection cuts, we observed one signal candidate event in the data. This is consistent with the total background expectation of 1.7 events. The statistical tests of distribution are described in Appendix E. Five events remain before the final selection of π^0 fitter, and four of them are rejected as π^0-like. This rejection capability is consistent with what we expected: 70% of ν_μ-originated events are rejected by the invariant mass cut according to the MC simulation. The rejection of ν_μ-originated background for each interaction mode is summarized in Table 7.3.

Feature of the surviving event in the data

The event display of the single surviving event is shown in Figure 7.20. While this event is categorized as a single-ring shower-type event by the standard reconstruction procedure, we recognize that the π^0 fitter properly finds two possible rings like a π^0 event. With a manual examination of ring reconstruction, the surviving candidate event is revealed to have more than two rings. As a matter of fact, we found it is inconsistent with the π^0 mass with any combination of two rings. The CC and NC multi-meson production contributes to the classification of multi-ring event. The breakdown of the ν_μ-originated background expectation is given in Table 7.4. The fraction of the multi-hadron background event is estimated to be 12.7% for K2K-I and 15.7% for K2K-II, which results in the expectation of

Table 7.1: Reduction of events for $\nu_\mu \rightarrow \nu_e$ search at SK. The MC events are normalized by the expected number of FCFV events without oscillation. The first column lists each selection cut. The others give the number of observed events, ν_μ-originated background in the case of no oscillation and beam-ν_e for K2K-I and K2K-II, respectively. The ν_μ-originated background expectations with $\nu_\mu \rightarrow \nu_\tau$ oscillation of $\sin^2 2\theta_{\mu\tau} = 1$ and $\Delta m^2 = 2.8 \times 10^{-3}$ eV^2 are given in parentheses.

	K2K-I			K2K-II		
	data	ν_μ	beam-ν_e	data	ν_μ	beam-ν_e
FCFV	55	81.1 (54.18)	0.81	57	77.4 (51.55)	0.86
single ring	33	50.92 (30.59)	0.47	34	49.41 (29.72)	0.52
shower like	3	2.66 (2.41)	0.40	5	3.21 (2.81)	0.44
visible energy cut	2	2.47 (2.25)	0.40	5	2.93 (2.61)	0.44
no decay electron	1	1.90 (1.83)	0.35	4	2.17 (2.06)	0.39
non-π^0 like	0	0.58 (0.56)	0.17	1	0.74 (0.69)	0.21

Table 7.2: Reduction of ν_e signal MC events on the assumption of the oscillation parameters of $\sin^2 2\theta_{\mu e} = 1.0$ and $\Delta m^2 = 2.8 \times 10^{-3}$ eV^2. The MC events are normalized by the expected number of FCFV events without oscillation. The first column lists each selection cut. The second and third give the expected number of events for K2K-I and K2K-II, respectively. The efficiencies in each selection step are given in parentheses.

	K2K-I	K2K-II
FCFV	28.2 (97.3%)	24.7 (98.6%)
single ring	22.7 (78.3%)	19.8 (78.9%)
shower like	20.3 (70.0%)	18.3 (72.8%)
visible energy cut	20.1 (69.3%)	18.1 (72.2%)
no decay electron	18.3 (63.3%)	16.5 (65.7%)
non-π^0 like	13.7 (47.2%)	12.9 (51.3%)

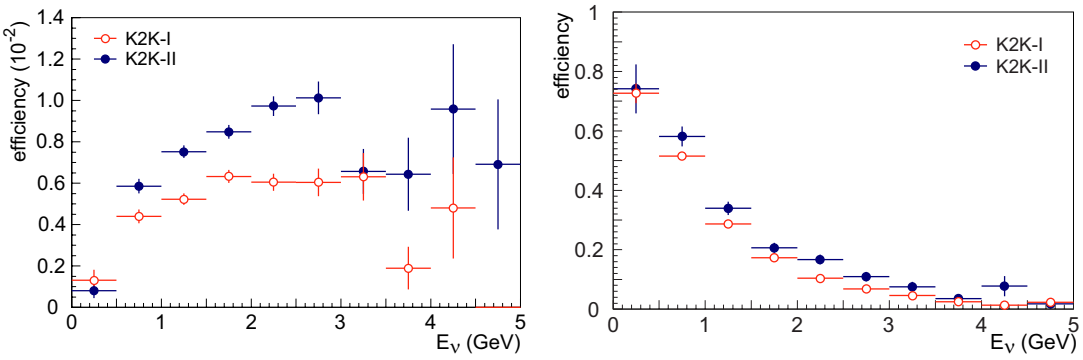

(a) ν_μ rejection

(b) ν_e selection efficiency

Figure 7.19: Efficiencies of ν_μ-originated background rejection (a) and ν_e signal selection (b) as a function of neutrino energy.

Table 7.3: ν_μ rejection factors after all the selection cuts for each interaction mode.

	K2K-I	K2K-II
CC-QE	6.8×10^{-4}	9.2×10^{-4}
CC single meson	1.2×10^{-3}	2.3×10^{-3}
CC multi mesons	9.9×10^{-4}	1.7×10^{-3}
NC	1.7×10^{-2}	2.3×10^{-2}

0.2 event. Thus, we conclude the surviving event could be originated from the multi-hadron production and it is consistent with the background expectation.

As a result, we found no evidence for a signature of $\nu_\mu \rightarrow \nu_e$ oscillation.

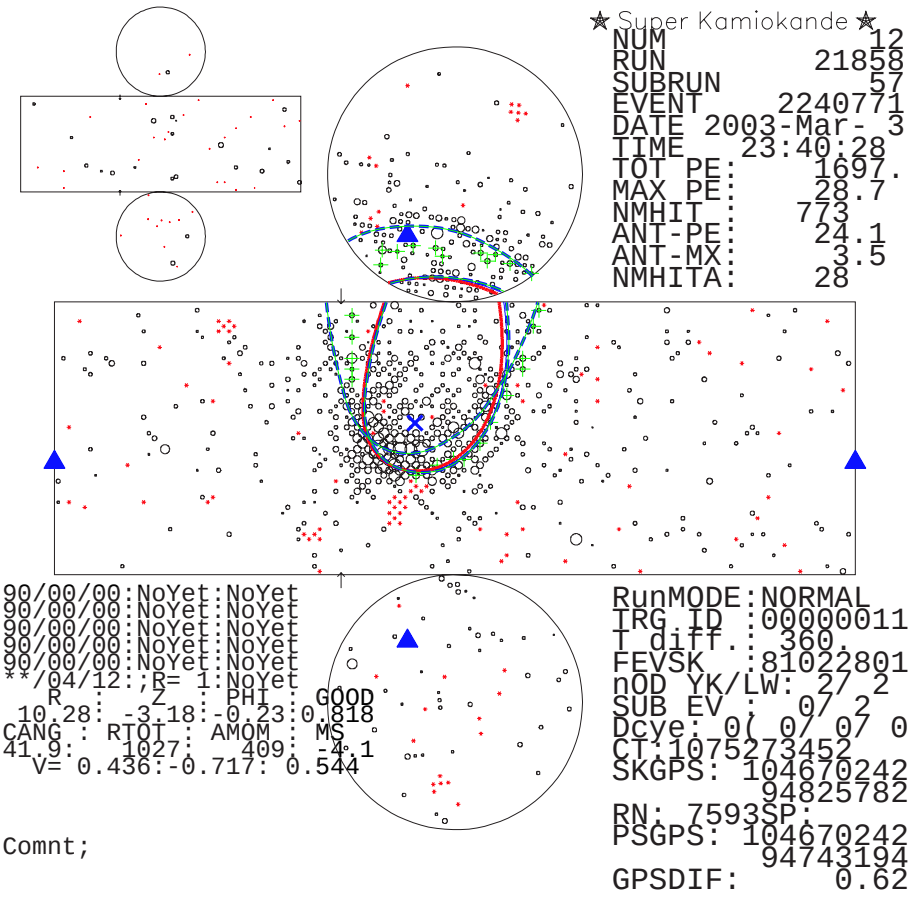

Figure 7.20: Single candidate event remaining after all selection cuts. The ring reconstructed by the standard fitter (solid line) and two rings by the π^0 fitter (dashed lines) are drawn.

Table 7.4: Breakdown of ν_μ background events after all the selection cuts.

	K2K-I	K2K-II
CC-QE	2.9%	5.5%
CC single π^0	2.5%	4.4%
CC single meson	2.2%	5.7%
CC multi mesons	2.2%	3.7%
NC single π^0	71.6%	57.4%
NC single meson	6.0%	8.6%
NC multi mesons	10.5%	12.0%
NC elastic	2.1%	2.7%

Chapter 8

Estimate of systematic uncertainties

In the measurement of $\nu_\mu \to \nu_e$ oscillation parameters, we compare the observed number of events with the expectation in SK. In this chapter, we estimate the systematic uncertainty of the expected number of events in SK.

The events in SK are classified into three categories: ν_μ-originated background, beam-ν_e background and ν_e appearance signal. We estimate the expected number of events for each of them. Then, the systematic uncertainties of normalization, interaction cross-section and selection efficiency are evaluated. Summary tables of the systematic uncertainties for each event category are given in the end of the chapter (Table 8.1, 8.2 and 8.3).

8.1 Expectation of the number of events in SK

The number of signal and background events are estimated based on the total number of neutrino interactions in SK (N_{SK}) described in Section 5.4.

The expected number of ν_e signal events, $\mathcal{S}_{\nu_e}$, is derived by multiplying the ratio of the expected signal event rate (r_{ν_e}) to the neutrino interaction rate without oscillation (r_{null}):

$$\mathcal{S}_{\nu_e} = N_{SK} \cdot \frac{r_{\nu_e}(\sin^2 2\theta_{\mu e}, \Delta m^2)}{r_{null}}, \tag{8.1}$$

$$r_{\nu_e}(\sin^2 2\theta_{\mu e}, \Delta m^2) \equiv \int dE_\nu \Phi_{SK}^{\nu_e}(E_\nu \mid \sin^2 2\theta_{\mu e}, \Delta m^2) \cdot \sigma(E_\nu) \cdot \epsilon_{SK}^{\nu_e}(E_\nu), \tag{8.2}$$

$$r_{null} \equiv \int dE_\nu \Phi_{SK}^{\nu_\mu, null}(E_\nu) \cdot \sigma(E_\nu) \cdot \epsilon_{SK}^{FCFV}(E_\nu), \tag{8.3}$$

where $\Phi_{SK}^{\nu_e}$, $\Phi_{SK}^{\nu_\mu,null}$, σ, $\epsilon_{SK}^{\nu_e}$ and ϵ_{SK}^{FCFV} are the ν_e flux at SK with oscillation parameters of $\sin^2 2\theta_{\mu e}$ and Δm^2, the ν_μ flux at SK without oscillation, the neutrino interaction cross-section with water, the ν_e detection efficiency after all the selection cuts and the ν_μ detection efficiency for the FCFV events without oscillation, respectively. The neutrino flux at near detectors (Φ_{ND}) and the far/near flux ratio are incorporated into ν_μ flux at SK:

$$\Phi_{SK}^{\nu_\mu,null}(E_\nu) = R_{F/N}(E_\nu) \cdot \Phi_{ND}(E_\nu). \tag{8.4}$$

In a two-flavor approximation, $\Phi_{SK}^{\nu_e}$ and the ν_μ flux $\Phi_{SK}^{\nu_\mu}$ are written as

$$\Phi_{SK}^{\nu_e}(E_\nu \mid \sin^2 2\theta_{\mu e}, \Delta m^2) = P_{\nu_\mu \to \nu_e}(E_\nu \mid \sin^2 2\theta_{\mu e}, \Delta m^2) \cdot \Phi_{SK}^{\nu_\mu,null}(E_\nu), \tag{8.5}$$

$$\Phi_{SK}^{\nu_\mu}(E_\nu \mid \sin^2 2\theta_{\mu e}, \Delta m^2) = \left[1 - P_{\nu_\mu \to \nu_e}(E_\nu \mid \sin^2 2\theta_{\mu e}, \Delta m^2)\right] \cdot \Phi_{SK}^{\nu_\mu,null}(E_\nu), \tag{8.6}$$

where $P_{\nu_\mu \to \nu_e}$ is the probability for $\nu_\mu \to \nu_e$ oscillation. To take into account the systematic uncertainty in σ, we classify interaction modes into four categories: CC-QE, CC other than CC-QE (CC non-QE), NC1π^0 and NC other than NC1π^0 (NC-other).

Similarly, the expected numbers of background events originated from ν_μ and beam ν_e, B_{ν_μ} and $B_{beam-\nu_e}$, are written as follows:

$$\mathcal{B}_{\nu_\mu} = N_{SK} \cdot \frac{r_{\nu_\mu}(\sin^2 2\theta_{\mu e}, \Delta m^2)}{r_{null}}, \tag{8.7}$$

$$\mathcal{B}_{beam-\nu_e} = N_{SK} \cdot \frac{r_{beam-\nu_e}}{r_{null}}, \tag{8.8}$$

where r_{ν_μ} and $r_{beam-\nu_e}$ are obtained by replacing the flux and the detection efficiency of ν_e in Equation 8.2 with those of ν_μ and beam ν_e. The beam-ν_e flux at SK is estimated based on the beam MC simulation.

When we estimate the expected numbers of events and the uncertainties, we take into account the differences of neutrino fluxes and detector systematics between the experimental phases (K2K-Ia, K2K-Ib and K2K-II).

Effect of neutrino oscillations

When neutrino oscillations occur, the estimation of the event selection efficiency and the number of events vary, which could affect the estimation of the systematic uncertainty.

For the ν_μ-originated background, NC interaction dominates as shown in Table 7.4. The number of background events is not so sensitive to ν_μ oscillation to ν_τ with parameters $\sin^2 2\theta_{\mu\tau} = 1.0$ and $\Delta m^2 = 2.8 \times 10^{-3}$ eV^2. It only affect the reduction of the number of background events by $\sim 5\%$ (Figure 9.1 in Section 9.1), which is much smaller than the systematic uncertainty. The contribution of ν_τ CC interactions is negligibly small. Thus, we do not account for the effect of $\nu_\mu \rightarrow \nu_\tau$ oscillation.

The effect of beam-ν_e oscillation is also negligible.

For the ν_e appearance signal, the ν_e energy spectrum depends on Δm^2 and the selection efficiency could be varied with Δm^2. Thus, we evaluate uncertainties by scanning Δm^2 and assign the maximum among them as the uncertainty.

8.2 Uncertainties of normalization

This section covers the systematic uncertainties related to the normalization: detector systematics of 1KT and SK, ν_μ energy spectrum, far/near flux ratio, neutrino fluxes and accumulated POT.

Detector systematics

In the estimate of event rate in SK, systematic uncertainties could originate from the event selection in the 1KT detector and SK.

For the 1KT detector, details are already described in Section 5.1 and the uncertainty is 4.1%.

For SK, a dominant contribution comes from the uncertainty of the fiducial volume definition. We use two vertex fitters to analyze the SK events as described in Section 6.1.2. Comparing the number of events in the fiducial volume between two fitters by using atmospheric neutrino data, we obtain the difference in the ratio of data to the MC events by 2%. This is assigned as a systematic uncertainty of the fiducial volume.

Another contribution comes from the uncertainty by the OD cut. Comparing the number of hits in an OD cluster between the data and the MC events for the partially contained events of atmospheric neutrinos, we evaluate a systematic uncertainty. The difference of the number of OD hits between the data and the MC events is estimated to be 15% (30%) for SK-I (SK-II). A change of the OD cut threshold by this difference varies the expected

number of events by 0.2% (0.4%) for K2K-I (K2K-II). We assign it as the systematic uncertainty.

We estimate the total uncertainty of 3% on the expected number of events due to the uncertainty of SK detector.

ν_μ energy spectrum

We estimate the ν_μ energy spectrum at SK by using the measured ν_μ energy spectrum at near detectors. The uncertainty due to the ν_μ energy spectrum is derived from the error of the spectrum measurement at near detectors given in Table 5.4.

Far/near flux ratio

The uncertainty from the far/near flux ratio is estimated from the errors of $R_{F/N}$ given in Equation 5.4.

Number of protons on target

In the normalization of SK events, the correction of POT (POT_{SK}/POT_{1KT}) is applied to account for the difference of live time between 1KT and SK. The uncertainty due to the POT correction is estimated as

$$\frac{POT_{SK} - POT_{1KT}}{POT_{1KT}} \cdot \delta S, \tag{8.9}$$

where δS is the stability of the 1KT event rate, evaluated to be ±6% considering the full spread of the event rate fluctuation (Figure 5.3). We estimate the uncertainties in the number of events for K2K-Ia, K2K-Ib and K2K-II to be ±1.0%, ±0.6% and ±0.3%, respectively.

Pion/kaon production in $p - Al$ collisions

Muon and kaon decays contribute to the beam-ν_e flux as shown in Figure 3.3, and we evaluate their uncertainties in the number of beam-ν_e events.

To estimate the uncertainty of the pion production, we adopt alternative pion production models in its production [35]. Comparing between our default model and alternative models, we evaluate the error on the flux ratio of beam-ν_e to ν_μ at SK as shown in Figure 8.1. Varying the ν_e/ν_μ ratio by its error, we estimate that the beam-ν_e flux uncertainty affects the number of beam-ν_e background events by $^{+14.5}_{-11.2}$%($^{+14.1}_{-11.5}$%) for K2K-I (K2K-II).

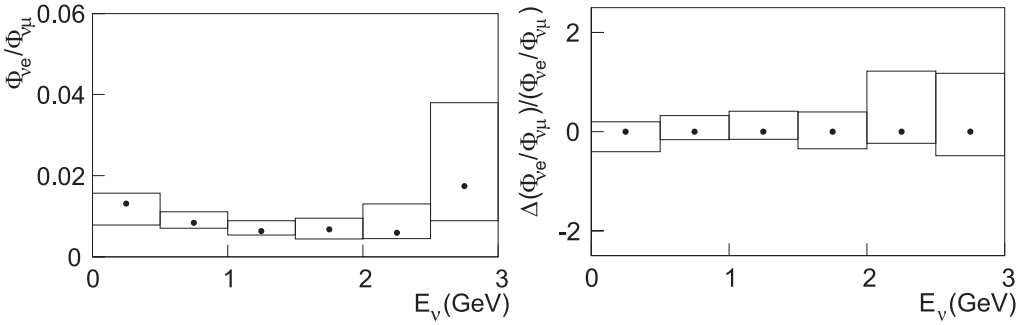

Figure 8.1: Flux ratio of beam-induced ν_e to ν_μ at SK (left). The beam MC prediction with our default pion production model is shown by circles. The error boxes show the the maximal deviation from our default model for alternative pion production models. The right figure shows the relative deviation.

For the kaon production, there is no available data. Therefore, a 100% fraction of ν_e yield from kaon decays is conservatively treated as the systematic uncertainty, which results in an uncertainty of ±15.8% in the expected number of beam-ν_e events.

8.3 Uncertainties of neutrino interaction cross-sections

In this section, we describe the uncertainties in neutrino interaction cross-section which mainly affect the estimate of the number of ν_μ-originated background events.

Neutral current cross-sections

The NC1π^0 background has a 70% fraction in the total background events. For understanding the cross-section in the water, we have measured the cross-section ratio of NC1π^0 production to CC interaction (NC1π^0/CC) [72] with the 1KT detector. NC1π^0 events are selected by extracting events with two shower-type rings. Then, the events are required to have the invariant mass within the range $85 - 215\mathrm{MeV/c^2}$. The CC interactions are selected in the same procedure as the ν_μ energy spectrum measurement [56]. The 1KT measurement of NC1π^0/CC gives $0.064 \pm 0.001(stat.) \pm 0.007(sys.)$, and our MC simulation predicts the ratio to be 0.065. Taking into account the errors on this measurement and the difference between the two central values, we evaluate the uncertainty of 12% to the NC1π^0/CC ratio.

For NC interaction other than NC1π^0, we quote an uncertainty of 20% in the cross-section ratio to CC as in Reference [73].

Varying these cross-sections by their errors, we estimate the contributions to the systematic uncertainty for the number of ν_μ-originated background events. The estimated uncertainties are $\sim$ 8% and $\sim$ 2% from NC1π^0 and NC-other, respectively. The contributions to the beam-ν_e prediction are estimated in the same way.

NC coherent π^0 production model

For the coherent NC π^0 production, the model of Rein and Sehgal [74] with modification by Marteau *et al.* [75] is used in our MC simulation. However, the measurement of CC coherent pion production cross-section with SciBar [76] is consistent with no CC coherent pion signal; this indicates the possibility that the cross-section of the NC coherent π^0 production is also considerably smaller than the MC prediction assuming the isospin relation. Considering that, the difference between the zero NC coherent pion production case and the model of Rein and Sehgal is taken into account as an systematic uncertainty, which affects the number of ν_μ-originated background events by $^{+3}_{-10}$%.

π^0 spectrum in the water

Final state interactions of nucleons and mesons inside of nuclear matter could substantially alter the π^0 momentum, which affect the expected number of π^0 background events. In order to account for the uncertainty of the π^0 spectrum in our simulation, we have checked the differences of the π^0 spectra between the 1KT data and the MC simulation. In the 1KT detector, π^0 events are selected as described in Section 7.3. Figure 8.2 shows the reconstructed π^0 momentum distribution in 1KT. Reshaping the MC π^0 spectra of SK by the differences of π^0 momentum between data and the MC events in 1KT, without changing the normalization, we estimate the contribution to the number of ν_μ-originated background events. It is estimated to be 8.0% and 9.6% for K2K-I and K2K-II, respectively.

CC non-QE cross-sections

The uncertainty in CC non-QE cross-section has an effect mainly on the numbers of ν_e signal and beam-ν_e events. Varying this cross-section by its

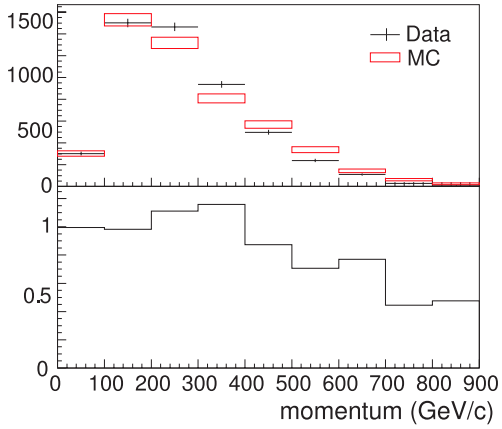

Figure 8.2: Reconstructed π^0 momentum distribution in the 1KT detector (upper). The dots with error bars and the boxes show data and the MC events, respectively. The ratio of data to the MC events is also shown (lower).

uncertainty from the near detector measurement of 20%, the uncertainty in the expected number of events is estimated to be about 5% for both of ν_e signal and beam-ν_e. The uncertainty in the ν_μ-originated background is estimated to be $\sim$ 1%.

8.4 Uncertainties of selection efficiency

We describe the uncertainty of the selection efficiencies in this section.

Ring counting

Most of the ν_μ-originated background events comes from π^0's. To estimate the uncertainty due to the ring counting for the ν_μ-originated background, we have compared the distributions of ring counting estimator for the atmospheric neutrino data and the MC events with two shower-type rings. The selection criteria for π^0 events is described in Section 7.3. The distribution of the ring counting estimator for the two-ring shower-type events is shown in Figure 8.3. We define the uncertainty of ring counting estimator for ν_μ-originated background events as the difference of the peak position (Δ) between data and the MC events: $\Delta \equiv \mid \mu_{data} - \mu_{MC} \mid + \sqrt{(\Delta\mu_{data})^2 + (\Delta\mu_{MC})^2}$, where $\mu_{data(MC)}$ and $\Delta\mu_{data(MC)}$ is the peak position and its error for data (MC events), respectively. The distribution is fitted with Gaussian function to

find the peak position. Shifting the MC distribution of the ring counting estimator by Δ, we estimate the change of the expected number of events. We apply this change as the systematic uncertainty due to the ring counting, which results in ±4.3% (±3.5%) for K2K-I (K2K-II).

For the signal ν_e and beam-ν_e events, we have performed the similar procedure as described above. The MC shift value is evaluated by using single-ring shower-type events of atmospheric neutrinos in the energy range up to several GeV. We estimate the contributions to the beam-ν_e and ν_e signal predictions for K2K-I (K2K-II) to be ±3.1% (±1.3%) and $^{+2.3}_{-6.9}$% ($^{+1.3}_{-2.9}$%), respectively.

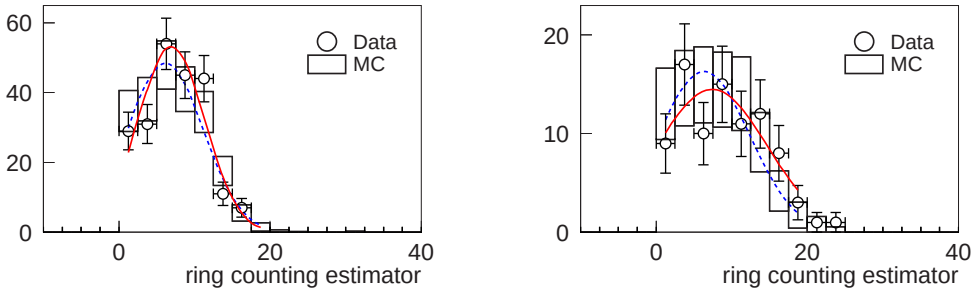

Figure 8.3: Distribution of ring counting estimator for atmospheric neutrino events with two shower-type rings. The open circles and boxes show the data and the MC events, respectively. The peak position is estimated to be $7.5 \pm 0.3 (7.1 \pm 0.7)$ for the data and 6.8 ± 0.1(6.7 ± 0.1) for the MC events in SK-I (SK-II). The fitted Gaussian functions for the data and the MC events are indicated by solid and dashed lines, respectively.

Shower-type ring identification

The systematic uncertainty due to the particle identification is estimated with a similar procedure to that for the ring counting, using atmospheric neutrinos. The contribution to the expected number of events for K2K-I (K2K-II) is estimated to be $^{+2.4}_{-4.9}$% ($^{+6.1}_{-6.9}$%), $^{+4.6}_{-6.1}$% ($^{+7.2}_{-5.1}$%) and $^{+4.3}_{-5.0}$% ($^{+3.6}_{-5.0}$%) for the ν_μ-originated background, beam-ν_e and signal ν_e, respectively.

Decay-electron tagging

Figure 8.4 shows the detection efficiency of decay-electrons measured by

using cosmic-ray muons which stop inside the inner detector. The uncertainty in the decay-electron tagging is estimated from the difference of the efficiency between data and the MC events. Varying the efficiency by this difference, we estimate the uncertainties of 1.7% and 1.1% in the number of ν_μ-originated background events for K2K-I and K2K-II, respectively.

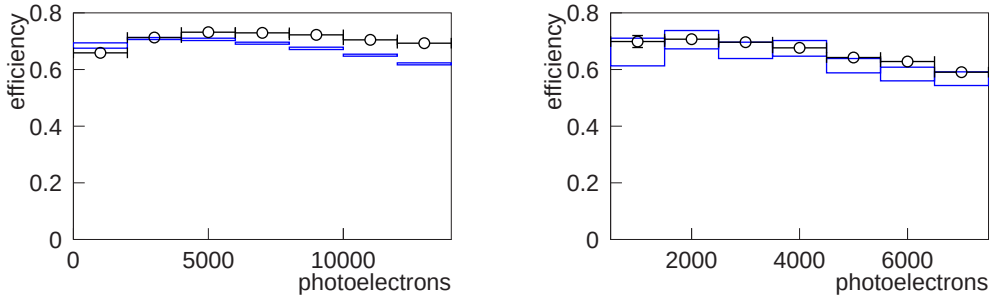

Figure 8.4: Detection efficiency of decay-electrons for SK-I (left) and SK-II (right). The open circles and boxes show the data and the MC events, respectively. The efficiencies are shown as a function of observed photoelectrons.

π^0 rejection cut

The uncertainty of π^0 rejection comes from the nuclear effects(e.g., final state interactions and nuclear deexcitations [77]), the variations of water properties and other possible reconstruction biases. To account for these contributions, we have compared the M_{inv} distributions of atmospheric neutrinos between the data and the MC events; the *in situ* measurements of π^0 events with only one reconstructed shower-type ring have been already described in Section 7.5. In this sample, the difference of M_{inv} peak position between data and the MC events is estimated to be less than 10 MeV including statistical uncertainty. The other sample of π^0, two-ring $\mu - e$ events, also gives an uncertainty of 10 MeV in the reconstructed invariant mass. We evaluate the uncertainty due to the M_{inv} cut by changing the selection boundary by 10 MeV. It is estimated to be $^{+18.6}_{-18.4}$% ($^{+18.9}_{-18.7}$%) for the ν_μ-originated background in K2K-I (K2K-II). For both of beam-ν_e and signal ν_e, the uncertainty is estimated to be about 6% (3%) for K2K-I (K2K-II).

Stability of water properties

There is a possibility that variations of water properties, such as light absorption, scattering and reflection, could affect the finding efficiency of a gamma-ray ring with small energy. These effects are estimated by changing the water properties in the MC simulation. To check the stability of water properties, we have measured the light attenuation length in SK using cosmic-ray muons during the entire running period. The attenuation length is measured from the observed photoelectrons corrected by the travel length of Cherenkov photons; the travel length is determined by the distance between a PMT and a muon track [78]. According to this measurement shown in Figure 8.5, the attenuation length is changed by ±20%(±15%) for SK-I (SK-II), which results in systematic effects of ±11.3% (±5.7%) on the number of ν_μ-originated events for K2K-I (K2K-II). The contributions to the signal ν_e and beam-ν_e predictions are estimated to be about 4%.

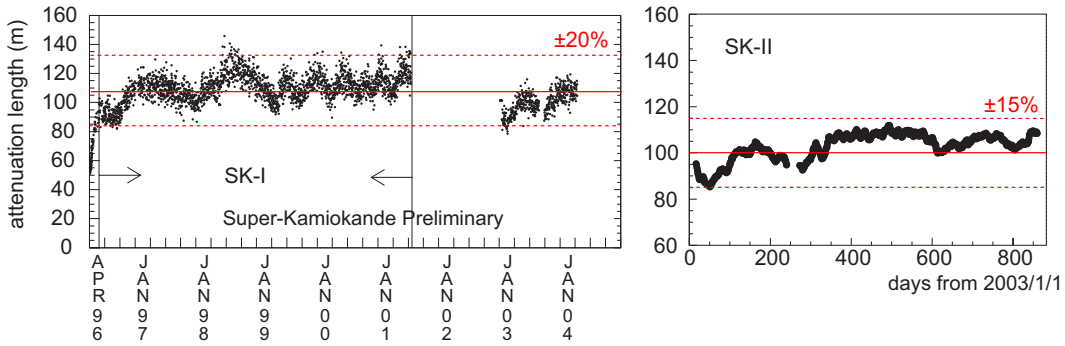

Figure 8.5: Stability of light attenuation length for SK-I (left) and SK-II (right).

8.5 Summary

Contributions of each systematic uncertainty in ν_μ-originated background, beam-ν_e background and ν_e signal expectations are summarized in Table 8.1, 8.2 and 8.3, respectively.

For the expectation of ν_μ-originated background, the dominant uncertainties are related to the π^0 production cross-sections and its rejection. This is due to the fact that the background is still dominated by the π^0 production events. Among those components, we have assigned the largest uncertainty on the π^0 rejection cut. The pion/kaon yield at the aluminum target is the main contribution

Table 8.1: Systematic uncertainties [%] in the expectation of ν_μ-originated background.

	K2K-I (K2K-Ia)	K2K-I (K2K-Ib)	K2K-II
1KT systematics	±4.1	±4.1	±4.1
SK systematics	±3	±3	±3
ν_μ energy spectrum	±13.6	$^{+5.1}_{-4.9}$	$^{+5.1}_{-4.8}$
Far/Near flux ratio	$^{+14.7}_{10.5}$	±2.8	$^{+2.9}_{-2.8}$
POT	±1.0	±0.6	±0.3
NC1π^0/CC cross-section ratio	±8.4	±8.4	±8.1
NC/CC cross-section ratio (for non-NC1π^0)	$^{+3.9}_{-3.7}$	$^{+2.4}_{-2.2}$	$^{+2.4}_{-2.3}$
NC coherent π^0 production model	$^{+2.8}_{-10.0}$	$^{+2.8}_{-10.0}$	$^{+2.6}_{-9.4}$
π^0 energy spectrum	±8.0	±8.0	±9.6
non-QE/QE cross-section ratio	$^{+1.6}_{-2.1}$	$^{+1.0}_{-0.9}$	$^{+1.0}_{-0.8}$
ring counting	±4.3	±4.3	±3.5
shower-type ring identification	$^{+2.4}_{-4.9}$	$^{+2.4}_{-4.9}$	$^{+6.1}_{-6.9}$
decay-e tagging efficiency	±1.7	±1.7	±1.1
π^0 rejection	$^{+18.6}_{-18.4}$	$^{+18.6}_{-18.4}$	$^{+18.9}_{-18.7}$
water properies	±11.3	±11.3	±5.7
total	$^{+33.8}_{-31.8}$	$^{+37.3}_{-25.6}$	$^{+39.3}_{-24.4}$

to the systematic uncertainty of the beam-ν_e flux. However, this uncertainty is not significant because the fraction of beam-ν_e events in the total background is small. For the expectation of ν_e signal events, the major sources originate from the measurements of the ν_μ energy spectrum and the non-QE/QE cross-section ratio.

In total, the expected number of events for ν_μ-originated background, beam-ν_e background are $1.32^{+0.50}_{-0.33}$, $0.38^{+0.12}_{-0.08}$, respectively. The numbers of total background events for K2K-I, K2K-II and K2K-I+II are estimated to be $0.75^{+0.21}_{-0.16}$, $0.95^{+0.30}_{-0.19}$ and $1.70^{+0.51}_{-0.34}$, respectively. When we incorporate all the systematic uncertainties in the expected number of events, we take into account the correlations between neutrino flux ration, fluxes and cross-sections according to Equation 5.4 and Table 5.4.

Table 8.2: Systematic uncertainties [%] in the expectation of beam-ν_e background.

	K2K-I		K2K-II
	(K2K-Ia)	(K2K-Ib)	
1KT systematics	±4.1	±4.1	±4.1
SK systematics	±3	±3	±3
pion production	$^{+14.5}_{11.2}$	$^{+14.5}_{-11.2}$	$^{+14.1}_{-11.5}$
kaon production	±15.8	±15.8	±15.8
POT	±1.0	±0.6	±0.3
NC1π^0/CC cross-section ratio	±0.2	±0.2	±0.2
NC/CC cross-section ratio (for non-NC1π^0)	±0.1	±0.1	±0.1
NC coherent π^0 production model	±0.2	±0.2	±0.2
non-QE/QE cross-section ratio	$^{+5.2}_{-6.5}$	$^{+4.7}_{-5.5}$	$^{+5.7}_{-5.5}$
ring counting	±3.1	±3.1	±1.3
shower-type ring identification	$^{+4.6}_{-6.1}$	$^{+4.6}_{-6.1}$	$^{+7.2}_{-5.1}$
decay-e tagging efficiency	±0.1	±0.1	±0.3
π^0 rejection	$^{+5.9}_{-6.2}$	$^{+5.9}_{-6.2}$	$^{+2.6}_{-2.3}$
water properies	±3.7	±3.7	±4.5
total	$^{+30.5}_{-20.3}$	$^{+32.5}_{-20.8}$	$^{+31.5}_{-22.8}$

Table 8.3: Systematic uncertainties [%] in the expectation of ν_e signal.

	K2K-I		K2K-II
	(K2K-Ia)	(K2K-Ib)	
1KT systematics	±4.1	±4.1	±4.1
SK systematics	±3	±3	±3
ν_μ energy spectrum	±16.0	$^{+6.8}_{-6.3}$	$^{+6.7}_{-6.3}$
Far/Near flux ratio	$^{+16.0}_{-10.0}$	±2.1	$^{+2.1}_{-2.2}$
POT	±1.0	±0.6	±0.3
NC1π^0/CC cross-section ratio	±1.4	±1.4	±1.4
NC/CC cross-section ratio (for non-NC1π^0)	±1.0	±1.0	±1.0
non-QE/QE cross-section ratio	$^{+5.2}_{-6.5}$	$^{+4.7}_{-5.5}$	$^{+5.7}_{5.5}$
ring counting	$^{+2.3}_{-6.9}$	$^{+2.3}_{-6.9}$	$^{+1.3}_{2.9}$
shower-type ring identification	$^{+4.3}_{-5.0}$	$^{+4.3}_{-5.0}$	$^{+3.6}_{-5.0}$
decay-e tagging efficiency	±2.7	±2.7	±0.3
π^0 rejection	$^{+5.7}_{-6.2}$	$^{+5.7}_{-6.2}$	$^{+2.2}_{-2.7}$
water properies	±3.7	±3.7	±4.5
total	$^{+24.7}_{-21.2}$	$^{+20.5}_{-13.6}$	$^{+19.8}_{-11.6}$

Chapter 9

Constraint on neutrino oscillation parameters

We obtained one signal candidate event in the data as described in Chapter 7. It is consistent with the background expectation of 1.7, and no evidence for $\nu_\mu \to \nu_e$ oscillation signal was found. Then the constraint on the neutrino mixing parameters is set by using one observed signal event with the MC background expectation. In this chapter, we calculate the upper limits on the oscillation parameters. We also describe the statistical analysis method, the comparison with the past experiments and the implication of our result for the future.

9.1 Calculation of upper limits

To set the upper limits on the $\nu_\mu \to \nu_e$ oscillation parameters in a two-flavor neutrino oscillation model, we adopt a confidence interval construction with the Poisson distribution using the expected number of events and the observed number. The expected number of events $\mathcal{N}_{exp}$ is represented by the sum of an appearance signal and two background components as

$$\mathcal{N}_{exp}(\sin^2 2\theta_{\mu e}, \Delta m^2_{\mu e}) = \mathcal{S}_{\nu_e}(\sin^2 2\theta_{\mu e}, \Delta m^2_{\mu e}) + \mathcal{B}_{\nu_\mu}(\sin^2 2\theta_{\mu e}, \Delta m^2_{\mu e}) + \mathcal{B}_{beam-\nu_e}, \quad (9.1)$$

where $\mathcal{S}_{\nu_e}$ is the number of ν_e signal events, $\mathcal{B}_{\nu_\mu}$ is the number of background events originated from ν_μ or oscillated ν_τ, and $\mathcal{B}_{beam-\nu_e}$ is the number of beam-ν_e events. $\mathcal{S}_{\nu_e}$ and $\mathcal{B}_{\nu_\mu}$ depend on the probability of $\nu_\mu \to \nu_e$ oscillation ($P_{\nu_\mu \to \nu_e}$).

$P_{\nu_\mu \to \nu_e}$ is expressed as

$$P_{\nu_\mu \to \nu_e}(E_\nu \mid \sin^2 2\theta_{\mu e}, \Delta m^2) = \begin{cases} \sin^2 2\theta_{\mu e} \cdot \sin^2(1.27 \cdot \Delta m^2 \cdot L/E_\nu) & \text{(for CC)}, \\ 0 & \text{(for NC)}, \end{cases} \tag{9.2}$$

where E_ν is neutrino energy in GeV and L is the flight distance of 250 km. Since the oscillation signature in the K2K experiment is smeared in the large Δm^2 region, we take an average of oscillation probability for CC interactions in Δm^2 region above the third oscillation maximum:

$$P_{\nu_\mu \to \nu_e}(E_\nu \mid \sin^2 2\theta_{\mu e}, \Delta m^2) = \tag{9.3}$$
$$\begin{cases} \sin^2 2\theta_{\mu e} \cdot \sin^2(1.27 \cdot \Delta m^2 \cdot L/E_\nu) & (\text{for } 1.27 \cdot \Delta m^2 L/E_\nu < \frac{11}{4}\pi) \\ \frac{1}{2} \sin^2 2\theta_{\mu e} & (\text{for } 1.27 \cdot \Delta m^2 L/E_\nu \geq \frac{11}{4}\pi). \end{cases}$$

When we estimate the contribution of $\nu_\mu \to \nu_\tau$ oscillation to $\mathcal{B}_{\nu_\mu}$, we assume the best-fit parameters of the K2K ν_μ disappearance analysis: $(\sin^2 2\theta_{\mu\tau}, \Delta m^2) = (1.0, 2.8\times10^{-3}\,\text{eV}^2)$. The effect of beam-$\nu_e$ oscillation is negligible. The formulations of $\mathcal{B}_{\nu_\mu}$, $\mathcal{B}_{beam-\nu_e}$ and $\mathcal{S}_{\nu_e}$ are given in Equation 8.7, 8.8 and 8.1, respectively. The dependence of the number of events on the oscillation parameters is shown in Figure 9.1. The number of background events is not sensitive to the $\nu_\mu \to \nu_e$ oscillation parameters. The number of ν_e signal events becomes maximum around $\Delta m^2 = 5 \times 10^{-3}$ eV^2.

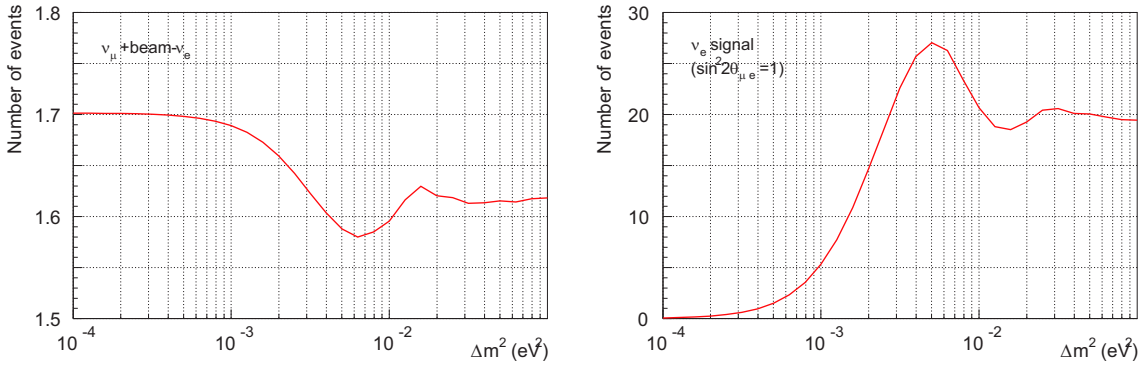

Figure 9.1: The expected number of events as a function of Δm^2. The left shows the total background, and the right shows the ν_e signal assuming $\sin^2 2\theta_{\mu e} = 1$.

9.1.1 Confidence interval with the unified method

We consider the Poisson distribution for the expected number of events to construct a confidence interval. In our case, the probability of getting a measured value of n events for a given set of oscillation parameters $P(n \mid \sin^2 2\theta_{\mu e}, \Delta m^2)$ is simply expressed as

$$\begin{aligned} P(n \mid \sin^2 2\theta_{\mu e}, \Delta m^2) &= \frac{\left(\mathcal{N}_{exp}\right)^n}{n!} e^{-\mathcal{N}_{exp}} \\ &= \frac{\left(\mathcal{S}_{\nu_e} + \mathcal{B}_{\nu_\mu} + \mathcal{B}_{beam-\nu e}\right)^n}{n!} e^{-\left(\mathcal{S}_{\nu e} + \mathcal{B}_{\nu \mu} + \mathcal{B}_{beam-\nu e}\right)}. \end{aligned} \tag{9.4}$$

For each value of Δm^2, a probability α (β) to observe n event more than (less than) the number of observed events n_{obs} is written as

$$\alpha = \sum_{n \geq n_{obs}} P(n| \sin^2 2\theta^{lo}_{\mu e}, \Delta m^2), \tag{9.5}$$

$$\beta = \sum_{n \leq n_{obs}} P(n| \sin^2 2\theta^{up}_{\mu e}, \Delta m^2), \tag{9.6}$$

Then, we obtain the confidence interval $[\sin^2 2\theta^{lo}_{\mu e}, \sin^2 2\theta^{up}_{\mu e}]$ which contains a fraction $1 - \alpha - \beta$.

For the construction of the confidence interval, the Bayesian approach is often applied. However, the Bayesian approach has the following issues:

- It do not cover the case when we measure a parameter near the physical boundary or null parameter.
- The true value of the parameter is treated as a random variable, and it does not provide a statistically exact confidence interval.

When we have a number of n_{obs} smaller than the expected background events, we obtain an anomalously low upper bound. In order to avoid these issues, we apply the unified method of Feldman and Cousins proposed in Reference [79]. It covers the treatment of the confidence interval for both of null and non-null results, and naturally provides two-sided intervals.

The Feldman and Cousins method introduces the ratio of likelihoods as an unified ordering principle when we select the values of n to place in the confidence interval, that is

$$R_T(n) = \frac{P(n|T)}{P(n|T_{best})}, \tag{9.7}$$

where T is the set of oscillation parameters ($\sin^2 2\theta_{\mu e}$, Δm^2), and T_{best} gives the highest probability for $P(n|T)$ in the physically allowed region of $\sin^2 2\theta_{\mu e}$ and Δm^2. The interval of $\mathcal{N}_{exp}$ is determined by adding values of n in decreasing order of R_T, until the sum of $P(n|T)$ exceeds the required confidence level (C.L.) as

$$\{\mathcal{N}_{exp}; R_T(\mathcal{N}_{exp}) \geq C_T\}. \tag{9.8}$$

where C_T is the lower bound on R_T for the required C.L. The notation $\{A; B\}$ represents a conditional ensemble of A satisfying B. Then, the unified intervals of oscillation parameters are defined as

$$\{T; R_T(\mathcal{N}_{exp}) \geq C_T\}. \tag{9.9}$$

9.2 Handling of systematic uncertainties

In order to implement the systematic uncertainties listed in Chapter 8, we convolute the Poisson probability with functions representing their probability densities of the expected number of events as follows:

(i) Suppose a certain set of oscillation parameters,

(ii) Define a toy model of the experiment with randomly generated systematic parameters listed in Table 8.1, 8.2 and 8.3,

(iii) Perform the virtual experiment for a case which the oscillation parameters is set above, and obtain the number of events in the Poisson regime,

(iv) Repeat the virtual experiment with various systematic parameters,

(v) Estimate the probability of observing n events from many virtual experiments.

The simple Poisson probabilities of Equation E.1 are replaced by the obtained probability densities. When we generate the systematic parameters, we suppose that each of them distributes as a Gaussian or an asymmetric Gaussian with the standard deviations of errors. For the near-to-far flux extrapolation, we take into account the correlations between the neutrino fluxes and cross-sections by adopting the error matrices given in Equations 5.4 and Table 5.4.

The probability densities as a function of the expected number of events are computed numerically in that way, and their distributions with some oscillation parameters are shown in Figure 9.2.

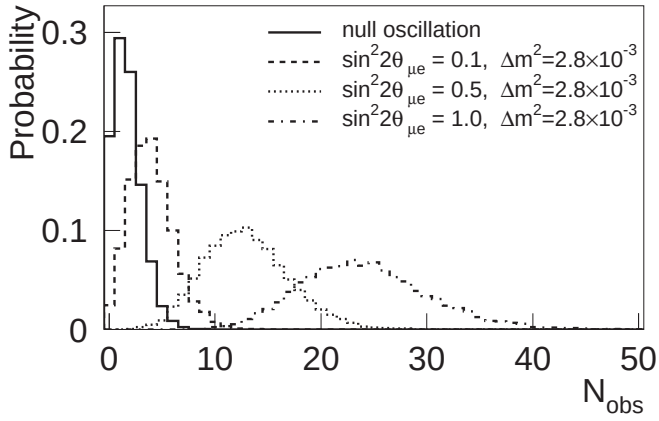

Figure 9.2: Probability density functions for K2K-I+II.

9.3 Results

Scanning along the oscillation parameter space and calculating the confidence intervals, we set the upper bound on the $\nu_\mu \rightarrow \nu_e$ oscillation parameters. We search a series of oscillation parameters where the confidence interval of 90% (99%) coverage probability would exclude the case of observing one event or below, as shown in Figure 9.3. Figure 9.4 shows the obtained upper bounds and experimental sensitivities at 90% and 99% C.L. for K2K-I, K2K-I and K2K-I+II. Here, the sensitivity is defined as the average of upper limits calculated from an ensemble of virtual experiments with the expected background and no true signal. The formulation is given as

$$\sum_n \nu_s^{up}(n \mid \sin^2 2\theta_{\mu e}, \Delta m^2) \times P(n \mid \sin^2 2\theta_{\mu e} = 0, \Delta m^2), \tag{9.10}$$

where the $\nu_s^{up}(n \mid \sin^2 2\theta_{\mu e}, \Delta m^2)$ is the upper limit of $\sin^2 2\theta_{\mu e}$ with the observation of n events, and $P(n \mid \sin^2 2\theta_{\mu e} = 0, \Delta m^2)$ is the probability that one would observe n events in the case of no oscillation, respectively. At the Δm^2 region of 2.8×10^{-3} eV^2, the neutrino oscillation from ν_μ to ν_e is constrained as

$$\begin{aligned} \sin^2 2\theta_{\mu e} &< 0.13 \quad (90\%\text{C.L.}), \\ &< 0.27 \quad (99\%\text{C.L.}). \end{aligned}$$

The most strict limit of $\sin^2 2\theta_{\mu e} < 0.10$ (90% C.L) is set at the region of $\Delta m^2 \sim 5 \times 10^{-3}$ eV^2. Upper bounds with independent data sets of K2K-I and K2K-II are also shown in Figure 9.4.

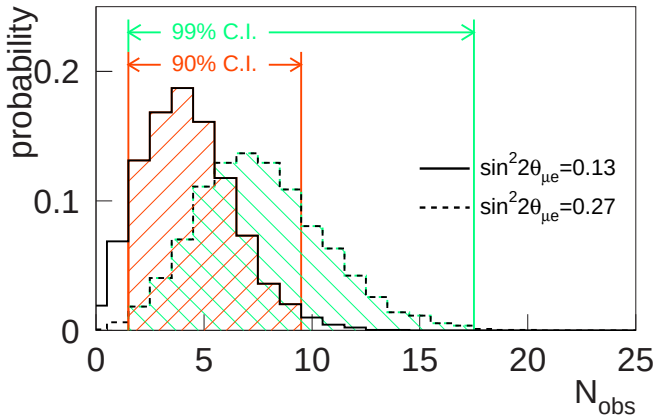

Figure 9.3: Confidence intervals at 90% and 90% coverage probabilities. The probability density functions are calculated assuming $\Delta m^2 = 2.8 \times 10^{-3}$eV^2.

9.3.1 Check with an alternative approach

As a check of the obtained result, we perform an alternative approach of constructing the confidence intervals. Figure 9.5 shows the comparison of upper bounds between the Feldman and Cousins method and the classical limit calculation with the single-sided interval. The classical method gives slightly strict limits, however, it is consistent with the result of Feldman and Cousins.

9.3.2 Effect of the systematic uncertainty

We estimate the uncertainty of $\sim$ 30% in the expected numbers of background events. Figure 9.6 shows the comparison of the upper bounds obtained with and without the systematic uncertainty. We found that the systematic uncertainty little affect the limit on $\sin^2 2\theta_{\mu e}$ with the current statistics. Figure 9.7 shows the expected sensitivities of $\sin^2 2\theta_{\mu e}$ as a function of POT with and without the systematic uncertainties. We suppose that the neutrino beam properties and the

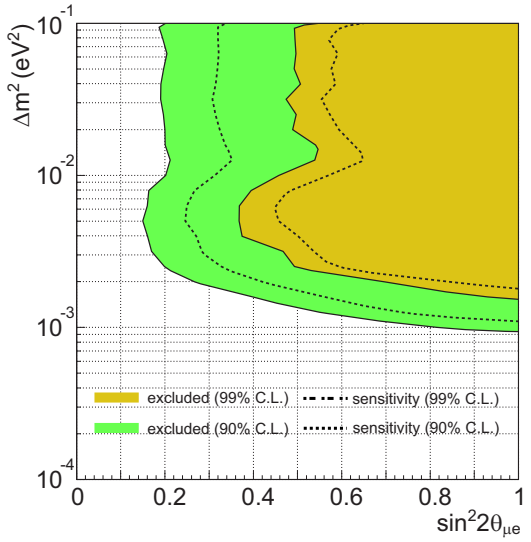

(a) K2K-I

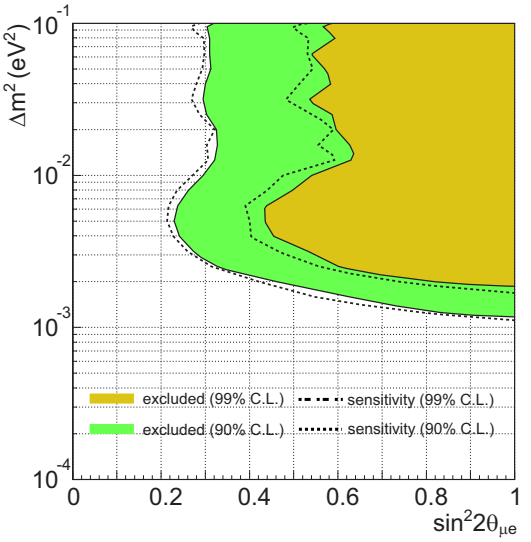

(b) K2K-II

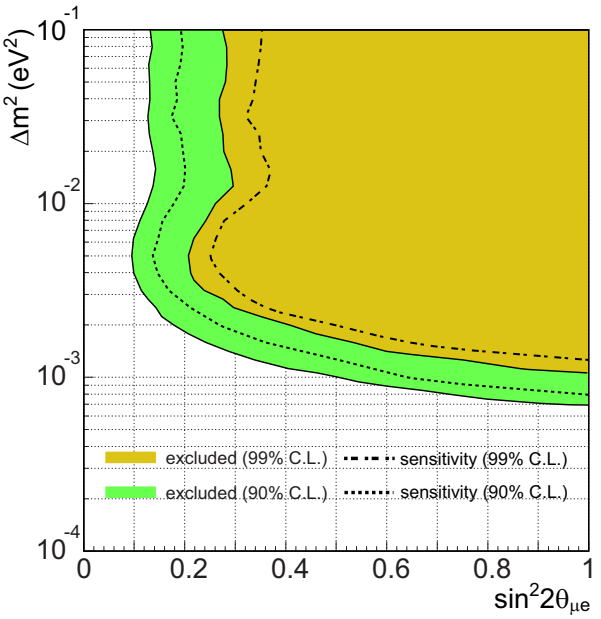

(c) K2K-I+II

Figure 9.4: Upper bounds of $\nu_\mu \to \nu_e$ oscillation parameters at 90% and 99% C.L. for K2K-I (a), K2K-II (b) and K2K-I+II (c). The sensitivities for each C.L. are also drawn with dashed (90%) and dot-dashed (99%) lines.

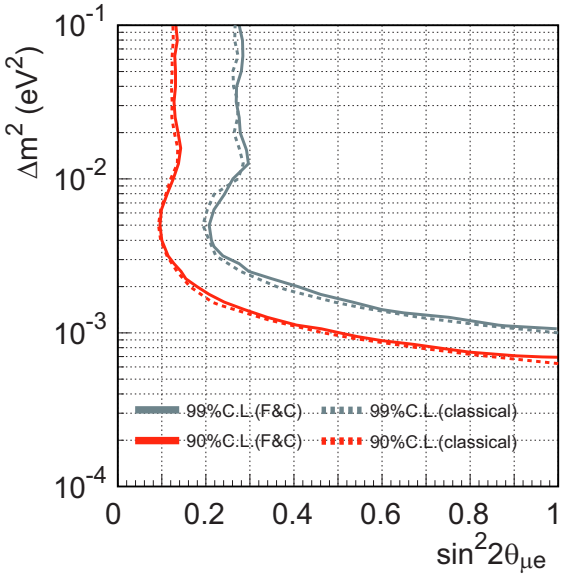

Figure 9.5: Comparison of upper bounds on $\nu_\mu \rightarrow \nu_e$ oscillation parameters between the Feldman and Cousins method (solid lines) and the classical limit calculation (dashed lines).

performances of the SK detector are similar to those of K2K-Ib in the calculation. The systematic uncertainty could become a dominant effect on the sensitivity if we collect more than 10 times statistics.

9.4 Discussion

We describe the comparison of our result with the past experimental results. Then we present our prospects of further neutrino oscillation searches.

9.4.1 Comparison with past experimental results

K2K-I published result

We have previously reported the search for $\nu_\mu \rightarrow \nu_e$ oscillation with the K2K-I data set [63]. We observed one signal candidate with the background expectation of 2.4 events. In the previous search, we applied the event selection without the π^0 fitter and found that the π^0 background events dominate. In fact, we concluded

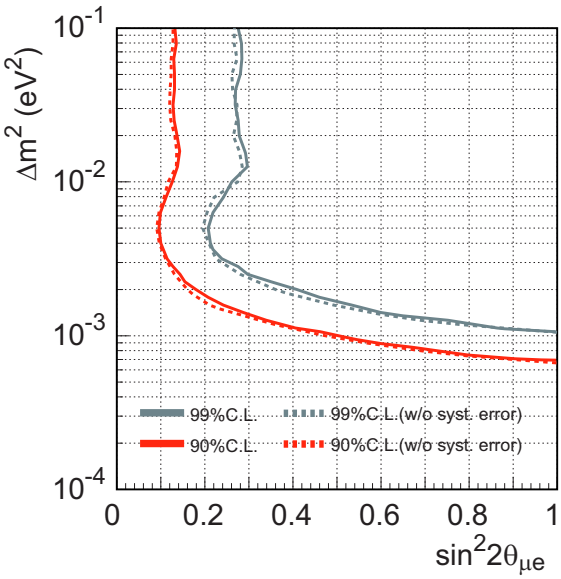

Figure 9.6: Upper bounds of $\nu_\mu \rightarrow \nu_e$ oscillation parameters with (solid line) and without (dashed line) systematic uncertainties.

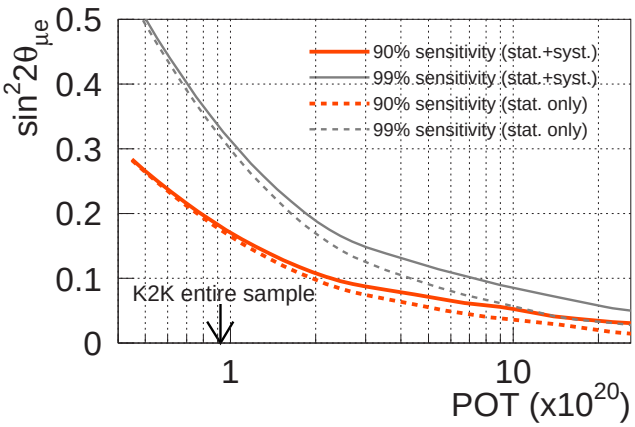

Figure 9.7: Expected sensitivities at 90% and 99% C.L. as a function of POT. The sensitivities for each C.L. with or without the systematic uncertainties are drawn by solid and dashed lines, respectively. The numbers of ν_e signal events are calculated on the assumption of $\Delta m^2 = 2.8 \times 10^{-3}$ eV^2.

that the observed event could be the π^0 production background by the visual examination.

In the new search, we have analyzed the entire K2K data sample which corresponds to almost the double statistics of our published results of K2K-I. We revised the signal selection by applying the π^0 fitter. The background events are suppressed by 70% and the signal candidate of K2K-I is rejected by the new cut. Consequently, we improved the sensitivity of $\nu_\mu \to \nu_e$ oscillation. The sensitivity of $\sin^2 2\theta_{\mu e}$ is 0.17 at $\Delta m^2 = 2.8 \times 10^{-3}$ eV^2 for the entire data sample; this is two times as strict as the previous one.

Results from reactor $\bar{\nu}_e$ experiments

As mentioned in Chapter 1, we can probe the neutrino mixing angle θ_{13} from our result on the assumption:

$$\sin^2 2\theta_{\mu e} \simeq \frac{1}{2} \sin^2 2\theta_{13}. \tag{9.11}$$

The limit on $\sin^2 2\theta_{13}$ is set as

$$\sin^2 2\theta_{13} < 0.26 \ (90\%\text{C.L.}) \tag{9.12}$$

at $\Delta m^2 = 2.8 \times 10^{-3}$ eV^2. Currently, this is most strict result on this mixing angle in $\nu_\mu \to \nu_e$ appearance experiments.

Further, the reactor $\bar{\nu}_e$ experiments with a few km baseline provide complementary results to the search for non-zero value of θ_{13} in K2K. In the Δm^2 region of 2.8×10^{-3} eV^2, the most stringent limit from the reactor experiments is $\sin^2 2\theta_{13} < 0.13$ by CHOOZ [20] and a weaker limit of < 0.20 is reported by Palo-Verde [21], showing a good agreement with our result. Constraints on Δm^2-$\sin^2 2\theta_{13}$ space by various experiments are shown in Figure 9.8. The allowed region given by Kamiokande [80] and the indicated space by SK [81] using atmospheric neutrinos, on the assumption of the three-flavor framework and the normal mass hierarchy, are also shown in the figure.

9.4.2 Future prospect of mixing angle θ_{13}

Measurement of the mixing angle θ_{13} is important to resolve the leptonic mixing and probe CP violation in the leptonic sector. The CP asymmetry A_{CP} is inversely

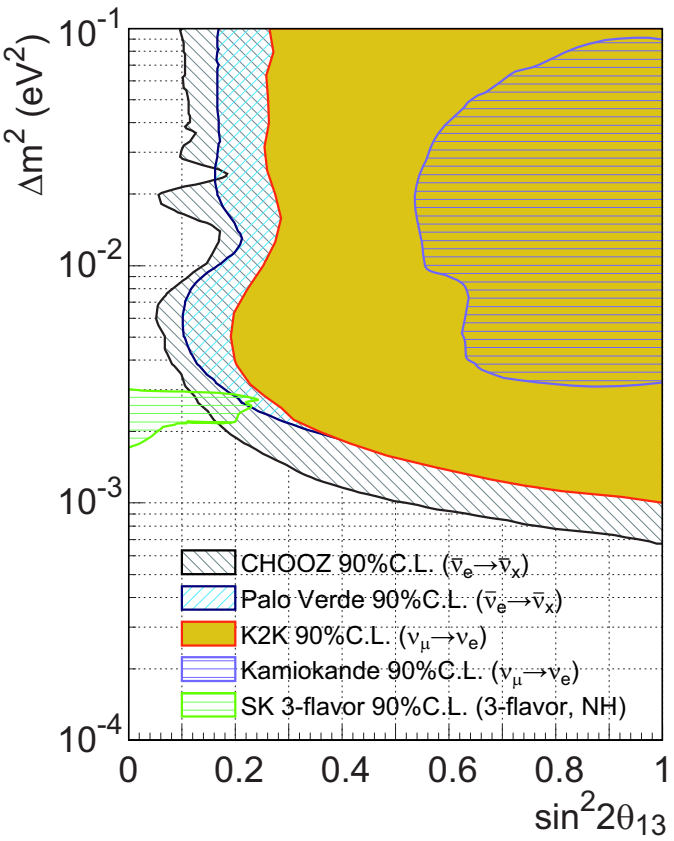

Figure 9.8: Constraints on Δm^2-$\sin^2 2\theta_{13}$ space by various experiments.

proportional to $\sin\theta_{13}$ as

$$A_{CP} = \frac{P_{\nu_\mu\to\nu_e} - P_{\bar{\nu}_\mu\to\bar{\nu}_e}}{P_{\nu_\mu\to\nu_e} + P_{\bar{\nu}_\mu\to\bar{\nu}_e}} = \left(\frac{\Delta m^2_{12} L \sin 2\theta_{12}}{4E_\nu}\right) \times \frac{\sin\delta}{\sin\theta_{13}}. \tag{9.13}$$

We believe the measurement of θ_{13} is the most important issue in neutrino physics for several years or a decade. Currently, no experiment shows the evidence of non-zero value of θ_{13}, and our resulting upper bound on the mixing parameters are still limited by statistics as shown in Figure 9.6. The experimental sensitivity of $\sin^2 2\theta_{13}$ reaches < 0.1 with ~ 10 times statistics in K2K, while the systematic uncertainty in the expectation of background events prevents us to improve the sensitivity. The π^0 production is still the dominant background and has a large contribution to the systematic uncertainty. For a further search, we need to reduce the π^0 background and improve the statistics.

In near future, some projects with nuclear reactors and high-intensity accelerators are planed or going to start to measure θ_{13} with large statistics; their sensitivity on $\sin^2 2\theta_{13}$ is expected to be $O(10^{-3})$. Especially, an accelerator experiment of T2K [82] is scheduled to start in a few years. T2K has some advantages in beam intensity and spectrum: the statistics is expected to become ~ 50 times as much as K2K for five years, and the neutrino beam energy is tuned to the oscillation maximum with a narrow spread to enhance the oscillation signature. However, T2K uses SK as the far detector. The NC π^0 production background is crucial as well as K2K, although the narrow band neutrino beam with averaged energy 0.8 GeV suppresses the resonance production of π^0. To settle this issue, we took the initiative in rejecting the π^0 background events and demonstrated the search for $\nu_\mu \to \nu_e$ oscillation in this thesis.

Hopefully, the mixing angle θ_{13} is not zero and will be addressed in the future experiments.

Chapter 10

Conclusions

We reported the results of the search for $\nu_\mu \rightarrow \nu_e$ oscillation in the K2K long-baseline neutrino oscillation experiment with the entire data sample of 9.2×10^{19} protons on target.

Our search for $\nu_\mu \rightarrow \nu_e$ signal is based on detection of charged current quasi-elastic interaction of ν_e in the Super-Kamiokande detector. The signature of ν_e appearance is the event with one shower-type Cherenkov ring generated by an electron. With this classification, the dominant background comes from π^0's induced by ν_μ NC interactions. A single π^0 decaying into two gamma-rays can be classified as a single-ring shower-type event, when one gamma-ray is not reconstructed. To improve the π^0 rejection capability, we developed a new π^0 reconstruction algorithm and validated its performances using atmospheric neutrino data. We revised the signal selection imposing the π^0 rejection cut and achieved the π^0 background suppression by 70%. As a result, we have improved the experimental sensitivity for $\nu_\mu \rightarrow \nu_e$ oscillation.

We search for a signal of $\nu_\mu \rightarrow \nu_e$ oscillation among one hundred and twelve beam neutrino events observed in SK. We find one signal candidate event, which is consistent with the background expectation of 1.7 events. We conclude that the event is consistent with the multi-hadron production background and there is no evidence for $\nu_\mu \rightarrow \nu_e$ oscillation. Then, we set the limit on the oscillation parameter space. In a two-flavor approximation, we set a constraint on $\sin^2 2\theta_{\mu e}$ as

$$\sin^2 2\theta_{\mu e} < 0.13 \quad (90\%\text{C.L.})$$

at $\Delta m^2 = 2.8 \times 10^{-3}$ eV^2. For the higher Δm^2 region, we set the more stringent limit of $\sin^2 2\theta_{\mu e} < 0.10$. Currently, our result is the most strict result on this mixing

angle in $\nu_\mu \to \nu_e$ appearance experiments.

Further, we can derive a constraint on θ_{13} from $\nu_\mu \to \nu_e$ oscillation. On the assumption of the relation $\sin^2 2\theta_{13} \simeq 2\sin^2 2\theta_{\mu e}$, we give a constraint on $\sin^2 2\theta_{13}$ as

$$\sin^2 2\theta_{13} < 0.26 \quad (90\%\text{C.L.})$$

at $\Delta m^2 = 2.8 \times 10^{-3}$ eV^2. Our result is consistent with the results from the reactor $\bar{\nu}_e$ experiments of CHOOZ and Palo-Verde that show the lack of observed disappearance of $\bar{\nu}_e$.

Appendix A

Neutrino interaction simulation

A.1 Neutrino interaction simulation

In the K2K experiment, we adopt the NEUT library to simulate the neutrino interactions with the target material. In NEUT, the following CC and NC interactions are considered: (quasi-)elastic scattering, resonance production, multi-pion production and coherent-pion production. In this chapter, we give descriptions of each interaction mode.

A.1.1 CC quasi-elastic scattering and NC elastic scattering

The charged current quasi-elastic (CC-QE) and neutral current elastic (NC-el) interactions are two-body scatterings of neutrino on a nucleon. The simulations of their cross-sections are based on Llewellyn Smith's formula [83]. Its amplitude is described as a product of hadronic and leptonic weak currents as

$$T = \frac{G_F}{\sqrt{2}} \bar{u}(k_2)\gamma^\mu(1-\gamma^5)u(k_1)\,\langle N'(p_2)|J_\mu^{\rm had}|N(p_1)\rangle, \tag{A.1}$$

where G_F is the Fermi coupling constant, p_1 (p_2) is the initial (final) nucleon four-momentum, and k_1 (k_2) is the initial (final) lepton four-momentum. The hadronic current, $\langle N'|J^{\rm had}|N\rangle$, can be expressed as a function of four-momentum transfer ($Q^2 \equiv -q^2 = -(p_1-p_2)^2$) as

$$\langle N'|J^{\rm had}|N\rangle = \cos\theta_c\,\bar{u}(N')\left[\gamma_\lambda F_V^1(Q^2) + \frac{i\sigma_{\lambda\nu}q^\nu\xi F_V^2(Q^2)}{2m_N} + \gamma_\lambda\gamma_5 F_A(Q^2)\right]u(N), \tag{A.2}$$

where θ_c is the Cabbibo angle, and m_N is the nucleon mass. The vector form factors, F_V^1 and F_V^2, are represented as follows:

$$F_V^1(Q^2) = \left(1 + \frac{Q^2}{4m_N^2}\right)^{-1} \left[G_E^V(Q^2) + \frac{Q^2}{4m_N^2} G_M^V(Q^2)\right], \tag{A.3}$$

$$\xi F_V^2(Q^2) = \left(1 + \frac{Q^2}{4m_N^2}\right)^{-1} \left[G_M^V(Q^2) - G_E^V(Q^2)\right], \tag{A.4}$$

$$G_E^V(Q^2) = \frac{1}{\left(1 + \frac{Q^2}{M_V^2}\right)^2}, \qquad G_M^V(Q^2) = \frac{1+\xi}{\left(1 + \frac{Q^2}{M_V^2}\right)^2}, \tag{A.5}$$

where $\xi \equiv \mu_p - \mu_n (= 3.71)$ is the difference of anomalous magnetic dipole moments between a proton and a neutron, and the vector mass in the dipole parametrization (M_V) is set to be 0.84 GeV/c. The axial form factor (F_A) is given by

$$F_A(Q^2) = \frac{-1.23}{\left(1 + \frac{Q^2}{M_A^2}\right)^2}, \tag{A.6}$$

where M_A is the axial vector mass. In NEUT, M_A is referred to electron-nucleon and neutrino-nucleon scattering experiments; they result in $1.0 - 1.1$ GeV/c^2 [84]. On the other hand, our measurement favors larger value of M_A around 1.11 GeV/c^2. Thus, in the current simulation, we set the standard value of M_A to 1.11 GeV/c^2.

Finally, the differential cross-section is expressed as follows:

$$\frac{d\sigma}{dQ^2} = \frac{m_N^2 G_F^2 \cos^2\theta_c}{8\pi E_\nu^2} \left[A(Q^2) \mp B(Q^2)\frac{(s-u)}{m_N^2} + C(Q^2)\frac{(s-u)^2}{m_N^4}\right] \tag{A.7}$$

where E_ν is the incident neutrino energy, $(s-u) \equiv 4m_N E_\nu - Q^2 - m_l^2$, m_l is the lepton mass, and

$$\begin{aligned} A(Q^2) = \frac{(m_l^2 + Q^2)}{4m_N^2} \Bigg[& \left(4 + \frac{Q^2}{m_N^2}\right)|F_A|^2 - \left(4 - \frac{Q^2}{m_N^2}\right)|F_V^1|^2 + \frac{Q^2}{m_N^2}|\xi F_V^2|^2 \left(1 - \frac{Q^2}{4m_N^2}\right) \\ & + \frac{4Q^2 F_V^1 \xi F_V^2}{m_N^2} - \frac{m_l^2}{m_N^2}\left(|F_V^1 + \xi F_V^2|^2 + |F_A|^2\right)\Bigg], \end{aligned} \tag{A.8}$$

$$B(Q^2) = -\frac{Q^2}{m_N^2} F_A \left(F_V^1 + \xi F_V^2\right), \tag{A.9}$$

$$C(Q^2) = \frac{1}{4}\left(|F_A|^2 + |F_V^1|^2 + \frac{Q^2}{m_N^2}\left|\frac{\xi F_V^2}{2}\right|^2\right). \tag{A.10}$$

The sign of $B(Q^2)$ in Equation (A.7) is − for neutrino and + for anti-neutrino.

Figure A.1 shows the cross-section for the CC-QE interaction as a function of neutrino energy. They are consistent with various bubble chamber measurements around 1 GeV [85, 86, 87, 88].

For the NC-el interaction, the cross-section is derived from following relations [89]:

$$\sigma(\nu p \to \nu p) = 0.153 \times \sigma(\nu n \to e^- p), \tag{A.11}$$

$$\sigma(\nu n \to \nu n) = 1.5 \times \sigma(\nu p \to \nu p). \tag{A.12}$$

The Fermi motion and the Pauli blocking effect are considered for the target nucleons bound in ^{16}O. In NEUT, the Fermi gas model is adopted to reproduce the Pauli blocking effect. The final nucleon momentum is required to be larger than the Fermi surface momentum, which is estimated to be 225 MeV/c for ^{16}O, based on an electron-^{12}C scattering experiment [90].

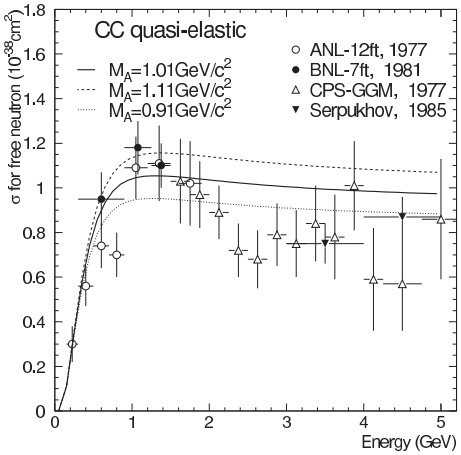

Figure A.1: Cross-section of CC-QE interaction on a free neutron in NEUT, together with the results of measurements by bubble chamber experiments. Horizontal axis is the incident neutrino energy. Solid, dashed, and dotted lines show the calculations of the cross-section in NEUT with M_A = 1.01, 1.11, and 0.91 GeV/c, respectively. Data points are from ANL [85], BNL [86], GGM [87], and Serpukhov [88].

A.1.2 Resonance production of single meson

The resonance production interaction produces one lepton and one pion via an intermediate baryon resonance state (N^*):

$$\begin{aligned} \nu + N &\rightarrow l^- + N^* \\ N^* &\rightarrow N' + \pi\ (\eta, K), \end{aligned} \tag{A.13}$$

where N (N') is a nucleons in initial (final) state. In the simulation, this production is based on the model of Rein and Sehgal [91]. The differential cross-section of the resonance production with the mass M is written by

$$\frac{d^2\sigma}{dQ^2 dE_\nu} = \frac{1}{32\pi m_N E_\nu^2} \cdot \frac{1}{2} \cdot \sum_{\text{spins}} |T(\nu N \rightarrow l N^*)|^2 \cdot \delta(W^2 - M^2), \tag{A.14}$$

where W is the invariant mass of the hadron system, and the width of the resonance decay is neglected. The amplitude of the resonance production, $T(\nu N \rightarrow l N^*)$, is calculated based on the FKR (Feynman-Kislinger-Ravndal) baryon model [92]. This model includes vector and axial-vector form factors using dipole parametrization with the same values of M_V and M_A as CC-QE interaction. The differential cross-section for the resonance, with a finite decay width Γ, is derived by replacing the δ-function in Equation (A.14) with a Breit-Wigner formula:

$$\delta(W^2 - M^2) \rightarrow \frac{1}{2\pi} \frac{\Gamma}{(W - M)^2 + \Gamma^2/4}. \tag{A.15}$$

In the simulation, $\Delta(1232)$ and other seventeen resonance states with $W < 2.0\,\text{GeV/c}^2$ are taken into account. Figure A.2 shows the the cross-section for each final state with $M_A = 1.01$ GeV/c^2 and experimental data [93, 94, 95]. In the case of $M_A = 1.11$ GeV/c^2, the cross-section is approximately 10% higher than that with $M_A = 1.01$ GeV/c^2. The cross-section is consistent with past experiments, no matter which M_A value is employed.

The decay kinematics of $\Delta(1232)$ is calculated by the model of Rein and Sehgal. For the other resonance states, the meson direction is determined under the assumption that it is isotropic in the rest frame of the resonance state.

A.1.3 Multi-meson production

In order to calculate the cross-sections of deep inelastic scattering, which is responsible for multi-pion production, we adopt the GRV94 [96] parton distribution

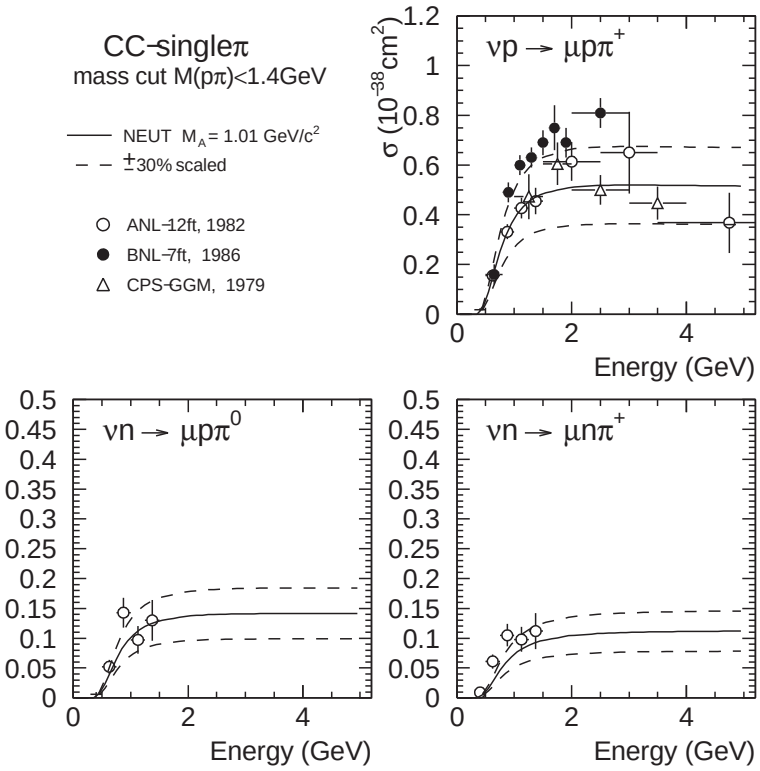

Figure A.2: The figuring of CC resonance production in NEUT program library and, experimental results. Solid lines show the calculation by NEUT, and dashed lines show the the cross-section scaled by ±30%, where M_A = 1.01 GeV/c^2. The experimental results from ANL [93], BNL [94], and GGM [95] are plotted here.

function with modifications by Bodek and Yang [97]. Its differential cross-section is given by integrating the following equation [98]:

$$\frac{d^2\sigma}{dxdy} = \frac{G_F^2 m_N E_\nu}{\pi} \cdot \left[(1 - y + \frac{1}{2}y^2 + C_1)F_2(x) + y(1 - \frac{1}{2}y + C_2)[xF_3(x)] \right] \tag{A.16}$$

$$C_1 = \frac{m_l^2(y-2)}{4m_N E_\nu x} - \frac{m_N xy}{2E_\nu} - \frac{m_l^2}{4E_\nu^2}$$

$$C_2 = -\frac{m_l^2}{4m_N E_\nu x}$$

where $x = Q^2/(2m_N(E_\nu - E_l) + m_N^2)$ and $y = (E_\nu - E_l)/E_\nu$ are the Bjorken scaling parameters, and E_l is the energy of the final state lepton. The nucleon structure functions, F_2 and xF_3, are taken from GRV94. In the calculation, the hadronic invariant mass, W, is required to be larger than 1.3 GeV/c^2. The Bodek-Yang modification of the functions effectively changes the cross-section by a Q^2-dependent factor as

$$\frac{d^2\sigma}{dxdy} \rightarrow \frac{Q^2}{Q^2 + 0.188} \cdot \frac{d^2\sigma}{dxdy}. \tag{A.17}$$

This reduces the cross-section in low Q^2 region, which is favored by our previous analysis [62, 56].

In the simulation of the kinematics of the hadronic system, two methods are adopted according to the invariant mass W. In the region of $1.3 < W < 2.0$ GeV/c^2, only pions are considered. The mean multiplicity of pions is estimated from the result of Fermilab 15-foot hydrogen bubble chamber experiment [99]:

$$\langle n_\pi \rangle = 0.09 + 1.83 \ln W^2. \tag{A.18}$$

The number of pions for each event is determined using KNO(Koba-Nielsen-Olesen) scaling [100]. Since the range of W overlaps with that in the resonance production mode, n_π is required to be larger than or equal to two in this W region. The forward-backward asymmetry of pion multiplicity is also taken into account to be [101]:

$$\frac{\langle n_\pi^F \rangle}{\langle n_\pi^B \rangle} = \frac{0.35 + 0.41 \ln W^2}{0.50 + 0.09 \ln W^2}. \tag{A.19}$$

In the region of W above 2.0 GeV/c^2, JETSET/PYTHIA package [102] is adopted.

For the NC deep inelastic scattering, the ratio of NC to CC is assumed to be

$$\frac{\sigma(\mathrm{NC})}{\sigma(\mathrm{CC})} = \begin{cases} 0.26 & (E_\nu < 3\ \mathrm{GeV}) \\ 0.26 + 0.04(E_\nu/3 - 1) & (3 < E_\nu < 6\ \mathrm{GeV}) \\ 0.30 & (E_\nu > 6\ \mathrm{GeV}) \end{cases}, \tag{A.20}$$

which is based on the experimental results of Ref. [103].

A.1.4 Coherent pion production

The coherent pion production is the neutrino interaction with a whole nucleus instead of an individual nucleon. In such interaction, the charge or isospin of the nucleus does not change. This reaction produces one pion with the same charge as the intermediating weak boson. Since the transferred momentum to the nucleus is small, the angular distribution of the recoil leptons and pions are peaked in the forward direction, and the nucleus does not break up due to the small momentum transfer.

The cross-section and the kinematics of coherent pion production is calculated based on the model of Rein and Sehgal [74]. The differential cross-section of the Rein & Sehgal model is expressed by

$$\frac{d^3\sigma}{dQ^2 dy dt} = \frac{G_F^2 m_N E_\nu}{2\pi^2} f_\pi^2 A^2 (1-y) \cdot \left.\frac{d\sigma(\pi N \to \pi N)}{dq^2}\right|_{q^2=0} \cdot \left(\frac{1}{1 + Q^2/M_A^2}\right)^2 e^{-bt} F_{\mathrm{abs}}, \tag{A.21}$$

where f_π is the pion decay constant of $0.93 m_\pi$, A is the atomic number, $b = (R_0 A^{1/3})^2/3$ is of the order of the transverse dimension of the nucleus taken to be 80 GeV^{-2} for oxygen, and t is the square of the four-momentum transfer to the nucleus. F_{abs} is a factor coming from the pion absorption in the nucleus. However, Marteau *et al.*have recently pointed out that the nuclear medium can modify widths of resonances, thus we make modifications on the cross-section calculation based on their proposal [75]. Figure A.3 shows the comparison of the cross-sections between the Rein & Sehgal model and its modification by Marteau *et al.*The model of Rein and Sehgal gives the sightly higher value of cross-section around the neutrino energy of 1 GeV.

In our simulation, we set the cross-section for CC coherent pion production to zero based on the measurement with SciBar [76, 61]. For NC coherent pion production, we adopt the model of Rein and Sehgal with the corrections reported

by Marteau. We have measurements of NC coherent pion production cross-section in the energy region of a few GeV, but there is a possibility that the cross-section is also considerably smaller than the MC prediction in the K2K beam energy assuming the isospin relation $\sigma(\mathrm{CC}) = 2\sigma(\mathrm{NC})$. Thus, we evaluate the uncertainty of cross-section considering the differences between alternative NC coherent pion production models.

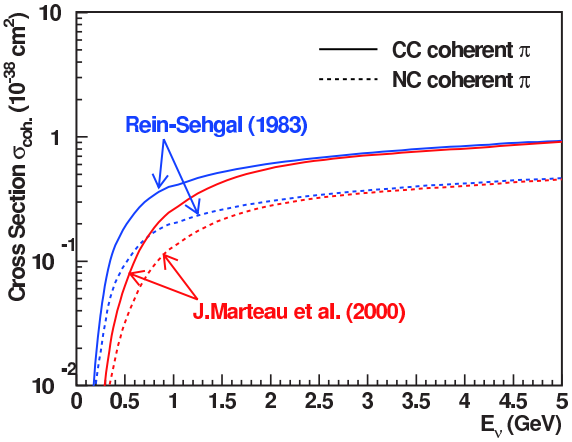

Figure A.3: Cross section of the coherent pion production off the ^{16}O nucleus. Solid lines show the cross-section of CC coherent pion production, and dashed lines show that of NC. Blue and red lines show the model of Rein & Sehgal [74] and Marteau *et al*. [75], respectively.

Appendix B

Verification of the ν_e flux prediction with SciBar

In order to validate the ν_e flux prediction by the beam MC simulation, we have performed the measurements of ν_e composition in the neutrino beam with two near detectors, LG [104] and SciBar. Here, we describe the details of the SciBar detector and present the result of the ν_e flux measurement with SciBar.

B.1 The SciBar detector

A fully active scintillator detector, SciBar, was constructed as an upgrade of the near detector complex, replacing the LG detector in summer 2003. A schematic views of the detector and the readout system are shown in Figure B.1. The detector is designed to measure the neutrino energy spectrum and study of neutrino interaction with good detection efficiency for low momentum particles.

The main part of the SciBar detector consists of an array of plastic scintillator strips to realize fully active detector and fine segmentation. The SciBar detector consists of 14848 scintillator strips arranged into 64 layers. Each layer consists of two planes, with 116 strips to give horizontal and vertical position. The scintillator strips are produced with TiO_2 reflector coating and a hole of 1.8 mm in diameter at the point of production (called extruded scintillator [105]). Each strip have dimensions of $1.3 \times 2.5 \times 300$ cm^3. In total, the detector weights about 15 tons and the dimensions are $3 \times 3 \times 1.7$ m^3. The scintillation light is guided by wavelength shifting (WLS) fibers, inserted into the holes of scintillator strips, to 64-channel

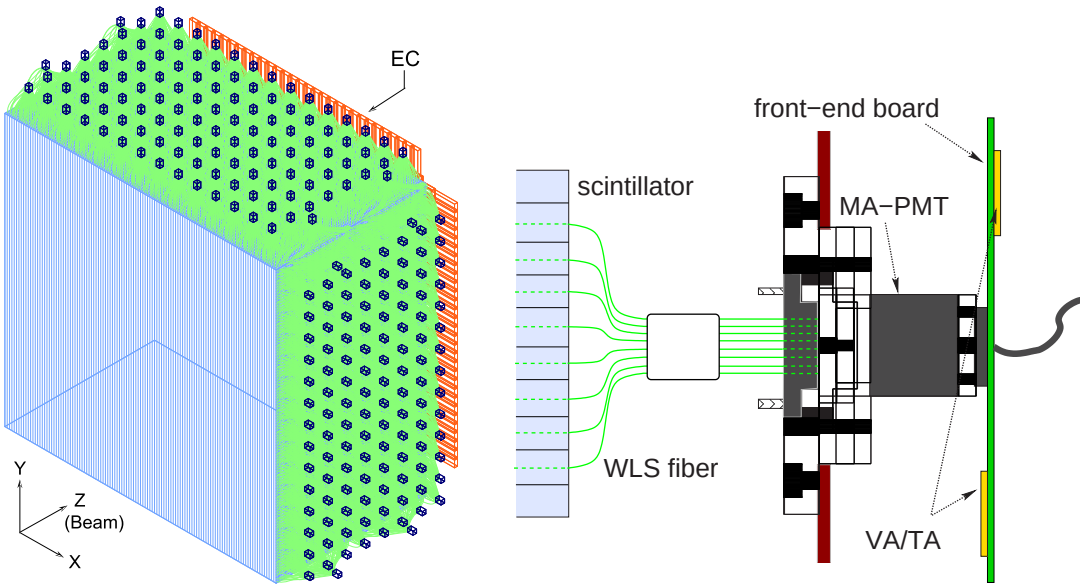

Figure B.1: Schematic views of the SciBar detector (left) and the readout system (left).

multi-anode photomultipliers (MAPMTs). A bundle of 64 WLS fibers is glued to an attachment for precise alignment between fibers and the photo-cathode of the MAPMT.

The readout system for MAPMT consists of two components: a front-end electronics board attached to the MAPMT and a back-end VME module [106, 107, 108]. At the front end, a circuit board with self-triggering readout using VA/TA ASIC (VA32HDR11 [109] and TA32CG [110]) was newly developed. VA has 32-channel pre-amplifier followed by a slow-shaper and a multiplexer, and serialize the outputs from the MAPMT. TA has a fast-shaper with a comparator, which provides the timing information of OR-ed signal of 32 channels. The output from the MAPMT is serialized by front-end electronics and digitized by FADCs on the back-end VME modules. Charge and timing information are digitized by FADCs on the back-end VME modules and the multi-hit TDCs, respectively. The noise level and the timing resolution for MIP signal are about 0.3 photoelectrons (p.e.) and 1.3 nsec, respectively. The back-end module also newly developed as a standard VME-9U module, and controls readout of the front-end boards.

These features of the detector allows us to reconstruct all the charged particles produced in neutrino interaction. A typical event display of CC-QE interaction is shown in Figure B.2.

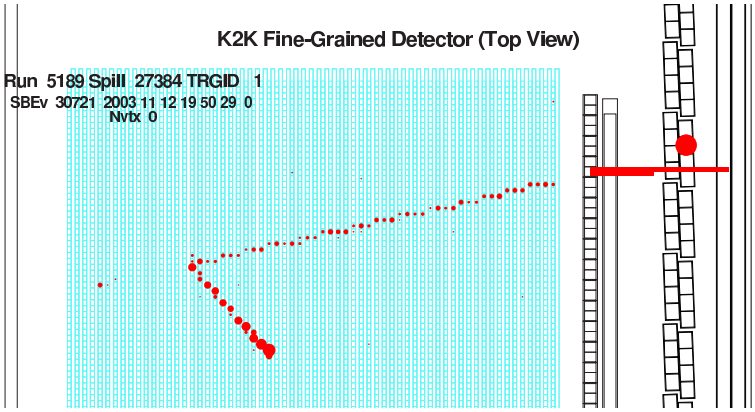

Figure B.2: A typical event display of CC-QE interaction in the SciBar detector. The longer track is muon and the shorter is proton. The area of hit circle is proportional to energy deposit in a scintillator strip.

In the downstream part of the SciBar, an electromagnetic calorimeter (EC) is installed to study the ν_e contamination in the beam and π^0 production in neutrino interaction. The calorimeter modules are originally built for CHORUS neutrino experiment at CERN [111]. A module of EC consists of scintillating fibers and lead sheets. The dimensions of the module are $4.0 \times 8.2 \times 262$ cm^3. A vertical plane (32 modules) and a horizontal plane (30 modules) are installed between the scintillator tracker and the MRD detector, providing an additional eleven radiation lengths ($11X_0$) to the main tracker part (about $4X_0$). The energy resolution of the EC is about $14/\sqrt{E(\mathrm{GeV})}$% with linearity better than 10%.

To reconstruct charged particles in SciBar, track projections in each of two dimensional view are looked for using a cellular automaton algorithm [112, 113]. Then, track candidates from two views are combined based on matching of the track edges in the beam direction and timing information. Reconstructed tracks are required to have hits in more than three consecutive layers. The minimum length of reconstructible track is 8 cm, corresponding to 450 MeV/c for protons. The reconstruction efficiency for an isolated track longer than 10 cm is 99%. The track finding efficiency as a function of the number of traversed layers for muons, protons and charged pions according to the MC simulation are shown in Figure B.3. In the measurement of ν_μ energy spectrum, we select muons in CC interactions. The muon is identified by requiring corresponding track or hits in MRD, which imposes a threshold of 450 MeV/c on muon momentum. The p_μ scale uncertainty, p_μ resolution, and θ_μ resolution are 2.7%, 80 MeV/c, and 1.6 degrees,

respectively.

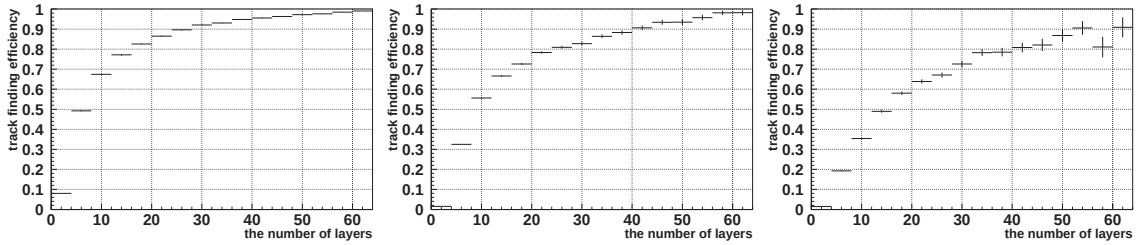

Figure B.3: Track finding efficiency of the SciBar detector as a function of the number of traversed layers for muons (left), protons (center) and charged pions (right).

B.2 ν_e flux measurement by SciBar

The measurement of the ν_e contamination in the beam has been performed by SciBar with a statistics corresponding to 2.1×10^{19} POT.

In order to measure the ν_e flux, we select the ν_e events interacting with SciBar in CC interactions and separate recoil electrons from muons with EC. Since the EC detector has a radiation length of $11X_0$, electrons in the energy range of $\sim$ 1 GeV are almost fully contained. On the other hand, the averaged energy loss in EC for penetrating muons and charged pions is small, which is estimated to be $\sim$ 100 MeV. Thus, we look for the event with a large signal of electromagnetic shower in a restricted region of EC. A typical event display of ν_e interaction is shown in Figure B.4.

In EC, the hits are clustered within a 20 cm width centered in the module with the maximum signal. We estimate the energy deposit in EC from the total energy of the cluster (cluster energy). Using the cluster energy for each plane, the electron event candidates are selected with the following criteria:

(i) The maximum hit energy of the first plane is greater than 100 MeV,

(ii) The cluster energy of the first plane (E_1) is greater than 350 MeV,

(iii) The ratio E_2/E_1 lies in the range 0.2–1.1, where E_2 is the cluster energy of the second plane,

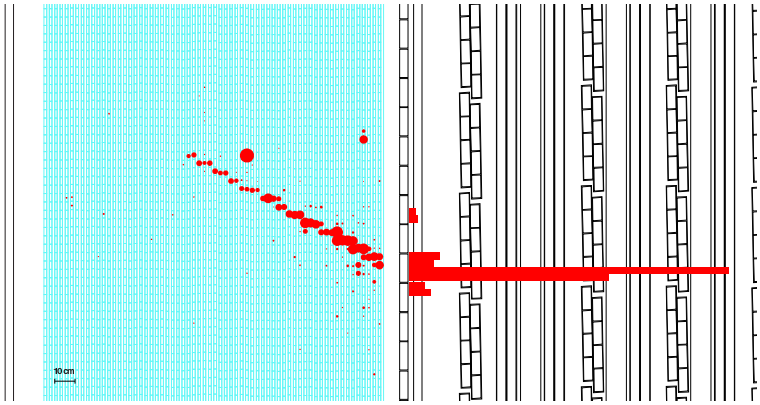

Figure B.4: Event display of ν_e interaction in SciBar.

(iv) The event with any track starting in the fiducial volume of SciBar (9.38 ton) is matched with the position of the EC clusters.

(v) The energy outside of the cluster for each EC plane is less than 30 MeV.

With criteria (i) (ii), the events with single MIP track or multi tracks are rejected. The criterion (iii) selects the electron events efficiently: the fraction of electron is estimated to be 95% according to the MC simulation. Rejecting the remaining ν_μ multi-hadron production events with the criterion (v), we enhance ν_e CC events.

After the selection cuts, we observed 42 electron candidate events. The visual examination of the events allows us to discard 9 events; they are identified as background events of the beam-induced particles generated by neutrino interactions outside SciBar, or as π^0 production events. In this sample, we expect there is a fraction of background originated from the π^0 production in the ν_μ interactions. For the π^0 production background, we estimate the contamination with the visual examination described above, by correcting the detection efficiency based on the MC simulation. Finally, we obtain 33 evens with the background expectation of 3 ± 2 events. The purity of electron is 90 %. The characteristics of the selected events are compared to those of MC events resulting from a full simulation of ν_e interactions in the SciBar and including also a 10% background from ν_μ interactions.

Figure B.5 shows the electron energy spectrum for the surviving events with the MC expectation. In the MC events, the 10% fraction of background events is taken into account. The electron energy is reconstructed by correcting the energy loss in SciBar and the longitudinal leakage; the average correction is of the

order of 20%. The data and the MC events are in good agreement except for the higher energy region. The discrepancy in the higher energy region indicates our underestimate of kaon production in $p - Al$ collisions at the target, however, we cannot give any conclusion with a small statistics.

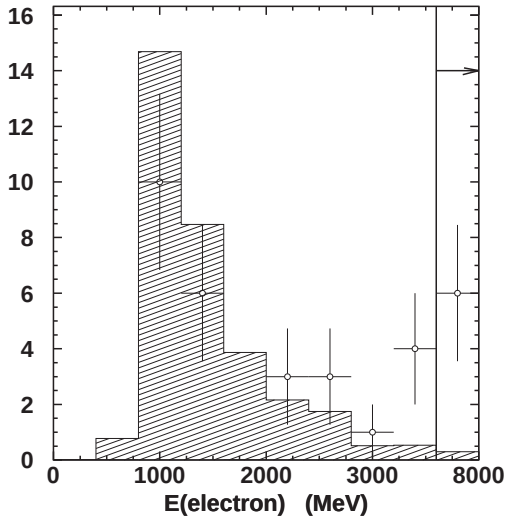

Figure B.5: Electron energy spectrum for the ν_e candidate events. The open circles and the histogram show the data and the MC events, respectively. The MC events are normalized to the data separately for the signal and background events.

In the $\nu_\mu \rightarrow \nu_e$ search, the contribution of beam-ν_e background is estimated based on the MC simulation including its flux and cross-section. Thus, to validate the MC prediction, we estimate the interaction ratio of ν_e to ν_μ. The total number of ν_μ interactions is calculated by correcting the number of observed events with the detection efficiency estimated by the MC simulation. The total ν_μ interactions are estimated from the ν_μ CC event sample used in the measurement of ν_μ energy spectrum in SciBar. The resultant ν_e/ν_μ interaction ratio is $1.6 \pm 0.3(\text{stat.}) \pm 0.2(\text{syst.})\%$.

B.2.1 Comparison with the beam MC prediction and the LG measurement

The measurement of beam-ν_e contamination has been also performed with the LG detector. The event selection and the result are given in Reference [104, 63].

The resulting ν_e/ν_μ interaction ratios by SciBar and LG, and the MC prediction are:

$$\begin{aligned} \text{SciBar:} &\quad 1.6 \pm 0.3(stat.) \pm 0.2(syst.)\% \\ \text{LG:} &\quad 1.6 \pm 0.4(stat.)^{+0.8}_{-0.6}(syst.)\% \\ \text{Beam MC:} &\quad 1.3\% \ \text{(at near site)} \end{aligned}$$

These are in a good agreement each other and give a validity of the ν_e flux prediction in the beam MC simulation.

Appendix C

Comment on the far/near flux ratio

In the K2K experiment, the ν_μ beam is produced via decays of positive pions generated in $p - Al$ collisions. If we assume the neutrino source to be a point like, the intensity of neutrino beam is proportional to $1/L^2$, where L is the distance from the source to the detector location. The SK detector is located 250km far from the π production target and the neutrino source is regarded as a point like. However, the near detectors are close to the target (L = 300 m) and the neutrino flux is not proportional to $1/L^2$ due to the finite size of decay volume in which π^+'s decay to μ^+'s and ν_μ's. In addition, there is a difference of geometrical acceptance for neutrinos between the near detectors and SK. The detector acceptance is proportional to the solid angle to the target and the covering angles of 1KT and SK are ±20 mrad and ±0.1 mrad, respectively. Therefore, we predict the event rate at SK with the near detector measurements by multiplying the far/near flux ratio. The predicted neutrino fluxes at the near site and SK and the far/near flux ratio are shown in Figure C.1. Here, we give explanations of the following subjects:

- Shape of the far/near flux ratio,
- Possibility of employing near detectors which cover the same geometrical acceptance as SK.

C.1 Shape of the far/near flux ratio

At the near detectors, the geometrical acceptance for low energy neutrinos is different from that for high energy ones. The low energy pions, contributing

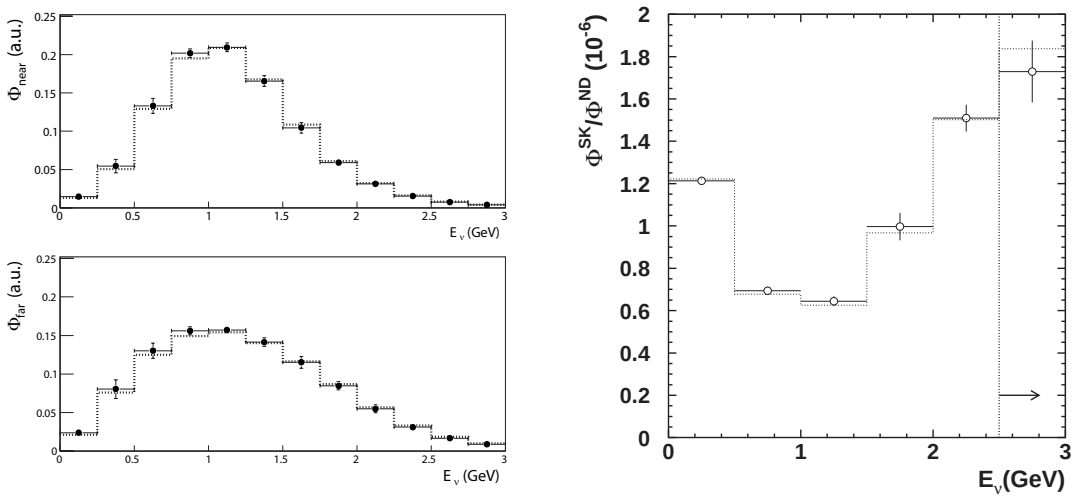

Figure C.1: Neutrino fluxes at the near site and SK (left) and the far/near flux ratio (right) predicted by the beam MC simulation.

to the low energy neutrino flux, decay near the target, while the high energy pions travel far away from the target before their decays. The decay piont of low energy pions is far from the near detectors compared with that of high energy ones. Therefore, the geometrical acceptance of the near detectors for low energy neutrinos become smaller than that for high energy ones, as shown in Figure C.2. For examples, the flight length of 0.5 GeV pions is 20 m and that of 2.5 GeV pions is 100 m. This difference of π flight length results in different 1KT acceptances for neutrinos by a factor of two, and the flux of low energy neutrinos becomes low. On the other hand, the difference of π decay point is negligible at SK and the geometrical acceptance does not depend on the neutrino energy. As a result, the far/near flux ratio goes down in the low energy region below 0.5 GeV.

In addition, the near detectors are sensitive to neutrinos which travel off the beam axis (off-axis neutrinos) due to the large detector coverage. Figure C.3 shows the illustration of off-axis neutrinos. The energy of neutrino (E_ν) from the π decay is expressed as

$$E_\nu = \frac{m_\pi^2 - m_\mu^2}{2(E_\pi - p_\pi \cos\theta)}, \tag{C.1}$$

where m_π, m_μ, E_π, p_π and θ are the pion mass, the muon mass, the pion energy, the pion momentum and the direction of neutrino with respect to the beam axis. Figure C.4 shows the neutrino energy as a function of the pion energy for various

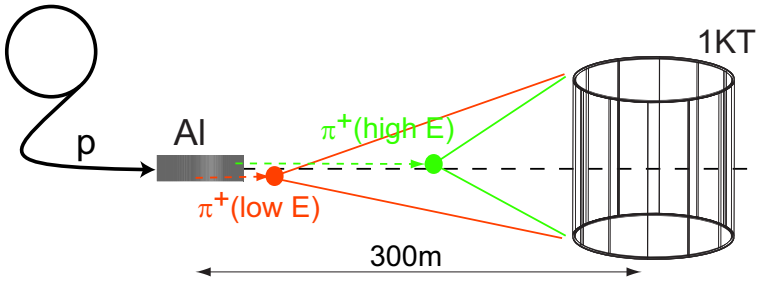

Figure C.2: Illustration of acceptance for low and high energy neutrinos at the near site.

off-axis angles. We recognize that the neutrino energy is not very correlated with the pion energy for off-axis neutrinos, and high energy pions contribute to the neutrino flux around 1 GeV. Therefore, the neutrino energy spectrum has a narrow peak around 1 GeV at the near detectors and that shows a broad distribution at SK, as shown in Figure C.1. Consequently, the far/near flux ratio goes up above ~ 1 GeV.

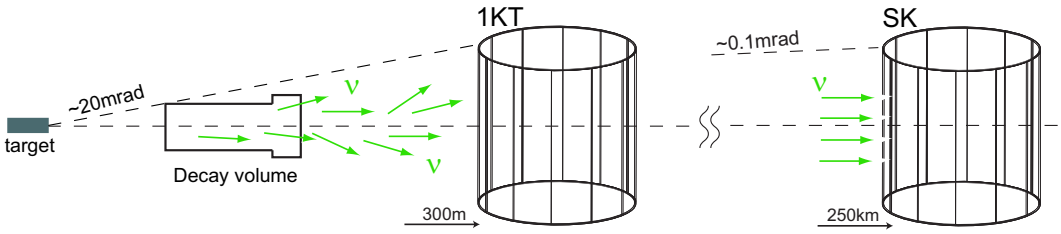

Figure C.3: Illustration of off-axis neutrinos.

C.2 Possibility of employing near detectors which cover the same geometrical acceptance as SK

We consider the case of employing near detectors which cover the very forward region of ~ 0.1 mrad (equivalent to the geometrical acceptance of the SK detector).

When we measure the neutrino flux in the very forward region, the contribution of off-axis neutrinos becomes small, but the near detectors are yet sensitive to them. Due to the spacial spread of pions, the near detectors have a finite geometrical acceptance for off-axis neutrinos produced by pions which have a transverse

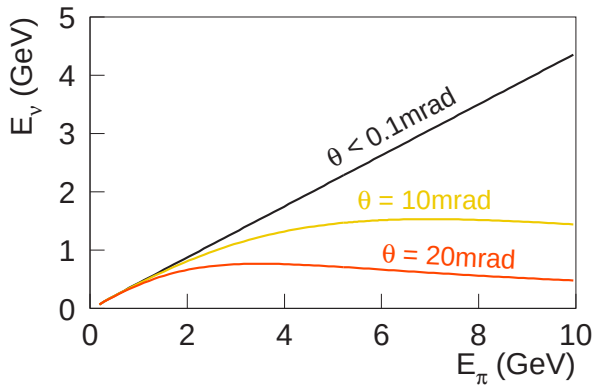

Figure C.4: The neutrino energy as a function of the parent pion energy for various off-axis angles.

momentum or travel far from the beam axis, as shown in Figure C.5. In addition, the difference of geometrical acceptance between low and high energy neutrinos still remains, as described above. These make a difference of neutrino energy spectrum between the near detectors and SK.

Thus, we can not adopt a simple $1/L^2$ extrapolation to predict the SK event rate even in that case. We should take into account the energy dependent far/near flux ratio.

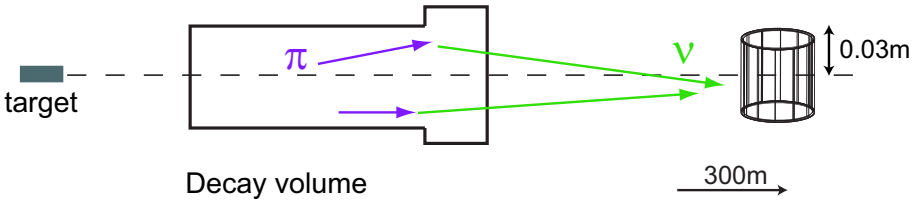

Figure C.5: Illustration of off-axis neutrinos contributing to the flux in the very forward region of the near detectors

Appendix D

Decay-electron identification

We identify the decay-electron event to reject the background originated from ν_μ-CC interactions.

In SK, the decay-electron events are classified into three categories based on the time difference Δt between the parent muon event and the following decay-electron:

- primary-event type:
  Hits associated with a decay-electron are detected within 1.2 μsec trigger gate with the primary event of the parent muon.
- sub-event type: A decay-electron is recorded as a separate event from the primary one.
- splitting-event type:
  A decay-electron is emitted at the timing around the boarder of the primary-event time window. Hits of a decay-electron are observed partially in the primary event and partially in the separate event.

We describe the criteria to select these event categories of decay-electrons.

For the events with the primary-event and splitting-event decays, we observe another peak in the timing distribution after the primary PMT hits. We identify the separate events when Δt is larger than 0.1μsec. We require that the number of PMT hits associated with a decay-electron should be greater than 40 (20) in 30 nsec time window for SK-I (SK-II).

For the sub-event type decays, the decay-electron ring candidates are selected by requiring that the goodness of the vertex fitting is more than 0.5 and the total

number of photo-electrons is less than 2000. Then, we require that the event follows the primary event with PMT hits above 60 (30) in 50 nsec time window for SK-I (SK-II), which corresponds to $\sim$ 11 MeV decay-electron threshold.

Finally, since we cannot detect the events with $\Delta t \sim 1\mu$sec efficiently due to the dead time of the readout electronics, we reject events with $0.8\mu\text{sec} < \Delta t < 1.2\mu\text{sec}$.

Appendix E

Comment on the surviving events before the π^0 rejection

We observe five surviving events in the entire data sample before the π^0 rejection, as shown in Figure E.1. Assuming that we observe only ν_μ-originated background events, we recognize that all of the observed events lie outside of the most probable region of the E_e range from 150 MeV to 350 MeV and the M_{inv} range from 100 MeV/c^2 to 140 MeV/c^2. However, the probability of observing one event in this region is approximately 40%, and the probability of observing no event among five trials is estimated to be 7.8% ($(1 - 0.4)^5 = 0.0778$). E_e and M_{inv} also shows probable values, as shown in Figure E.2.

In addition, we perform statistical tests to make a statement about how well the observed distribution agree with the MC prediction. We construct a likelihood of observing five given events. The likelihood ($\mathcal{L}$) is calculated by the product of probabilities as

$$\mathcal{L} = \prod_{i=1}^{5} P(E_e^i, M_{inv}^i), \tag{E.1}$$

where $P(E_e^i, M_{inv}^i)$ is the probability of observing an event with E_e^i and M_{inv}^i for i-th event. The probability is estimated by the MC ν_μ-originated background events. Figure E.3 shows the likelihood distribution obtained from many virtual experiments of observing five events. We estimate the probability of obtaining a result with the same level of discrepancy as the K2K data or higher to be 51.8%. Further, the two-dimensional Kolmogorov-Smirnov test shows a probability of 47.4%.

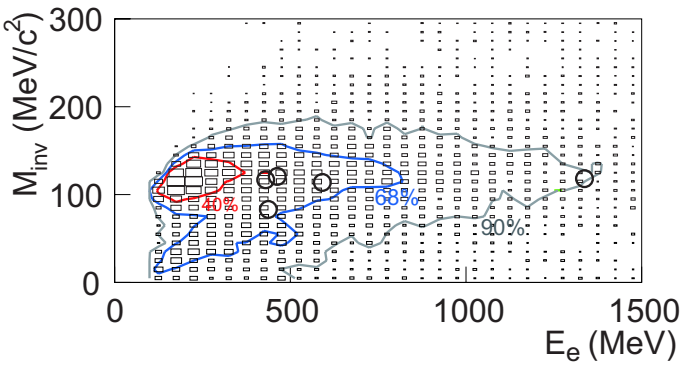

Figure E.1: Distribution of signal candidate events in the M_{inv}-E_e space for K2K-I and K2K-II. Five surviving events before the π^0 rejection in data are shown by open circles. The MC events originated from ν_μ are shown by open boxes. The acceptance region with a 40% (68% or 90%) probability is shown with a contour line.

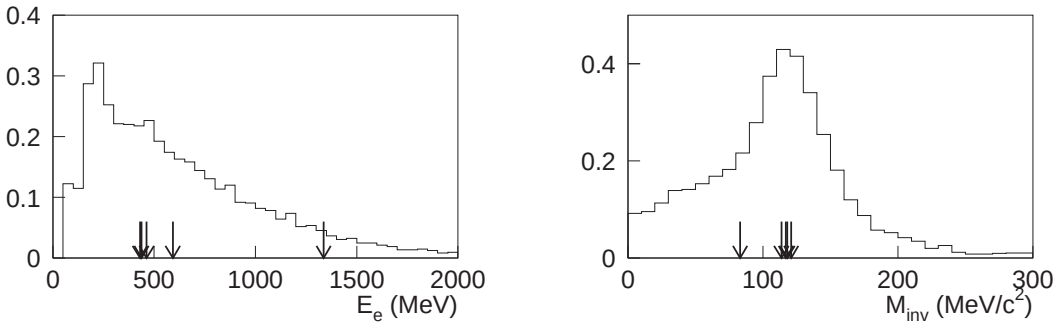

Figure E.2: Distributions of E_e (left) and M_{inv} (right) for the surviving events. The arrows show the observed events in the data. The histograms show the MC events originated from ν_μ.

Consequently, we conclude that the observed data stand within the statistical fluctuation of background events.

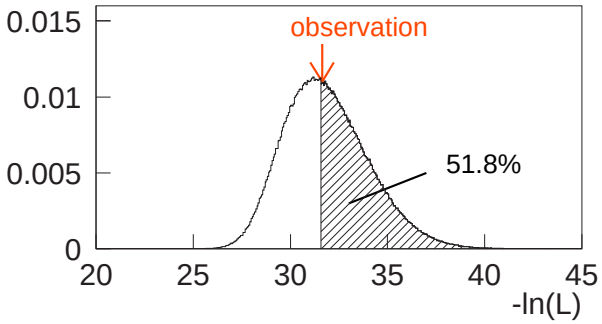

Figure E.3: Likelihood distribution from many virtual experiments with five observations per experiment. The arrow shows the observed data in K2K. The probability of obtaining a result with the same level of discrepancy as the observed data or higher is 51.8%.

References

[1] C. Weinheimer *et al.*, Phys. Lett. **B460**, 219 (1999).

[2] V. M. Lobashev *et al.*, Phys. Lett. **B460**, 227 (1999).

[3] K. Assamagan *et al.*, Phys. Rev. **D53**, 6065 (1996).

[4] R. Barate *et al.* (ALEPH), Eur. Phys. J. **C2**, 395 (1998).

[5] T. Yanagida, Proc. of Workshop Unified theory and Baryon Number in the Univers, KEK, Tsukuba, Japan (1978).

[6] P. Gell-Mann, M. Ramond and R. Slansky, Supergravity, edited by P. van Nieuwenhuizen and D. Freedman (North-Holland, Amsterdam, 1979), p. 315.

[7] B. T. Cleveland *et al.*, Astrophys. J. **496**, 505 (1998).

[8] Y. Fukuda *et al.* (Kamiokande), Phys. Rev. Lett. **77**, 1683 (1996).

[9] J. N. Abdurashitov *et al.* (SAGE), Phys. Rev. **C60**, 055801 (1999), astro-ph/9907113.

[10] W. Hampel *et al.* (GALLEX), Phys. Lett. **B447**, 127 (1999).

[11] E. Bellotti, Nucl. Phys. Proc. Suppl. **91**, 44 (2001).

[12] S. Fukuda *et al.* (Super-Kamiokande), Phys. Lett. **B539**, 179 (2002), hep-ex/0205075.

[13] Q. R. Ahmad *et al.* (SNO), Phys. Rev. Lett. **89**, 011301 (2002), nucl-ex/0204008.

[14] G. L. Fogli, E. Lisi, A. Marrone, and A. Palazzo, Phys. Lett. **B583**, 149 (2004), hep-ph/0309100.

[15] T. Araki *et al.* (KamLAND), Phys. Rev. Lett. **94**, 081801 (2005), hep-ex/0406035.

[16] Y. Ashie *et al.* (Super-Kamiokande), Phys. Rev. **D71**, 112005 (2005), hep-ex/0501064.

[17] Y. Ashie *et al.* (Super-Kamiokande), Phys. Rev. Lett. **93**, 101801 (2004), hep-ex/0404034.

[18] E. Aliu *et al.* (K2K), Phys. Rev. Lett. **94**, 081802 (2005), hep-ex/0411038.

[19] N. Tagg (the MINOS) (2006), hep-ex/0605058.

[20] M. Apollonio *et al.*, Eur. Phys. J. **C27**, 331 (2003), hep-ex/0301017.

[21] A. Piepke (Palo Verde), Prog. Part. Nucl. Phys. **48**, 113 (2002).

[22] B. Armbruster *et al.* (KARMEN), Phys. Rev. **D65**, 112001 (2002), hep-ex/0203021.

[23] E. Church *et al.* (MiniBooNE), FELMILAB-P-0898 (1997).

[24] High Energy Accelerator Research Organization (KEK) in Tsukuba, Ibaraki, Japan. (http://www.kek.jp).

[25] H. Sato, *Commissioning run of the long-baseline neutrino oscillation experiment at the 12-GeV KEK-PS*, Contributed to IEEE Particle Accelerator Conference (PAC 99), New York, 29 Mar - 2 Apr 1999.

[26] H. Tanaka, KEK-preprint 91-27 (1991).

[27] Y. Yamanoi, IEEE Trans. on Applied Superconductivity. **10**, 252 (2000).

[28] T. Maruyama, Ph.D. thesis, Tohoku University (2000).

[29] S. Nakayama, Master thesis, University of Tokyo (1999).

[30] A. Suzuki *et al.* (K2K), Nucl. Instrum. Meth. **A453**, 165 (2000), hep-ex/0004024.

[31] K. Nitta *et al.*, Nucl. Instrum. Meth. **A535**, 147 (2004), hep-ex/0406023.

[32] T. Ishii *et al.* (K2K MRD GROUP), Nucl. Instrum. Meth. **A482**, 244 (2002), hep-ex/0107041.

[33] T. Inagaki, Ph.D. thesis, Kyoto University (2001).

[34] Y. Cho *et al.*, Private communication with W. Gajewski, a K2K collaborator.

[35] J. Hill, K2K internal note BEAM/BMMC/00-001 (2000).

[36] J. Gabriel, T. A. Amburgey and B. L. Bishop (1977), ORNL/TM-5619.

[37] C. Zeitnitz and T. A. Gabriel, Nucl. Instrum. Meth. **A349**, 106 (1994).

[38] A. Fasso *et al.*, FLUKA: Present status and future developments (1993), given at 4th International Conference on Calorimetry and High-energy Physics, La Biodola, Italy, 19-25 Sep. 1993.

[39] J. R. Sanford and C. L. Wang, Brookhaven National Laboratory, AGS internal report (1967).

[40] R. A. Lundy *et al.*, Phys. Rev. Lett. **14**, 504 (1966).

[41] D. Dekkers *et al.*, Phys. ReV. **137**, B962 (1965).

[42] W. F. Baker *et al.*, Phys. ReV. Lett. **7**, 101 (1961).

[43] A. Yamamoto, KEK Report **81-13** (1981).

[44] Y. Cho *et al.*, Phys. Rev. **D4**, 1967 (1971).

[45] Y. Hayato, Nucl. Phys. Proc. Suppl. **112**, 171 (2002).

[46] L. L. Salcedo, E. Oset, M. J. Vicente-Vacas, and C. Garcia-Recio, Nucl. Phys. **A484**, 557 (1988).

[47] C. H. Q. Ingram *et al.*, Phys. Rev. **C27**, 1578 (1983).

[48] H. W. Bertini, Phys. Rev. **C6**, 631 (1972).

[49] K. V. Alanakian *et al.*, Phys. Atom. Nucl. **61**, 207 (1998).

[50] S. J. Lindenbaum *et al.*, Phys. Rev. **105**, 1874 (1957).

[51] T. S. Kosmas and E. Oset, Phys. Rev. **C53**, 1409 (1996).

[52] *GEANT – Detector Description and Simulation Tool, Application Software Group, Computing and Networks Division, CERN (1993), CERN Program Library Long Writeup W5013.* (1993).

[53] E. Bracci *et al.* (1972), CERN/HERA 72-1.

[54] A. S. Carrol *et al.*, Phys. Rev. **C14**, 635 (1976).

[55] Y. Fukuda *et al.*, Nucl. Instrum. Meth. **A501**, 418 (2003).

[56] I. Kato, Ph.D. thesis, Kyoto University (2004).

[57] A. Shima, Master's thesis, Kyoto University (2001).

[58] T. Iwashita, Ph.D. thesis, Kobe University (2003).

[59] H. Yokoyama, Ph.D. thesis, Tokyo University of Science (2004).

[60] H. Maesaka, Ph.D. thesis, Kyoto University (2005).

[61] M. Hasegawa, Ph.D. thesis, Kyoto University (2006).

[62] M. H. Ahn *et al.* (K2K), Phys. Rev. Lett. **90**, 041801 (2003), hep-ex/0212007.

[63] M. H. Ahn *et al.* (K2K), Phys. Rev. Lett. **93**, 051801 (2004), hep-ex/0402017.

[64] M. G. Catanesi *et al.*, *Proposal to study hadron production for the neutrino factory and for the atmospheric neutrino flux*, CERN-SPSC-99-35.

[65] *The HARP detector at the CERN PS* (in preparation).

[66] M. G. Catanesi *et al.* (HARP), Nucl. Phys. **B732**, 1 (2006), hep-ex/0510039.

[67] H. Fesefeldt, *THE SIMULATION OF HADRONIC SHOWERS: PHYSICS AND APPLICATIONS*, PITHA-85-02.

[68] M. Kohama, Ph.D. thesis, Kobe University (2000).

[69] M. Ishitsuka, Ph.D. thesis, University of Tokyo (2004).

[70] T. Barszczak, Master's thesis, Univirsity of California, Irvine (2005).

[71] J. A. Nelder and R. Mead, Computer Journal **7**, 308 (1965).

[72] S. Nakayama *et al.* (K2K), Phys. Lett. **B619**, 255 (2005), hep-ex/0408134.

[73] E. H. Monsay, Phys. Rev. Lett. **41**, 728 (1978).

[74] D. Rein and L. M. Sehgal, Nucl. Phys. **B223**, 29 (1983).

[75] J. Marteau, Eur. Phys. J. **A5**, 183 (1999), hep-ph/9902210.

[76] M. Hasegawa *et al.* (K2K), Phys. Rev. Lett. **95**, 252301 (2005), hep-ex/0506008.

[77] H. Ejiri, Phys. Rev. **C48**, 1442 (1993).

[78] M. Shiozawa, Ph.D. thesis, University of Tokyo (1999).

[79] G. J. Feldman and R. D. Cousins, Phys. Rev. **D57**, 3873 (1998), physics/9711021.

[80] Y. Fukuda *et al.* (Kamiokande), Phys. Lett. **B335**, 237 (1994).

[81] (2006), hep-ex/0604011.

[82] Y. Itow *et al.* (2001), hep-ex/0106019.

[83] C. H. Llewellyn Smith, Phys. Rept. **3**, 261 (1972).

[84] V. Bernard, L. Elouadrhiri, and U. G. Meissner, J. Phys. **G28**, R1 (2002), hep-ph/0107088.

[85] S. J. Barish *et al.*, Phys. Rev. **D16**, 3103 (1977).

[86] N. J. Baker *et al.*, Phys. Rev. **D23**, 2499 (1981).

[87] S. Bonetti *et al.*, Nuovo Cim. **A38**, 260 (1977).

[88] S. V. Belikov *et al.*, Z. Phys. **A320**, 625 (1985).

[89] L. A. Ahrens *et al.*, Phys. Rev. Lett. **56**, 1107 (1986).

[90] F. A. Brieva and A. Dellafiore, Nucl. Phys. **A292**, 445 (1977).

[91] D. Rein and L. M. Sehgal, Ann. Phys. **133**, 79 (1981).

[92] R. P. Feynman, M. Kislinger, and F. Ravndal, Phys. Rev. **D3**, 2706 (1971).

[93] G. M. Radecky *et al.*, Phys. Rev. **D25**, 1161 (1982).

[94] T. Kitagaki *et al.*, Phys. Rev. **D34**, 2554 (1986).

[95] M. Pohl *et al.*, Lett. Nuovo Cim. **24**, 540 (1979).

[96] M. Gluck, E. Reya, and A. Vogt, Z. Phys. **C67**, 433 (1995).

[97] A. Bodek and U. K. Yang, Nucl. Phys. Proc. Suppl. **112**, 70 (2002), hep-ex/0203009.

[98] C. H. Albright and C. Jarlskog, Nucl. Phys. **B84**, 467 (1975).

[99] M. Derrick *et al.*, Phys. Rev. **D17**, 1 (1978).

[100] H. Sarikko, Proc. of NEUTRINO'79 p. 507 (1979).

[101] S. Barlag *et al.* (Amsterdam-Bologna-Padua-Pisa-Saclay-Turin), Zeit. Phys. **C11**, 283 (1982).

[102] T. Sjostrand, PYTHIA 5.7 and JETSET 7.4: Physics and manual (1995), hep-ph/9508391.

[103] P. Musset and J. P. Vialle, Phys. Rept. **39**, 1 (1978).

[104] M. Yoshida, Ph.D. thesis, Osaka University (2001).

[105] The MINOS Collaboration, Technical Design Report (1998).

[106] M. Yoshida *et al.*, IEEE Trans. Nucl. Sci. **51**, 3043 (2004).

[107] S. Yamamoto *et al.*, IEEE Trans. Nucl. Sci. **52**, 2992 (2005).

[108] S. Yamamoto, Master thesis, Kyoto University (2003).

[109] VA32_HDR11 Specifications, http://www.ideas.no/products/ASICs/pdf/VA32_hdr11.pdf.

[110] TA32CG Specifications, http://www.ideas.no/products/ASICs/pdf/TA32cg.pdf.

[111] S. Buontempo *et al.*, Nucl. Instrum. Meth. **A349**, 70 (1994).

[112] I. Kisel and G. Ososkov, *An application of cellular automata and neural networks for event reconstruction in discrete detectors*, Prepared for 10th International Conference on Computing in High-energy Physics (CHEP 92), Annecy, France, 21-25 Sept 1992.

[113] A. Glazov, I. Kisel, E. Konotopskaya, and G. Ososkov, Nucl. Instrum. Meth. **A329**, 262 (1993).

List of Figures

List of Tables